

ABSTRACT

BRYAN, EUGENE NOBORU. The Influence of a TiN Buffer Layer on the PECVD Growth and Field Emission Properties of Carbon Nanotubes. (Under the direction of Robert J. Nemanich.)

This study explores the growth and field emission properties of carbon nanotubes (CNTs) prepared using Fe catalyst layers on TiN coated Si substrates. TiN buffer layers were employed as a catalyst support in the plasma enhanced chemical vapor deposition (PECVD) growth of the CNT films. The TiN layers were characterized by X-ray photoelectron spectroscopy, atomic force microscopy, and photo electron emission spectroscopy to establish the interaction of the Fe catalyst film with the TiN buffer layer and underlying substrate. The TiN layers were shown to directly influence the growth process by enabling the catalyst to remain in an active state.

The PECVD grown CNT films exhibited field emission current densities of 1 mA/cm^2 at applied fields of $\sim 2.1 \text{ V}/\mu\text{m}$. The emission distribution from the films, observed using a phosphor coated screen, was found to be uniform over selectively deposited areas up to 3.24 cm^2 . Non-linearity in the Fowler-Nordheim emission plots of the CNT films was shown to originate from adsorbate effects which have in many cases led to misleading analysis of field emission data. The uniform distribution of emission sites and the excellent field emission properties of the CNT films indicate that TiN, unlike SiO_2 , effectively functions as a catalyst barrier for growth without significantly impeding electron transport from the substrate to the emitter structures.

**THE INFLUENCE OF A TIN BUFFER LAYER ON THE PECVD GROWTH AND
FIELD EMISSION PROPERTIES OF CARBON NANOTUBES**

by
EUGENE NOBORU BRYAN

A thesis submitted to the Graduate Faculty of
North Carolina State University
in partial fulfillment of the
requirements for the Degree of
Master of Science

MATERIALS SCIENCE AND ENGINEERING

Raleigh, North Carolina

2007

APPROVED BY:

R. J. Nemanich
Chair of Advisory Committee

G. J-M. Duscher
Co-Chair

G. L. Bilbro
Minor Representative

DEDICATION

To my family.

BIOGRAPHY

Eugene Noboru Bryan was born in Naha, (Okinawa) Japan on June 18, 1977 to Benjamin Earl Bryan and Kiyo Nagata. He was the second child, seven years separated, from his sister Kathaleen Michiyo Bryan.

The early years of Eugene's recalled childhood were spent in Raleigh, NC where his father was employed as a Marine recruiter in close proximity to North Carolina State University. Eventually the military led his family to Cherry Point, NC where he received his elementary education. With his father's retirement in 1987, Eugene would spend his remaining adolescent years in Hubert, NC where he attended Swansboro Middle and High School.

In his early education, Eugene found himself excelling in mathematics and attributed his success to his mother's teachings of times tables in Japanese. His interest in science was inspired by the time that he spent with his father learning about fishing and hunting and how many of the tools that go along with the sports functioned. Countless hours were spent in his father's workshop listening to country music and tinkering with hand saws, drills, files or anything that could be used to make something new. He took advantage of the abundant amount of free time Hubert had to offer and started developing some of the skills that would eventually inspire him to become an engineer.

After graduation from high school, Eugene enrolled as a chemistry major at Chowan College in Murfreesboro, NC. He then chose to transfer to a larger college, and the following year he transferred to NCSU in which his undergraduate studies consisted of a transition from chemistry to physics at the end of his sophomore year. In December of 1999

he graduated with a B.S. in physics and a B.A. in chemistry. Near the end of completing his undergraduate work he started working in the laboratory of Dr. Robert Nemanich studying the diffusion activity of buried metal layers. The work in Dr. Nemanich's lab eventually led to his introduction to John Driscoll, the owner of Power Technology Services (PTS). He spent the next five years working on various projects as an employee of PTS, a small company located in the Research Triangle area. During his time at PTS Co. he continued to work closely with Dr. Nemanich and the students in his lab.

Eugene enrolled into the Materials Science and Engineering graduate program at NCSU in the fall of 2004. During this time he attended classes while continuing his work at PTS. In December of 2005 he returned to graduate school full time and is currently preparing a masters thesis based on the carbon nanotube and field emission research he has performed.

ACKNOWLEDGEMENTS

First I would like to thank my family, immediate and removed, and give special thanks to Don Fauver who has brought so much happiness to my mother. I could not have made it to the point I am at today without the support of my family and friends.

I am grateful to my committee members, Dr. Gerd Duscher who I have had the pleasure of speaking to about my research and learning TEM from, and Dr. Bilbro who I have had the pleasure working with during my days at PTS and in graduate school. I would also like to acknowledge Dr. John Hren for his insightful discussions about my research and also Dr. Jack Rowe for his recent involvement in my work.

I would like to thank Dr. Robert Nemanich for making my success in graduate school possible and enabling me to work with such a large group of unique and wonderful people. To all the members of the Surface Science Lab who I have had the opportunity to interact with over the past 8 years (*special thanks).

Past members:

Thomas Blair, Billyde Brown, James Burnette, Ted Cook, Brian Coppa, Charlie Fulton*, Philip Hartleib*, Ed Hurt, Jennifer Huening, Jaeseob Lee, Will Mecouch, Brian Rodriguez*, Brendan Shields, Kieran Tracey, John Waldrep, Yunyu Wang*, Branden Ward*, and Woochul Yang

Present members:

Matt Brukman, Jiyoung Choung*, Jacob Garguilo*, Jacquie Hanson*, Franz Keock*, Wendy Kong*, Xin Li, Jeff Mullen, James Perkins*, Joshua Smith, Anderson Sunda-Meya, Yingjie Tang*, Joseph Tedesco, Leigh Winfrey, and Matthew Zeman*.

I should also include a few others that went out of their way to help me with my research (Kevin Ball, Trinity Biggerstaff, Brad Hartman and Chuck Mooney).

John and Winna Driscoll, it was a pleasure working with you at PTS Co. I was lucky to be able to fall into such a unique company that allowed me to work so closely with the university. The initial funding for this research was obtained through a PTS/NCSU collaboration. I would like to acknowledge the Department of Defense (DOD) Small Business Innovation Research (SBIR) program for its involvement in the Phase I Air Force Contract Titled “Cold Cathode for Traveling Wave Tubes.”

Thank you to those at the Jožef Stefan Institute in Slovenia. Dr. Vincenc Nemanič and Marko Žumer I had a wonderful time in your beautiful country and enjoyed the collaboration we had together.

C.J. Hathorne, Edna Deas, and Cecilia Upchurch, you guys are great and I hope everyone appreciates you as much as I do.

TABLE OF CONTENTS

	Page
LIST OF TABLES	x
LIST OF FIGURES	xi
1. Introduction.....	1
1.1 Background on Carbon Nanotubes	1
1.1.1 Carbon.....	2
1.1.2 Graphite.....	3
1.1.3 Single-Walled Carbon Nanotubes.....	4
1.1.4 Multi-Walled Carbon Nanotubes.....	5
1.2 Carbon Nanotubes as Field Emitters for Vacuum Electronics	6
1.2.1 Vacuum Electronics Based on Thermionic Emitters.....	6
1.2.2 Vacuum Electronics Based on Field Emitters	7
1.2.3 Traditional Field Emitter Structures	8
1.2.4 Carbon Nanotubes as Field Emission Sources for Vacuum Electronics.....	8
1.3 Summary of CNT Properties and Applications Towards Vacuum Electronics.....	9
1.4 Overview of Thesis	10
REFERENCES	12
2. Synthesis of CNTs-General Principles and Methods.....	13
2.1 Overview of Synthesis Techniques.....	13
2.1.1 Arc-discharge.....	13
2.1.2 Laser Ablation.....	14
2.1.3 Chemical Vapor Deposition.....	14
2.2 Transition Metal Catalysts for CNT Growth	16
2.2.1 Catalyst Types and Deposition Techniques.....	16
2.2.2 Catalyst Activity	17
2.2.3 Catalyst Nanoparticle Formation	17
2.3 Growth Mechanisms of CNTs	18
2.3.1 Hydrocarbon Decomposition by Catalyst Nanoparticles.....	19
2.3.2 CNT Growth Modes	19
2.3.3 Surface Vs. Bulk Diffusion of Carbon and Effects on CNT Growth	20
2.4 Summary of CNT Synthesis	22
REFERENCES	22
3. TiN Buffer Layers Used as a Catalyst Support for CNT Growth.....	24
3.1 General Applications of TiN.....	24

3.2	Deposition of TiN by Plasma Assisted Reactive Evaporation.....	24
3.3	Characterization of PARE Deposited TiN Films.....	25
3.4	Characterization of Annealed Fe Films on TiN Coated Si Substrates.....	31
3.4.1	AFM of Annealed FE Films on TiN Coated Si Substrates.....	32
3.4.2	PEEM of Annealed Fe Films on TiN Coated Si Substrates.....	32
3.4.3	AFM of Annealed Fe on TiN and Annealed Fe on Si	35
3.5	Summary of TiN Deposition and Its Effectiveness as a Catalyst Support for CNT Growth and Field Emission Applications	37
	REFERENCES	38

4. Synthesis and Characterization of Carbon Nanotubes Grown Using PECVD.....39

4.1	Microwave PECVD System	39
4.2	PECVD GROWTH PROCESS	41
4.2.1	Substrate Treatment	42
4.2.2	TiN Buffer Layer Deposition.....	42
4.2.3	Fe Catalyst Deposition.....	42
4.2.4	Sample Pretreatment for CNT Growth	43
4.2.5	Parameters Used for CNT Growth.....	43
4.3	Characterization of PECVD Grown CNT Films	43
4.3.1	SEM Analysis	44
4.3.2	TEM Analysis	45
4.3.3	Raman Spectroscopy Analysis.....	48
4.4	Summary of PECVD Growth of CNTs and Characterization	49
	REFERENCES	50

5. Field Emission Theory and Characterization51

5.1	Field Emission Theory	51
5.2	Effects of Morphology on Field Emission Properties.....	54
5.3	Field Emission Characterization by the Approach Curve Method	56
5.3.1	Variable Distance Field Emission System.....	57
5.3.2	Threshold Field Determination	59
5.3.3	Field Enhancement Factor Determination	61
5.4	Emission Current Measurements In the Parallel Plate Field Emission System.....	64
5.4.1	Parallel Plate Field Emission System	64
5.4.2	Parallel Plate Field Emission Measurements and Comments on Adsorbate Effects.....	66
5.4.3	Field Emission Stability of CNT Emitters	70
5.5	Field Emission Characterization in the UHV Thermionic/Field Emission System.....	71
5.6	Characterization of CNT Emitters by Field Emission Imaging.....	75
5.7	Growth and Characterization of Carbon Nanoparticles on Metallic Substrates	79

5.7.1	PECVD Growth of CNPs on Fe/TiN/Ti and Fe/TiN/Mo Substrates.....	79
5.7.2	Field Emission Properties of CNPs Grown on Fe/TiN/Ti and Fe/TiN/Mo Substrates.....	85
5.8	Observation of Ring Formations in Field Emission Images.....	87
5.8.1	Jožef Stefan Institute Collaboration.....	89
5.8.2	Theory Behind Ring Structure Formation	90
5.9	Summary of Field Emission Characterization of CNT Films.....	93
	REFERENCES	95
6.	Concluding Remarks	98
6.1	Summary and Results	98
6.2	Suggestions and Future Work.....	100
	REFERENCES	102

LIST OF TABLES

	Page
<i>Table 2.1 Island size and resulting CNT diameter distribution occurring from variations in deposited catalyst thickness.</i>	21
<i>Table 4.1 Pretreatment parameters used for CNT deposition on TiN coated Si substrates.</i>	46
<i>Table 4.2 Growth parameters used for CNT deposition on TiN coated Si substrates.</i>	46

LIST OF FIGURES

	Page
<i>Figure 1.1 Pressure and temperature phase diagram of carbon.</i>	2
<i>Figure 1.2 Structure of single crystal graphite with ABAB stacking.....</i>	3
<i>Figure 1.3 The (n,m) naming scheme of carbon nanotubes as described by the chiral vector C_h.</i>	4
<i>Figure 2.1. Schematic of tip and base growth mechanisms for CNT growth.....</i>	20
<i>Figure 3.1 XPS (Mg Kα) surface spectra identifying Ti and N species in a TiN film deposited on a Si substrate..</i>	26
<i>Figure 3.2 XPS (Mg Kα) spectra of Ti and N content in the as-deposited and UHV annealed (900 °C) TiN films.</i>	28
<i>Figure 3.3 AFM error signal images of a) as-deposited, b) 500 °C and c) 900 °C UHV annealed TiN films on Si substrates.....</i>	29
<i>Figure 3.4 AFM error signal images of a) 900 °C UHV annealed and b) plasma annealed TiN films on Si substrates..</i>	30
<i>Figure 3.5 XPS (Mg Kα) spectra of Si content in as-deposited, plasma annealed, and UHV annealed TiN films.</i>	31
<i>Figure 3.6 AFM error signal image of a 20 nm Fe film annealed on a 25 nm buffer layer of TiN deposited on a Si substrate.....</i>	32
<i>Figure 3.7 Image of a photo electron emission microscope and corresponding schematic showing the inner lens column and screen assembly.</i>	33
<i>Figure 3.8 A series of PEEM images captured during the 2D layer to 3D island-like transition of an Fe film deposited on a TiN coated Si substrate.....</i>	34
<i>Figure 3.9 PEEM images of the annealed Fe films on s TiN coated Si substrate revealing island coalescence.....</i>	35
<i>Figure 3.10 AFM error signal images revealing the transitions of 20 nm Fe films annealed to 900 °C on (a) TiN buffers and (b) Si substrates.</i>	36

<i>Figure 4.1</i>	<i>Schematic of the microwave plasma enhanced chemical vapor deposition system showing the main chamber with heater/sample stage and magnetron head with tunable waveguide.</i>	40
<i>Figure 4.2</i>	<i>Schematic of UHV process and characterization tool (T-line) showing the systems used in this study.</i>	41
<i>Figure 4.3</i>	<i>SEM image of an aligned CNT film grown for 10 minutes on a TiN coated Si substrate.</i>	44
<i>Figure 4.4</i>	<i>a) Schematic of the patterned TiN buffer and blanket Fe catalyst layers used to determine the influence of TiN on the growth of CNTs. The resulting CNT film is shown in (b).</i>	45
<i>Figure 4.5</i>	<i>TEM image of a) large diameter CNTs grown from 20 nm thick catalysts and b) thinner diameter CNTs grown from a 5 nm thick catalyst.</i>	46
<i>Figure 4.6</i>	<i>TEM images of CNT grown from (a) 5 nm Fe catalyst layer and (b) 20 nm Fe catalyst layer.</i>	47
<i>Figure 4.7</i>	<i>Raman spectra of PECVD CNT films grown from 5 nm and 20 nm catalyst layers.</i>	49
<i>Figure 5.1</i>	<i>The surface potential barrier seen by an electron. The metal has a work function of 4.5 eV.</i>	52
<i>Figure 5.2</i>	<i>Schematic diagram of an emitter tip which results in the local field enhancement effect enabling the tunneling of electrons through the potential barrier.</i>	54
<i>Figure 5.3</i>	<i>Schematic of the setup for the variable distance field emission system showing the mechanism of the anode stepper.</i>	57
<i>Figure 5.4</i>	<i>Current vs. voltage sweeps at various 55 μm step sizes for an as loaded CNT film grown on a TiN coated Si substrate.</i>	59
<i>Figure 5.5</i>	<i>Current vs. voltage sweeps at various 55 μm step sizes for a UHV annealed CNT film.</i>	60
<i>Figure 5.6</i>	<i>Plot of the voltage required for extraction of 1 nA of current vs. the relative distance for a CNT film grown on a TiN coated Si substrate.</i>	61
<i>Figure 5.7</i>	<i>F-N plots and corresponding linear fits of the I-V data presented in Fig 5.5.</i>	62

<i>Figure 5.8</i>	<i>A plot of the F-N slopes vs. relative distance which can be used to approximate the field enhancement factor of a CNT film.....</i>	63
<i>Figure 5.9</i>	<i>a) Image and b) schematic of the parallel plate field emission stage.....</i>	64
<i>Figure 5.10</i>	<i>Schematic of the PPFES showing the power supply and computer interface used to collect field emission data.....</i>	65
<i>Figure 5.11</i>	<i>Current vs. voltage plots, for three up/down sweeps, obtained for a CNT film measured in the PPFES.</i>	66
<i>Figure 5.12</i>	<i>Current density vs. applied field plots for a CNT film measured in the PPFES.....</i>	67
<i>Figure 5.13</i>	<i>Current density vs. field plots of a CNT film showing adsorbate effects on the emission behavior.</i>	68
<i>Figure 5.14</i>	<i>F-N plot of a CNT indicating three distinct regions of field emission behavior.</i>	69
<i>Figure 5.15</i>	<i>F-N plots of a CNT film operating in the high (blue), medium (green-magenta), and low (red) current regimes.</i>	70
<i>Figure 5.16</i>	<i>Emission stability of a CNT film deposited on a TiN coated Si substrate.....</i>	71
<i>Figure 5.17</i>	<i>F-N plot of an as loaded CNT film showing the transition on the initial upsweep from an adsorbate induced state to the clean state on the downsweep.....</i>	72
<i>Figure 5.18</i>	<i>Current density vs. applied field for an outgassed (clean) CNT film obtained assuming 1mm (left) and 0.5 mm (right) spacing.....</i>	73
<i>Figure 5.19</i>	<i>F-N plots for an outgassed (clean) CNT film obtained assuming 1mm (left) and 0.5 mm (right) spacing.</i>	74
<i>Figure 5.20</i>	<i>Image of a PECVD grown CNT film on a TiN coated Si substrate, and emission images recorded from the film at various applied fields.....</i>	76
<i>Figure 5.21</i>	<i>Schematic of parallel plate field emission imaging setup.....</i>	76

<i>Figure 5.22 A plot of current density vs. applied field for a CNT film with inserted emission images corresponding to the field at which they were captured.....</i>	78
<i>Figure 5.23 Images of Fe/TiN/Ti (left) and Fe/TiN/Mo (right) substrates after PECVD growth.</i>	80
<i>Figure 5.24 XPS (Mg Kα) analysis of PECVD carbon growth on a Fe/TiN/Ti substrate.....</i>	81
<i>Figure 5.25 Raman spectra of PECVD carbon growth on a Fe/TiN/Ti substrate.....</i>	81
<i>Figure 5.26 XPS (Mg Kα) spectra of Fe pre and post carbon growth on a Fe/TiN/Ti substrate.</i>	82
<i>Figure 5.27 SEM images of nanoparticles grown on a Fe/TiN/Ti substrate.....</i>	82
<i>Figure 5.28 Raman spectra of PECVD carbon growth on a Fe/TiN/Mo substrate.....</i>	83
<i>Figure 5.29 SEM images of carbon nanoparticles grown on a Mo/TiN/Fe coated substrate showing a) transition from deposited area to bare Mo substrate, and b) 10 kX magnified image of carbon nanoparticle structure.....</i>	84
<i>Figure 5.30 Current density vs. applied field for a CNP film deposited on a Fe/TiN/Mo substrate.</i>	85
<i>Figure 5.31 Current density vs. applied field for a CNP film deposited on a Fe/TiN/Ti substrate.</i>	86
<i>Figure 5.32 Emission images captured for a) CNPs grown on a Fe/TiN/Mo coated substrate using a (ZNO) imaging screen and for b) CNPs grown on a Fe/TiN/Mo coated substrate using a (ZNS) imaging screen..</i>	87
<i>Figure 5.33 Emission images of a CNP film grown on a Fe/TiN/Mo coated substrate which reveals the appearance of emission rings indicated by arrows.....</i>	87
<i>Figure 5.34 A series of images showing emission rings obtained using the parallel plate high magnification system.....</i>	88
<i>Figure 5.35 Schematic of the high magnification parallel plate emission imaging setup.....</i>	89

<i>Figure 5.36 Image and schematic of the field emission imaging triode located at the Jožef Stefan Institute.</i>	89
<i>Figure 5.37 Field emission images captured for CNT films using the triode imaging system located at the Jožef Stefan Institute.....</i>	90
<i>Figure 5.38 a) Image of an emission ring from a CNT film, identifying the high level of symmetry associated with the ring structure (a shadow of the extraction grid can be seen in the background) and b) schematic identifying the semi-angle of emission.....</i>	92

1. Introduction

Since their discovery in 1991,¹ carbon nanotubes (CNTs) have been investigated to gain understanding of their unique properties in efforts to establish scientific foundations as well as to optimize their properties for specific applications. Although the abundant research devoted to CNTs has revealed insight into their formation and resulting physical, chemical, and electrical properties, a great deal of additional work must be carried out to uncover many of the phenomena associated with these astonishing nanostructures. CNTs have been employed in many applications ranging from light-weight high-strength composites² to electron sources for flat panel displays.³ The potential applications of these materials include, nano-sized interconnects for microelectronics,⁴ drug delivery for nanomedicine,⁵ hydrogen storage mediums for hydrogen based vehicles,⁶ water filters for the removal of bacteria,⁷ and even far reaching applications such as a lift for a space elevator.⁸

The objective of the first section of this chapter is to provide background on the fundamental aspects that give rise to the unique chemical, physical, and electrical properties of CNTs. Section 2 will present an introduction to vacuum electronics and identify some of the problems associated with the conventional electron emitters of the past. The advantages of CNT based field emitters will be addressed as well as the obstacles faced in their development towards specific applications. A short summary of this introductory chapter is described in section 3 and an overview of this thesis is presented in section 4.

1.1 Background on Carbon Nanotubes

Before introducing CNTs it is important to first discuss the fundamental aspects of their structure which result in their unique properties.

1.1.1 Carbon

Carbon is a column IV element containing six electrons that occupy the $1s^2 2s^2 2p^2$ atomic orbitals. Numerous allotropes of carbon have been identified including diamond, graphite, amorphous carbon, fullerenes and nanotubes. The mixing of the 2s orbitals with the 2px, 2py, and 2pz orbitals gives rise to the sp^2 and sp^3 hybridizations of carbon. It should be noted that carbon is the only column IV element that exhibits both the sp^2 and sp^3 configurations which are characteristic of the graphitic and diamond structures, respectively. As indicated by the carbon phase diagram in Fig. 1.1, graphite is a stable phase of carbon under ambient conditions and is characterized by in-plane trigonal sp^2 bonding. At higher pressures and temperatures, carbon can take on tetrahedral sp^3 bonding forming diamond.

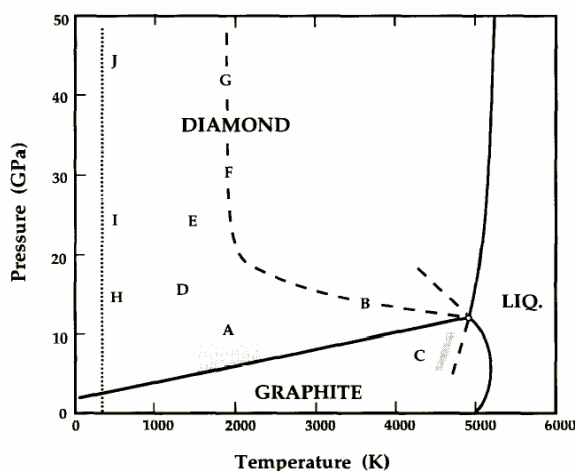


Figure 1.1. Pressure and temperature phase diagram of carbon.⁹

In addition to the bulk phases of carbon such as graphite and diamond, stable nanostructures of carbon have also been identified. The discovery of fullerenes by Kroto et al. in 1985 and ultimately the discovery of carbon nanotubes by Iijima in 1991 have impacted numerous areas of research due to the unique physical, chemical, and electrical properties exhibited by the nanostructured carbon materials.¹⁰ The developments in electron

microscopy, scanning tunneling microscopy and theoretical modeling have revealed that these structures may have many properties similar to graphite such as atomic structure, electrical conductivity, and chemical inertness.

1.1.2 Graphite

The crystal structure of graphite is illustrated in Fig. 1.2. Hexagonal single crystal graphite possesses $P6_3/mmc$ symmetry with ABAB Bernal stacking.

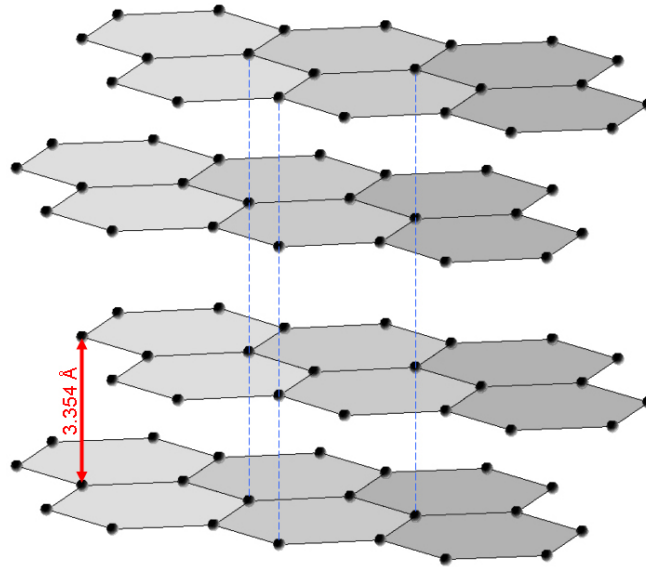


Figure 1.2. Structure of single crystal graphite with ABAB stacking.

The interplanar spacing between the graphite layers is $\sim 3.354 \text{ \AA}$ while the in-plane nearest-neighbor spacing a_{C-C} is $\sim 1.421 \text{ \AA}$.¹¹ Each carbon atom is strongly covalently bonded to its 3 nearest-neighbor atoms exhibiting sp^2 hybridization of the $2p_x$ and $2p_y$ contributions. This strong interplanar bonding gives rise to graphite's high interplanar stiffness, high thermal conductivity, and high melting point. The overlap of the $2p_z$ orbitals attributes to the weak interlayer bonding through van der Waals-like forces. This weak interaction between the layers results in the semi-metallic behavior of graphite along the basal ab plane and reduced electrical conductivity along the c -axis. The weak van der Waals forces between the

graphitic sheets also allow them to slide easily past one another giving rise to the lubricating properties of graphite.

1.1.3 Single-Walled Carbon Nanotubes

As in the case of fullerenes, carbon nanotubes are an alternate configuration of the graphitic state of carbon. An ideal single-walled carbon nanotube (SWCNT) can be described as a graphene sheet rolled into a seamless cylinder. The overall diameter and chirality of the nanotube is typically defined in terms of the chiral vector which runs normal to the nanotube axis. The chiral vector is expressed in terms of the unit vectors a_1 and a_2 in the hexagonal lattice of the graphene sheet where

$$C_h = na_1 + ma_2 \quad (1.1)$$

(See Fig. 1.3).

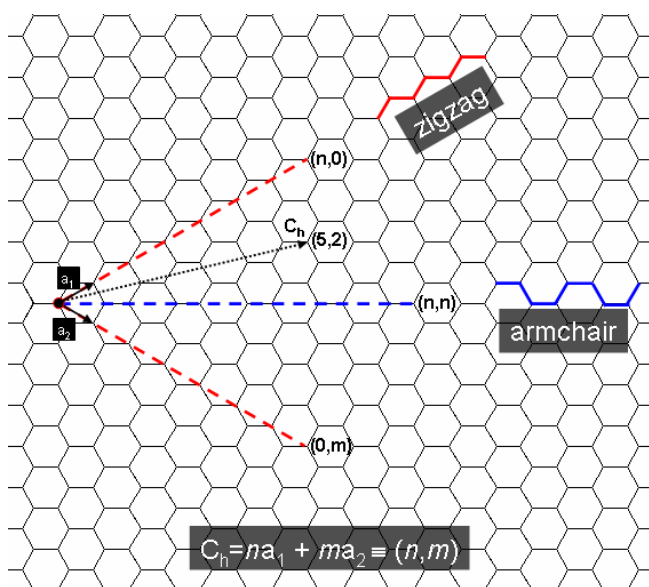


Figure 1.3. The (n,m) naming scheme of carbon nanotubes as described by the chiral vector C_h . Adapted from.¹²

If an atom is chosen as the origin and the graphene sheet is rolled into a cylinder, the chiral vector will point from the origin to the atom that will be crystallographically superimposed

on the origin. The chiral vector can be specified by the integers (n,m) and the diameter of an ideal nanotube can be determined using the relation

$$d_t = \sqrt{3a_{c-c}} \left(m^2 + mn + n^2 \right)^{1/2} / \pi = C_h / \pi, \quad (1.2)$$

where a_{c-c} is the nearest-neighbor distance between carbon atoms in the graphene sheet and m and n are integer values used in the naming scheme outlined in Fig. 1.3.

The chiral angle θ is given by

$$\theta = \tan^{-1} \left[\frac{\sqrt{3}n}{(2m+n)} \right], \quad (1.3)$$

and the “armchair” configuration occurs for $\theta = 30^\circ$ (n,n), while the “zigzag” configuration occurs for $\theta = 0^\circ$ (n,0) or (0,m).

Theoretical calculations have been performed to predict if CNTs exhibiting different chiral structures would be metallic or semiconducting in nature. It has been predicted, and in some cases experimentally observed, that a CNT will have a zero bandgap if

$$(n-m)=3q \quad (1.4)$$

where q is an integer.^{12,13} This suggests that 1/3 of the SWCNTs are metallic while 2/3 are semiconducting.

1.1.4 Multi-Walled Carbon Nanotubes

To this point, only SWCNTs, the simplest structural CNT form, have been discussed. Although SWCNTs are commonly available, CNTs are typically found in the multi-walled (MW) state in which a number of concentric graphitic shells are present in the tube structure. It has been found that MWCNTs contain many stacking faults which result in an increased interlayer distance between concentric graphene sheets when compared to perfect graphite.

Correlation is lost between the graphene sheets in MWCNTs and the resulting structure is similar to what is known as turbostratic graphite.¹⁴

The complex and nearly infinite variations in MWCNT structures poses many challenges when approaching characterization from a theoretical standpoint. In-depth theoretical calculations are typically limited to MWCNTs containing only a few concentric walls. For the most part, MWCNTs exhibit metallic like behavior, especially in the case of larger diameter MWCNTs containing numerous walls.

1.2 Carbon Nanotubes as Field Emitters for Vacuum Electronics

Although CNTs have diverse potential and existing applications, as earlier indicated, the focus of this thesis will be directed towards their use as field emission sources for vacuum electronics.

1.2.1 Vacuum Electronics Based on Thermionic Emitters

Vacuum electronics were significantly influenced by the introduction of the thermionic vacuum tube. In this device, electron emission from a cathode is achieved by heating a metal or a low work function material until a sufficient number of electrons acquire enough kinetic energy to overcome the potential barrier for electron emission. A material's work function significantly influences the temperature required to emit an electron from the material's surface into vacuum. Metals with a high melting point such as tungsten typically have work functions in the range of 4-5 eV requiring temperatures in excess of 1500 K to achieve significant thermionic emission. Although thermionic vacuum tubes and thermionic emitters in general have proven to be successful in many applications, there are also significant drawbacks to these emitters due to the high temperatures needed for operation. Specialized materials and components capable of withstanding the high temperature

operation of the emitters are commonly expensive and can be inconvenient where weight restrictions are enforced as in aeronautic applications. Size reduction of a thermionic based device is typically limited due to thermal expansion issues as well as radiative heating of nearby components. Maintaining satisfactory vacuum conditions for efficient operation also becomes extremely difficult due to the size and operating temperature of the devices. Additionally, rapid turn on and turn off are uncommon to these devices due to the time required to heat and stabilize the emitter as well as cool down the emitter.

1.2.2 Vacuum Electronics Based on Field Emitters

As technology advancements continue to progress, the demand for smaller, faster, more efficient devices increases. As an alternative to the thermionic emitter, field-emission based emitters have been studied. The field emission process involves the tunneling of electrons from a material into vacuum initiated by the application of an electric field. In comparison to thermionic emitters, field-emitters can be smaller, lighter, turned on/off much faster, and are capable of operating over a large range of temperatures.

The diode configuration of a field emission device is the simplest configuration and consists of an emitter (cathode), a vacuum gap, and an anode. With the application of an electric field between the anode and cathode, under proper conditions, electrons can be extracted from the cathode through tunneling processes and in turn be transported across the vacuum gap to the anode. It is more common for field emitters to be operated in a triode mode which makes use of an extraction grid (gate) placed within the vacuum gap of the diode configuration. In this configuration the voltage on the extraction grid can be significantly reduced by placing the grid in close proximity to the cathode. Although a portion of the emitted current will be collected by the grid, one has the ability to select the

accelerating voltage of the uncollected electrons by the addition of a secondary voltage on the anode.

1.2.3 Traditional Field Emitter Structures

Early work on field emission devices identified that sharp metallic tips enabled electron emission at lower applied fields due to what is termed field enhancement. Micro-fabricated metallic tip arrays, commonly fabricated from Mo, have been the basis of high current field emission devices for decades, but these devices suffer from many issues that degrade their operating performance.¹⁵ One of the critical factors limiting the operational stability and lifetime of these metallic emitters is tip degradation due to Joule heating at high emission currents and ion bombardment which leads to erosion and blunting of the tips. Significant damage to the sharp structures alters the field enhancement created by the tips ultimately degrading the performance of the emitter. Obtaining sharper and more robust materials capable of delivering high emission current densities is an ongoing effort. Currently, the most successful application of field emission sources has been in the area of electron microscopy.

1.2.4 Carbon Nanotubes as Field Emission Sources for Vacuum Electronics

The electron emissive properties of CNTs were realized in 1995 inspiring significant research towards field emission applications, which has become one of the most concentrated areas of CNT research.^{16,17} A typical goal of field emission for both research and industry is to develop a material that is capable of emitting a significant electron current into vacuum under the application of a small voltage. The specific properties of CNTs that are favorable for field emission are their high conductivity, high mechanical strength, high melting point, chemical inertness, and very small diameter to length ratio. The geometric field

enhancement effects induced by CNTs have been found to significantly lower the macroscopic threshold fields required for electron emission. The local amplification of the applied electric field at the CNT tips, enabled by their unique geometrical structure, is the critical factor that inspired and continues to direct CNT research towards field emission applications. In addition to their field enhancement capabilities, the sputter resistance of carbon based materials has been found to be an order of magnitude greater than that of Mo.¹⁸ The properties exhibited by CNTs are essential in overcoming some of the challenges faced with the development and efficient operation of field emission sources as electron emitters.

A significant obstacle impeding the progress towards the development of effective field emission devices based on CNT films is the difficulty achieving controlled growth of the materials over large substrates. Some of the factors leading to these difficulties are the high temperatures necessary for nucleation and growth as well as limitations on the substrates that can be used. Additionally, CNTs have been found to have emission stability issues which are often attributed to the removal and absorption of gas species that enhance or impede the emission characteristics of the films. The removal or stabilization of adsorbates on CNT emitters and the development of new materials for CNT growth are of critical importance in overcoming the challenges of employing CNTs as field emission sources. This is especially critical for vacuum microelectronic applications that are significantly sensitive to instabilities and non-uniformities in emission.

1.3 Summary of CNT Properties and Applications Towards Vacuum Electronics

In summary, it has been shown that CNTs possess many qualities that are attractive for field emission applications. Their metallic like behavior, high temperature capabilities, chemical inertness, small diameter to length ratios, and high erosion resistance to ion

bombardment make them an ideal emitter for vacuum electronic applications. CNTs have the potential, in many applications, to replace conventional thermionic emitters and solve many of the issues associated with field emitters based on metallic tips. The research reported in this thesis was carried out in efforts to further advance the science and technology associated with the growth and implementation of CNTs as effective electron emitters in vacuum electronic applications.

1.4 Overview of Thesis

The goal of this thesis is two fold. First I will focus on the implementation of TiN buffer layers on Si substrates for CNT growth and field emission applications. Chapter 2 will give a general background on the various synthesis techniques developed for CNT production. This chapter will highlight the advantages of catalytic chemical vapor deposition techniques and comment on the proposed catalytic growth mechanisms of CNTs. Chapter 3 will identify the properties of TiN that are favorable for enhancing CNT growth capabilities while maintaining a favorable substrate-buffer layer structure for field emission applications. The deposition of TiN using plasma assisted reactive evaporation will be summarized and results of film characterization such as composition, barrier properties, resistivity, and thermal stability will be addressed. The first section of chapter 4 will give an overview of the plasma enhanced chemical vapor deposition (PECVD) system used in this work and identify the advantages this technique has to offer for the production of CNTs. The second section of chapter 4 will summarize the PECVD growth of CNTs, including substrate preparation, TiN buffer layer deposition, catalyst deposition, sample pretreatment, and growth parameters. The third section of chapter 4 is devoted to the characterization of the resulting CNT films by SEM, TEM, and Raman spectroscopy.

Secondly, in addition to the growth of CNTs on TiN coated Si substrates, characterization of the field emission properties of these films will be discussed. Section 1 of chapter 5 will give an introduction to field emission theory. Section 2 will comment on the various aspects of field enhancement structures that enable extraction of electron from a material at moderate applied fields. Section 3 through 6 of chapter 5 will describe and give the experimental results of four field emission systems used to characterize the CNT films. Specifically, three systems, the variable distance field emission system, parallel plate field emission system, and thermionic/field emission system will be used to electrically characterize the field emission properties of the CNT films. Comments will be made on the field emission performance of the films as well as adsorbate effects that alter their emission behavior. The last system, the field emission imaging system, will be used to characterize the emission distribution from the films in order to gain an understanding of the emission uniformity.

It should be noted that attempts to grow CNT films on metallic substrates utilizing the TiN buffers resulted in the growth of carbon nanoparticles (CNPs) which exhibited unique physical and field emission properties. A short summary of this work will be presented in section 7 of chapter 5. Additionally, a collaboration with researchers from the Jožef Stefan Institute was developed to investigate unique structures observed in the emission images from the CNT and CNP films. This introductory work is summarized in section 8 of chapter 5. Chapter 6 will summarize the results obtained from the work presented in this thesis and offer suggestions for future work.

REFERENCES

- 1 S. Iijima, *Nature* **354** (6348), 56 (1991).
- 2 B. Lahr and J. Sandler, *Kunststoffe-Plast Europe* **90** (1), A94 (2000).
- 3 J. M. Kim, W. B. Choi, N. S. Lee et al., *Diamond and Related Materials* **9** (3-6), 1184 (2000).
- 4 A. Naeemi, R. Sarvari, and J. D. Meindl, *Ieee Electron Device Letters* **26** (2), 84 (2005).
- 5 A. Bianco, K. Kostarelos, and M. Prato, *Current Opinion in Chemical Biology* **9** (6), 674 (2005).
- 6 H. M. Cheng, Q. H. Yang, and C. Liu, *Carbon* **39** (10), 1447 (2001).
- 7 A. Srivastava, O. N. Srivastava, S. Talapatra et al., *Nature Materials* **3** (9), 610 (2004).
- 8 B. Iannotta, *Aerospace America* **44** (3), 30 (2006).
- 9 F. P. Bundy, W. A. Bassett, M. S. Weathers et al., *Carbon* **34** (2), 141 (1996).
- 10 H. W. Kroto, J. R. Heath, S. C. Obrien et al., *Nature* **318** (6042), 162 (1985).
- 11 Thomas Ebbesen, *Carbon Nanotubes Preparation and Properties*. (CRC Press, New York, 1997).
- 12 R. Saito, M. Fujita, G. Dresselhaus et al., *Applied Physics Letters* **60** (18), 2204 (1992).
- 13 N. Hamada, S. Sawada, and A. Oshiyama, *Physical Review Letters* **68** (10), 1579 (1992).
- 14 M.S. Dresselhaus, *Carbon Nanotubes Synthesis, Structure, Properties, and Applications*. (Springer, New York, 2001).
- 15 George Fursey, *Field Emission in Vacuum Microelectronics*. (Springer, 2005).
- 16 W. A. Deheer, A. Chatelain, and D. Ugarte, *Science* **270** (5239), 1179 (1995).
- 17 A. G. Rinzler, J. H. Hafner, P. Nikolaev et al., *Science* **269** (5230), 1550 (1995).
- 18 Y.K Yap, J Menda, L Venga et al., presented at the Materials Research Society Symposium, Warrendale PA, 2004 (unpublished).

2. Synthesis of CNTs-General Principles and Methods

This chapter will provide a background on the various techniques and methods developed over the years for the synthesis of CNTs. The role of transition metal catalyst particles in catalytic chemical vapor deposition (CVD) of CNTs will be addressed. In addition, comments will be made on the proposed CNT growth mechanisms.

2.1 Overview of Synthesis Techniques

The discovery of fullerenes produced by carbon arc-discharge techniques eventually led to the first observations of carbon nanotubes by Iijima in 1991.¹ The increased involvement in CNT research has resulted in the development of a number of synthesis techniques that possess particular advantages in the production of CNTs for specific applications. The two general categories that CNT synthesis techniques fall under are the catalytic and non-catalytic processes. Transition metal catalysts, typically Fe, Co and Ni, have been used for the production of CNTs due to their hydrocarbon decomposition capabilities. Although a number of CNT synthesis techniques are in existence, the three most common production methods found today are arc-discharge, laser-ablation and chemical vapor deposition.

2.1.1 Arc-discharge

One of the simplest methods to produce CNTs is by the arc-discharge technique. In this technique, two electrodes, commonly graphite, are brought into close proximity under an applied voltage. This is typically carried out in the presence of an inert gas such as helium at a pressure of around 200 torr. When the separation distance between the electrodes becomes very small, arcing can occur resulting in the formation of a plasma between the two

electrodes. The high temperature generated within the plasma evaporates carbon atoms from the anode and deposits them on the cathode.

The resulting CNT yield has been found to depend on the deposition pressure as well as the current flow between the two electrodes.² The reaction products from this technique commonly contain ~70% multi-walled (MW) CNTs while the bi-products are typically multi-layered graphitic particles.³ The resulting products are of lab-scale quantities and typically require collection and purification processes such as that developed by Smalley and coworkers.⁴

While the non-catalytic arc-discharge process only results in MWCNTs, it was found that SWCNTs can be produced by arc-discharge techniques through the incorporation of a metal catalyst into the anode. Iijima and Ichihashi reported the evaporation of the metal into a vapor favored the formation of SWCNTs over MWCNTs.⁵

2.1.2 Laser Ablation

The laser-ablation technique utilizes an intense laser to vaporize a carbon target containing a low percentage of transition metal. This process is typically carried out in a high temperature furnace, and the resulting products have been found to consist of SWCNTs, while the bi-products commonly contain fullerenes, carbon nanoparticles and additional contaminants. Guo et al. were successful in producing gram quantities of SWCNTs using this technique.⁶ As for the case of CNTs produced using the arc-discharge method, a collection and purification process is required to obtain the SWCNT products.

2.1.3 Chemical Vapor Deposition

Chemical vapor deposition (CVD) methods to produce CNTs involve the decomposition of a hydrocarbon or carbon containing feedstock in the presence of catalyst

particles at an elevated temperature. A variety of CVD techniques have been developed for the growth of CNTs since the first report in 1993 by Jose-Yacaman.⁷ In general, the catalyst can be either supported or floating during the CVD reaction process to form CNTs. Large scale production of CNTs typically use the floating catalyst methods in which the reactive catalyst is not directly bound to a substrate. For example, thermal decomposition of ferrocene in metalorganic chemical vapor deposition (MOCVD) and fluidized bed CVD methods have succeeded in producing mass quantities of high quality CNTs.⁸ Although these methods can be used to easily produce large quantities of CNTs, selected deposition of the products is typically achieved only after collection, purification and transfer of the product materials to a substrate through processes such as screen printing. These deposition techniques are preferred for applications that require large quantities of randomly oriented CNTs as in the case of lightweight high-strength composite materials.

Chemical vapor deposition utilizing a supported catalyst offers the advantage of controlled and selective growth of CNTs on a substrate. This technique is preferred for the fabrication of microelectronic devices, sensors, filters, field emitters and other applications where patterned growth is essential. Thermal and plasma enhanced CVD synthesis techniques have emerged as the leading catalytic growth methods capable of providing the tightest control on the direct growth of CNTs on pre-patterned substrates. Both methods have successfully produced highly ordered and aligned CNT films which are not achievable by the other previously noted deposition methods.

In comparison to synthesis of CNTs by thermal CVD, plasma enhanced chemical vapor deposition (PECVD) has demonstrated the capability to improve the alignment of CNT films as well as enable reduced growth temperatures. It has been reported that alignment of

CNT films during thermal CVD growth is attributed to crowding and van der Waals effects.⁹ The improvements in alignment using PECVD have been attributed to the electrical field effects induced by the plasma environment resulting in CNTs that grow perpendicular to the substrate surface.¹⁰ Additionally, the generation of highly reactive radicals, produced in the plasma assisted dissociation of hydrocarbon gasses, can account for the lower growth temperature capabilities.

2.2 Transition Metal Catalysts for CNT Growth

The production of CNTs by CVD techniques utilize transition metal catalysts to assist in the decomposition of hydrocarbons or other carbon sources. The tubular and graphitic nature of CNTs arises from mechanisms carried out by the catalyst.¹¹ The size and shape of catalyst nanoparticles has been found to significantly influence the production of CNTs, therefore the activity of the catalyst not only depends on type, but structure as well.¹²

2.2.1 Catalyst Types and Deposition Techniques

The three predominant catalysts used in the CVD growth of CNTs are Fe, Co and Ni. There are various methods used to prepare catalysts for CNT growth such as the sol-gel method, co-reduction of precursors, and metalorganic chemical vapor deposition, but the scope of this research focuses on physical deposition techniques such as sputtering or evaporation which are common to the microelectronic industry.¹³

Room temperature deposition of the catalyst metals by physical deposition methods generally results in an even distribution of amorphous material over the substrate surface. It has been reported that the formation of catalyst nanoparticles is critical for supported catalytic growth of CNTs.¹⁴ Upon annealing of the amorphous catalyst films, nanoparticle formation is typically achieved at temperatures of ~ 600 °C. The size and distribution of the

catalyst nanoparticles depends on a number of inter-related factors which have given rise to the large number of diverse growth recipes and results reported by the research community. Among the most significant factors are the catalyst thickness¹², the catalyst/support interface,¹⁵ and the annealing environment/method.¹⁶

2.2.2 Catalyst Activity

Among the three common transition metal catalysts, Fe, Co, and Ni, Fe has generally been found to be the most active of the catalysts for producing CNTs. Although Fe has typically been found to produce the highest densities of CNTs, there have been reports that a higher degree of graphitization is achieved when Co is used.¹³ In addition to pure metals, metal alloys or multi-layer catalysts are known to influence the catalytic activity improving product yield and lowering reaction temperatures.

2.2.3 Catalyst Nanoparticle Formation

The catalyst support, in most cases the substrate, has been found to significantly influence the properties of catalyst nanoparticle formation such as the shape and size. Thin metal films of high surface energies tend to transform from 2-D layers to 3-D islands when annealed on low surface energy supports. The island formation effectively reduces the surface to volume ratio of the high surface energy film in addition to exposing more of the low surface energy support.

The size and density of the catalyst particles has been found to directly depend on the thickness of the deposited material.¹² The general trend commonly observed is that the thinner the deposited catalyst layer is, the smaller the resulting particles will be after annealing. The ability to produce SWCNTs and MWCNTs using the same CVD technique has been enabled with the ability to control of the size and distribution of catalysts particles.

Considerable attention must be given to the annealing process as the growth of larger particles may result due to secondary interactions such as ripening or coalescence which develop during longer annealing times and/or higher temperatures.

The activity of the Fe, Ni, or Co catalysts can be strongly influenced by the support layer especially if the catalyst forms a compound with or diffuses into the substrate. In efforts to preserve or improve the activity and tailor the size and distribution of catalyst nanoparticles, various buffer layers such as SiO₂, TiN, Al, Al₂O₃ and TiO₂ have been implemented into the catalyst support structures.¹⁷ The likelihood of metals to form a silicide or diffuse into Si substrates presents significant challenges in the fabrication of CNT based devices. The significance of this issue becomes of greater concern as the catalyst film approaches sub-nanometer thicknesses typically required for thin or SWCNT growth. SiO₂, widely used in device fabrication processes, is the most commonly reported buffer/barrier layer for CNT growth. Although, implementation of SiO₂ as a barrier layer has resulted in the abundant success of CNT growth, including SWCNTs, the significance is typically academic when considering device fabrication from a field emission standpoint due the inherent insulating properties of the SiO₂ layer. It is for this reason, alternative barrier layers such as TiN are essential to the fabrication processes due to their high conductive nature.

2.3 Growth Mechanisms of CNTs

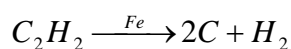
Although significant contributions have been made towards improving and controlling the growth of CNTs, comprehensive details of the actual growth mechanisms still remain poorly understood. It is presumed that the nucleation and growth of CNTs corresponds to other known processes in which graphitic structures are produced from the catalytic decomposition of carbon-containing precursors. The earlier work of carbon

filament growth from catalytic particles by Baker et al. closely resembled the behavior observed for CNT growth.¹⁸ Adaptations of Baker's model have been made to account for CNT growth and it is widely accepted that the general stages of growth involve: 1) the dissociation of hydrocarbons on the catalyst surface; 2) diffusion of carbon on and into the bulk of the catalyst; 3) precipitation of carbon out of the catalyst; and 4) the assembly of carbon atoms into an sp^2 tubular structure.¹⁹

2.3.1 Hydrocarbon Decomposition by Catalyst Nanoparticles

The aforementioned catalysts, Fe, Ni, Co enable carbon to diffuse through and over the metals allowing the formation of ordered carbon by a mechanism of diffusion and precipitation. The formation of the graphitic structures must therefore occur in close proximity to the metal's surface as deposition of carbon away from the catalyst will be in the amorphous state.

It has been reported that acetylene is thermally stable at temperatures below 800 °C.²⁰ The dissociation of acetylene at lower temperatures by catalyst particles, for example Fe, has been found to occur at a temperature of 127 °C.²⁰



Although it is possible to dissociate acetylene at 127 °C, the diffusion of carbon into bulk Fe is limited at temperatures less than 500 °C.²¹ This may explain the common temperature window of ~500 °C – 900 °C for CNT growth and the difficulty in achieving low temperature growth even with the assistance of plasma enhancement.

2.3.2 CNT Growth Modes

The two general growth modes exhibited by CNTs synthesized by supported catalytic CVD are described as tip and base growth.

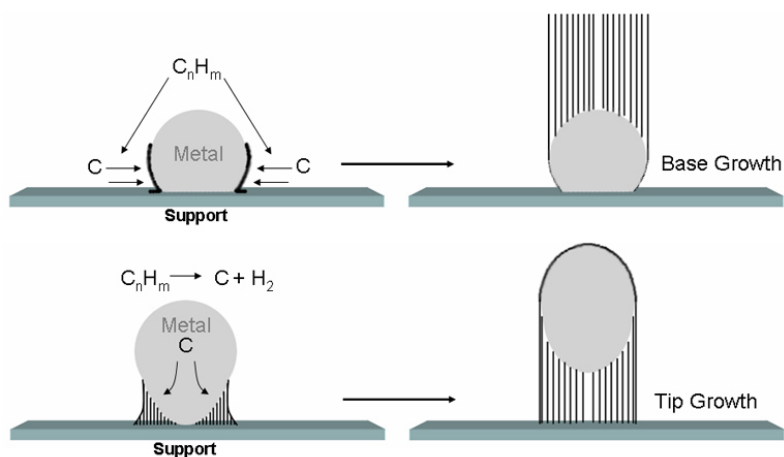


Figure 2.1. Schematic of tip and base growth mechanisms for CNT growth. Adapted from.¹⁹

It has been suggested that the adhesion between the catalyst particle and its support is the major factor that governs the outcome of the growth mode. The tip and base growth mechanisms are presented in Fig. 2.1. In the case of base growth, also referred to as root growth, the catalyst particle is strongly bound to the substrate and the CNT grows from the top of the catalyst particle. In the tip growth mechanism, the catalyst particle is weakly bound to the substrate and as carbon leaves the particle, the particle is lifted up as CNT growth proceeds. It is still unclear whether the selective precipitation of carbon occurs due to temperature or concentration gradients within the catalyst.^{20,22} In all supported catalyst cases, it should be noted that it is the support layer that breaks the symmetry of the system.

2.3.3 Surface Vs. Bulk Diffusion of Carbon and Effects on CNT Growth

It is postulated that variations of the bulk and surface diffusion of carbon into and on the catalyst particles contributes to the variety of CNT and CNT-like structures observed including carbon fibers, bamboo structured MWCNTs, hollow MWCNTs, and SWCNTs. These structures are typically characterized by the orientation of the graphitic basal planes within the structure. Larger filaments, produced from large catalyst particles, are known to

have the basal planes oriented tangential to the catalyst surface. As the catalyst particle size decreases, the radius of curvature decreases imposing increasing strain on the basal planes within the larger filament structures. Eventually it becomes more favorable to form continuous surfaces resulting in MWCNT growth. Further reduction in catalyst particle size eventually leads to the formation of SWCNTs.¹⁹

Bulk-diffusion of carbon in the catalyst particle must take place for MWCNT or carbon fiber growth because surface diffusion alone can not account for their unique internal structures. In the case of large particles, the surface area to volume ratio is small which can explain the why bulk diffusion is favorable. Smaller catalyst particles having a larger surface area to volume ratio typically result in the thinner and hollow CNTs whose structures can be explained by surface diffusion contributions.

Wang et al. reported on the island formation of Fe particles on SiO₂ as a function of film thickness, and noted the resulting CNT structures grown from the films.²³

*Table 2.1. Island size and resulting CNT diameter distribution occurring from variations in deposited catalyst thickness.*²³

Fe film thickness (nm)	Island size (~nm)	Nanotube diameter (~nm)
20	200–600	100–300
10	100–200	30–120
5	60–120	30–100
2	30–60	15–30
1	30–50	5–15
0.3–0.5	10–15	1–5

The internal structure of the CNTs grown from the various Fe catalyst thicknesses was found to change from the bamboo-structure for thick catalyst films (>5 nm) to a distribution of hollow and bamboo structures for thinner films, and to hollow tubes for catalyst films thinner

than 2 nm. It was also noted in this work that PECVD growth of SWCNTs was achieved using 0.3-0.5 nm catalyst films.

Generally it is accepted that contributions of both surface and bulk diffusion are responsible for the observed variations in CNT growth, although there are a number of authors that argue differently. A summary of alternate growth mechanisms proposed by various authors can be found in a report by Kuznetsov.²⁴

2.4 Summary of CNT Synthesis

It was shown that since their discovery, active involvement in CNT research has led to the development of various synthesis techniques such as arc-discharge, laser ablation, and CVD. A wide variety of growth recipes and sample treatments have also been developed for CVD techniques to optimize supported transition metal catalysts for various growth results. PECVD has shown to be a flexible technique to provide proper conditions to grow a variety of CNTs including MWCNTs and SWCNTs.

REFERENCES

- ¹ S. Iijima, *Nature* **354** (6348), 56 (1991).
- ² M. Cadek, R. Murphy, B. McCarthy et al., *Carbon* **40** (6), 923 (2002).
- ³ Thomas Ebbesen, *Carbon Nanotubes Preparation and Properties*. (CRC Press, New York, 1997).
- ⁴ J. Liu, A. G. Rinzler, H. J. Dai et al., *Science* **280** (5367), 1253 (1998).
- ⁵ S. Iijima and T. Ichihashi, *Nature* **363** (6430), 603 (1993).
- ⁶ T. Guo, P. Nikolaev, A. Thess et al., *Chemical Physics Letters* **243** (1-2), 49 (1995).
- ⁷ M. Joseyacaman, M. Mikiyoshida, L. Rendon et al., *Applied Physics Letters* **62** (6), 657 (1993).
- ⁸ A. Barreiro, S. Hampel, M. H. Rummeli et al., *Journal of Physical Chemistry B* **110** (42), 20973 (2006).

- ⁹ H. Cui, G. Eres, J. Y. Howe et al., *Chemical Physics Letters* **374** (3-4), 222 (2003).
- ¹⁰ C. Bower, W. Zhu, S. H. Jin et al., *Applied Physics Letters* **77** (6), 830 (2000).
- ¹¹ F. H. Kaatz, M. P. Siegal, D. L. Overmyer et al., *Applied Physics Letters* **89** (24), 3 (2006).
- ¹² S. Hofmann, M. Cantoro, B. Kleinsorge et al., *Journal of Applied Physics* **98** (3), 8 (2005).
- ¹³ A. C. Dupuis, *Progress in Materials Science* **50** (8), 929 (2005).
- ¹⁴ M. Meyyappan, L. Delzeit, A. Cassell et al., *Plasma Sources Science & Technology* **12** (2), 205 (2003).
- ¹⁵ T. de los Arcos, F. Vonau, M. G. Garnier et al., *Applied Physics Letters* **80** (13), 2383 (2002).
- ¹⁶ M. Cantoro, S. Hofmann, S. Pisana et al., *Diamond and Related Materials* **15** (4-8), 1029 (2006).
- ¹⁷ T. de los Arcos, M. G. Garnier, P. Oelhafen et al., *Carbon* **42** (1), 187 (2004).
- ¹⁸ R. T. K. Baker, *Carbon* **27** (3), 315 (1989).
- ¹⁹ S. B. Sinnott, R. Andrews, D. Qian et al., *Chemical Physics Letters* **315** (1-2), 25 (1999).
- ²⁰ C. Klinke, J. M. Bonard, and K. Kern, *Physical Review B* **71** (3), 7 (2005).
- ²¹ W. H. Hung and S. L. Bernasek, *Surface Science* **339** (3), 272 (1995).
- ²² M. Grujicic, G. Cao, and B. Gersten, *Materials Science and Engineering B-Solid State Materials for Advanced Technology* **94** (2-3), 247 (2002).
- ²³ Y. Y. Wang, S. Gupta, R. J. Nemanich et al., *Journal of Applied Physics* **98** (1), 6 (2005).
- ²⁴ V. L. Kuznetsov, A. N. Usoltseva, A. L. Chuvilin et al., *Physical Review B* **64** (23), 7 (2001).

3. TiN Buffer Layers Used as a Catalyst Support for CNT Growth

This chapter discusses the use of TiN as a catalyst support layer for CNT growth. The TiN films were deposited by plasma assisted reactive evaporation (PARE) and characterized by a number of techniques to validate the use of TiN layers to assist in the growth of CNTs. The electrical properties of the TiN films were investigated for their use in support structures for field emission devices based on CNT emitters.

3.1 General Applications of TiN

Various applications have taken advantage of the unique chemical, physical and electrical properties of TiN. The gold-like color of TiN is well suited for decorative coatings while its high corrosion resistance, high hardness, and low friction coefficient have been applied to biomedical applications as well as coatings for high-speed cutting tools.¹ The thermal stability, diffusion barrier properties and high conductivity of TiN have impacted the microelectronics industry specifically in device fabrications processes carried out on Si. Traditionally TiN has been employed as a diffusion barrier preventing the interaction between metals such as aluminum and copper with adjacent layers during high temperature and annealing processes.^{2,3,4}

3.2 Depositon of TiN by Plasma Assisted Reactive Evaporation

The synthesis of TiN films is typically carried out using two main processes. The first involves the diffusion of nitrogen into a Ti matrix while the second, used in this work, involves the formation of TiN in a gaseous state prior to deposition onto a substrate. In this study, TiN films were deposited using a plasma assisted reactive evaporation (PARE) system typically maintained a base pressure of 1×10^{-9} torr by a turbomolecular pump. The deposition process consisted of the electron beam evaporation of a Ti source within the

proximity of a nitrogen plasma. The evaporation of the Ti source was carried out at in a reactive nitrogen atmosphere generated by the local plasma, and a deposition pressure of 1×10^{-5} torr was regulated using a turbomolecular pump. The rf plasma source, manufactured by SVT, was optimized for the production of atomic nitrogen rather than the formation of the less reactive molecular and ionic species of nitrogen. Si wafers were used as substrates and the substrate temperature was typically maintained at ~ 300 °C during the deposition process. In the deposition process, the evaporated Ti reacts with atomic nitrogen produced by the RF plasma prior to deposition on the substrate surface. It should be noted that at the deposition pressures of $\sim 1 \times 10^{-5}$ torr, nitrogen would become the limiting reactant in the formation of TiN if the Ti evaporation rate was set too high.

3.3 Characterization of PARE Deposited TiN Films

It has been found that oxygen can significantly affect the desirable electrical and physical properties of TiN films.⁵ Under a Ti deposition rate of 0.5 \AA/s at the aforementioned pressure of 1×10^{-5} torr, X-ray photoelectron spectroscopy (XPS) analysis utilizing a Mg K α (1253.6 eV) X-ray source revealed that the TiN films had little oxygen contained in the film (peak signal detected slightly above the noise level). The majority of the oxygen observed in the XPS spectra is attributed to originate from the surface layer. Figure 3.1 shows the XPS surface spectra of the as-deposited TiN film.

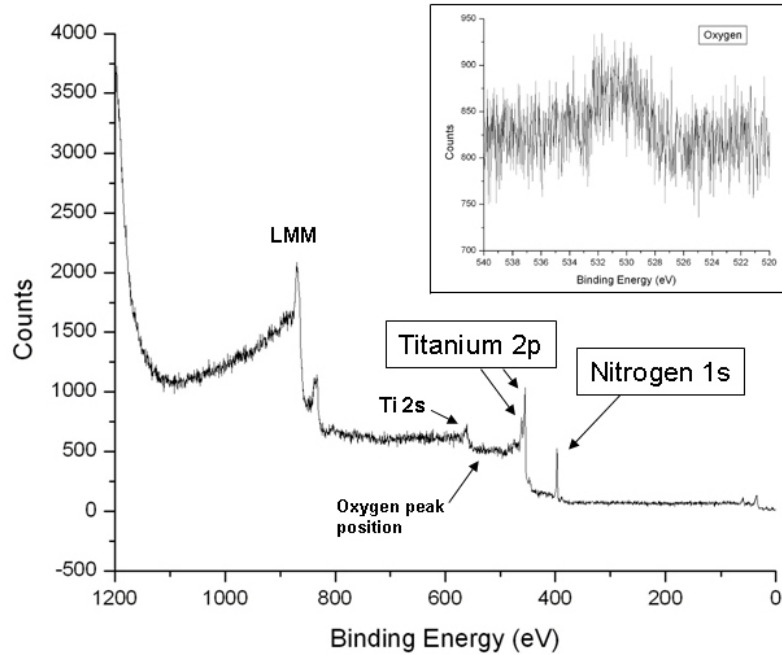


Figure 3.1. XPS ($Mg K\alpha$) surface spectra identifying Ti and N species in a TiN film deposited on a Si substrate. Little oxygen content is detected in the magnified region of the spectra (top right inset).

Four-point probe measurements of as-deposited TiN films resulted in sheet resistance values of $\sim 43 \Omega/\square$ corresponding to film resistivities of $\sim 140 \mu\Omega\text{-cm}$ which were in good agreement with reported values.¹

XPS quantitative analysis of the deposited TiN films revealed that they were nearly stoichiometric with a nitrogen to Ti ratio of approximately 1. The analysis was performed utilizing peak area sensitivity factors for an X-ray source oriented 90° to the sample surface. For a homogeneous sample, the number of photoelectrons per second in a specific spectra peak is given by:

$$I = nf\sigma\theta y\lambda AT \quad (3.1)$$

where n is the number of atoms of the element per cm^3 , f is the x-ray flux, σ is the photoelectric cross-section for the atomic orbital, θ is an angular efficiency factor based on the instrumental arrangement, y is the efficiency in the photoelectric process for formation of

photoelectrons of the normal photoelectron energy, λ is the mean free path of the photoelectrons in the sample, A is the area of the sample from which the photoelectrons are detected, and T is the detection efficiency for electrons emitted from the sample. Equation 3.1 can be rearranged to solve for the number of atoms of a specific element per cm^3 of the sample:

$$n = \frac{I}{f\sigma\theta y\lambda AT} \quad (3.2)$$

Here the denominator is defined as the sensitivity factor, S which has been determined for specific elements based on empirical data.⁶ Taking the ratio of the number of atoms of nitrogen to the number of atoms of Ti per cm^3 of the as-deposited sample, the nitrogen to Ti content was found to be ~0.9.

$$\frac{n_N}{n_{Ti}} = \frac{I_N}{I_{Ti}} \frac{S_{Ti}}{S_N} = \frac{(\sim 1790)(1.798)}{(\sim 7240)(0.477)} \approx 0.9 \quad (3.3)$$

It should be noted that the sample remained in UHV after deposition of the TiN film and was not removed prior to XPS measurements. This prevented the contamination of the surface of the film by exposure to atmosphere. In addition to the as-deposited films, XPS measurements were performed for films annealed at 500 °C and 900 °C in vacuum.

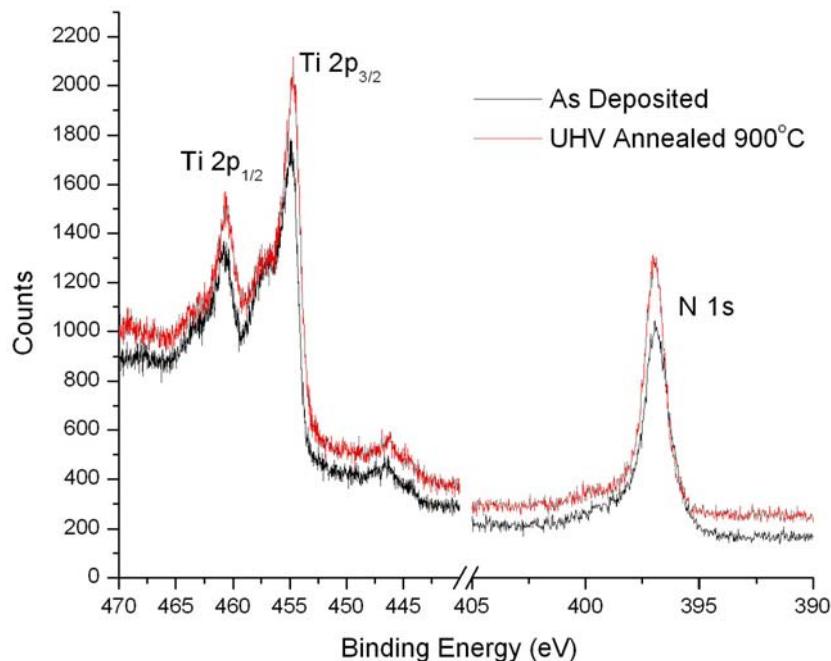


Figure 3.2. XPS ($Mg\ K\alpha$) spectra of Ti and N content in the as-deposited and UHV annealed ($900\ ^\circ C$) TiN films.

While films annealed to $500\ ^\circ C$ in vacuum showed little compositional change, a small decrease in the relative N/Ti peak area for the $900\ ^\circ C$ annealed films was observed. This resulted in a N/Ti content of ~ 0.8 (see Fig. 3.2.).

While there was no Si observed in the XPS spectra of the as-deposited and $500\ ^\circ C$ annealed films, it should be noted that Si was detected in the XPS spectra for the sample annealed to $900\ ^\circ C$. This indicated the possible exposure of Si occurring through voids such as pinholes in the TiN surface or diffusion of Si to the surface occurring along grain boundaries in the film.

To investigate the surface structure of the TiN films, atomic force microscopy (AFM) images were obtained for the as-deposited, $500\ ^\circ C$, and $900\ ^\circ C$ UHV annealed films.

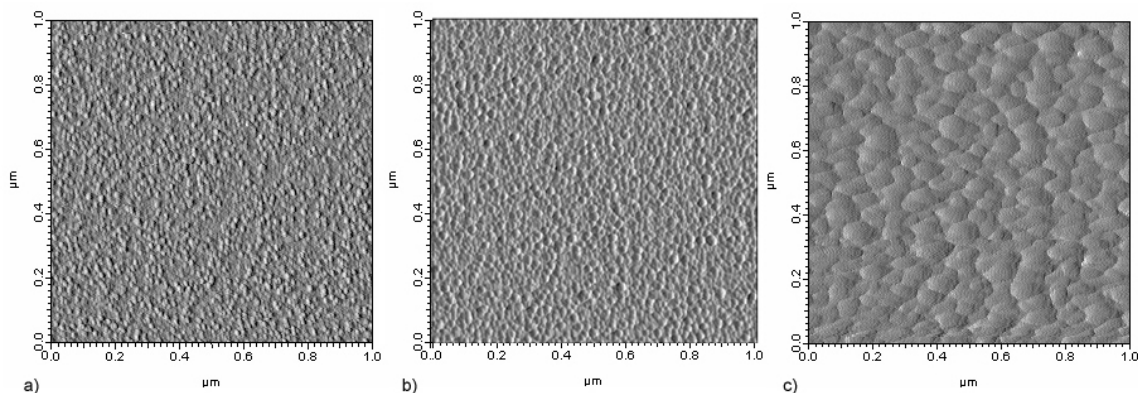


Figure 3.3. AFM error signal images of a) as-deposited, b) 500 °C and c) 900 °C UHV annealed TiN films on Si substrates. (Images acquired in contact mode using SiN tips).

Very little change in morphology was observed to occur for samples annealed to 500 °C in UHV. Upon annealing the TiN films to 900°C, a significant morphological change occurred as evidenced in Fig. 3.3 (c). An agglomerated structure resulted, which can have an impact on the barrier properties of the TiN film.

The thermal stability of TiN diffusion barriers in multi-layer contacts to Si has been reported by various authors. Suni et al. found that the interdiffusion of Si with Pd, Cu, and Au layers deposited on Si substrates containing reactively sputtered TiN diffusion barriers occurred at temperatures of ~650 °C.⁷ Gao et al. reported that for Ag/TiN/Si structures, the reactively sputtered TiN films were stable up to temperatures of 600 °C.⁸ de los Arcos, found that the barrier properties of TiN films deposited by biased reactive sputtering were improved due to densification of the TiN films occurring due to biasing.⁹ He reported that a thin layer of dense TiN between the Si substrate and Fe film prevented the interdiffusion of Fe and Si up to temperatures approaching 850 °C.

The annealed films in Fig. 3.3 and those reported by de los Arcos, Gao, and Suni were carried out under high vacuum annealing conditions. It should be noted that variations in annealing conditions such as plasma treatment have been found to influence the resulting

morphological changes that a system may undergo.¹⁰ In efforts to reproduce annealing conditions similar to those used for PECVD growth of CNTs, 25 nm PARE deposited TiN films were annealed to 900 °C using a C₂H₂:NH₃ plasma. AFM images of the plasma annealed films shown in Fig. 3.4 revealed that the surface structure was significantly different from the agglomerated surface of the UHV annealed films.

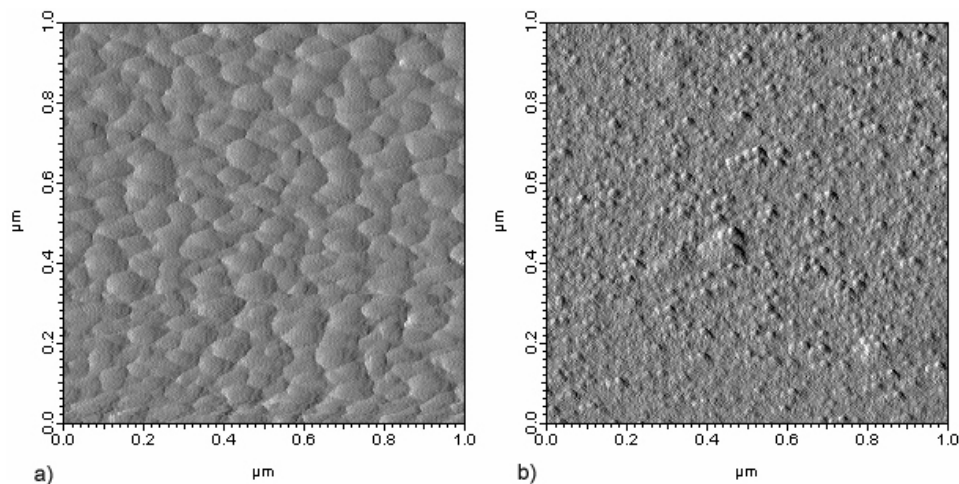


Figure 3.4. AFM error signal images of a 900 °C a) UHV annealed and b) plasma annealed TiN films on Si substrates. (Images acquired in contact mode using SiN tips).

These results indicate that TiN films annealed in a C₂H₂:NH₃ plasma may possess a higher thermal stability due to secondary reactions occurring with the feed gasses or that the surface of the film may be altered due to etching by the plasma. Similar results have been reported identifying that TiN films annealed in a N₂ atmosphere showed higher stability than those annealed to the same temperature in vacuum.¹¹

XPS was used to study the surface chemistry of the plasma annealed films and comparisons were made to films annealed to the same temperature under UHV conditions.

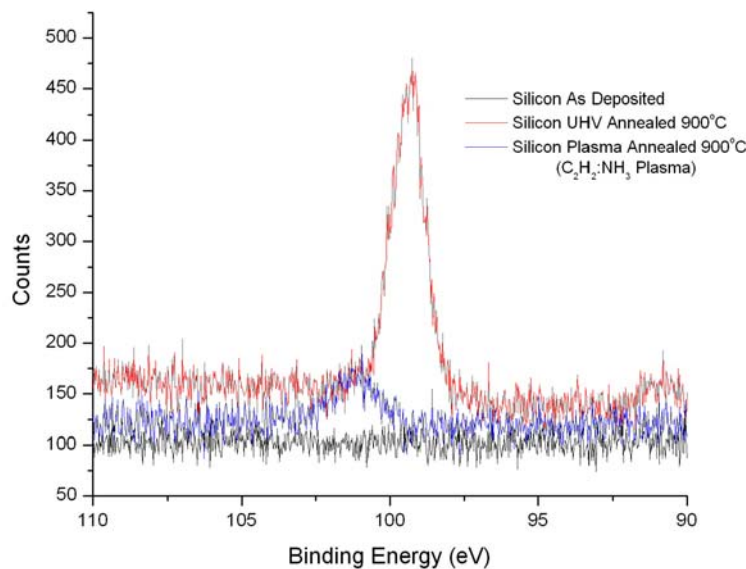


Figure 3.5. XPS ($Mg K\alpha$) spectra of Si content in as-deposited, plasma annealed, and UHV annealed TiN films.

A significant reduction in exposed Si for the plasma annealed TiN films is noted when comparing the XPS Si peak intensities in Fig. 3.5 for the UHV annealed and plasma annealed films. A shift in the nitrogen peak for the plasma annealed films indicated the formation of SiN. It is likely that the formation of the SiN was a result of exposed Si reacting with the nitrogen rich atmosphere produced in the plasma. Compositional analysis of the plasma annealed TiN film was not performed due to contamination of the film after exposure to atmosphere and secondary reactions taking place on the surface resulting in a non-homogeneous TiN cross sectional sample area.

3.4 Characterization of Annealed Fe Films on TiN Coated Si Substrates

In addition to characterization of the TiN films alone, it is important to investigate the influence of annealing on the catalyst and buffer system as a whole. Fe films annealed on the TiN buffers were investigated using AFM and photo electron emission microscopy (PEEM) to determine the structural transitions of the Fe and TiN films during annealing. A direct comparison between annealed Fe films on TiN and Si was also investigated using AFM.

3.4.1 AFM of Annealed Fe Films on TiN Coated Si Substrates

As stated in chapter 2, active Fe nanoparticles are essential for the catalytic growth of CNTs. To study the morphological changes of annealed Fe films supported on a TiN buffer layer, AFM was employed. The AFM image presented in Fig 3.6 show the resulting transition of an as-deposited 20 nm film of Fe on a TiN buffer annealed to 900 °C in UHV.

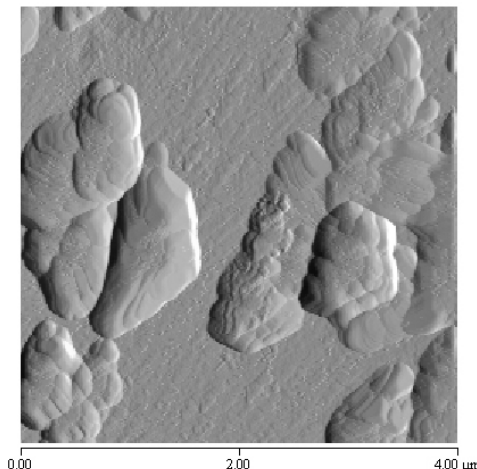


Figure 3.6. AFM error signal image of a 20 nm Fe film annealed on a 25 nm buffer layer of TiN deposited on a Si substrate. (Images acquired in contact mode using a Si tip).

The Fe films on TiN were found to form islands of various sizes, typically much larger than those capable of producing CNTs. The large island formation observed in the AFM images is attributed to coalescence and ripening during the annealing process. To verify this behavior, PEEM was employed to observe, in real time, the transitions of an Fe film as it was annealed from room temperature to 900 °C.

3.4.2 PEEM of Annealed Fe Films on TiN Coated Si Substrates

Under the various forms of microscopy, electron microscopy has proven to be a useful tool for the characterization of materials surfaces. The PEEM utilizes photo-emitted electrons from a materials surface to effectively generate real-time images of a sample's surface. The photo-excitation of electrons from the sample is achieved by illuminating a

material with light of a specific wavelength that has an energy large enough to overcome the photothreshold of the material. Commonly, ultra-violet light is used to elicit excitation but other forms of radiation such as X-rays have been used to effectively perform the same function.

The formation of images in the PEEM system is accomplished by collecting the photo-emitted electrons by a local field, $\sim 4 \text{ V}/\mu\text{m}$, generated between the sample and anode of the microscope. Once the photo-emitted electrons are emitted from the surface of the sample, they are accelerated towards the anode, maintaining their spatial distribution, and projected down the lens column containing a series of six electro-magnetic lenses used to form a magnified image of the sample surface. An image and schematic of the PEEM system is shown in Fig. 3.7.

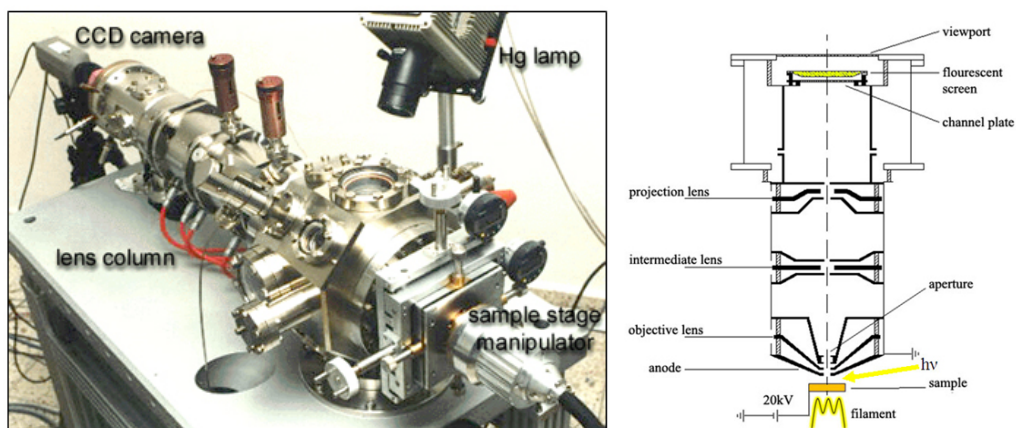


Figure 3.7. Image of a photo electron emission microscope and corresponding schematic showing the inner lens column and screen assembly.

The collected electrons leave the lens column and are projected onto a micro-channel plate that results in a gain of 5.6×10^7 at a test voltage of 2400 V. The resulting electrons are then projected on a phosphor coated conductive transparent screen to form images of the sample surface which are then captured using a CCD camera. Contrast in the images is achieved by

the variation in photo-yield across the film resulting from differences in elemental composition or topography on the surface. Additional contrast can result from materials that are sensitive to field or thermionic emission effects resulting from the applied accelerating voltage and/or heating of the sample.

PEEM investigation of the Fe films on the surface of a TiN coated Si substrate was carried out using a 244 nm UV laser corresponding to an energy of 5.08 eV. The transition of the 2-D Fe film into 3-D island structures was found to rapidly occur at a temperature of ~ 725 °C. Figure 3.8 shows a series of PEEM images captured during the transition phase.

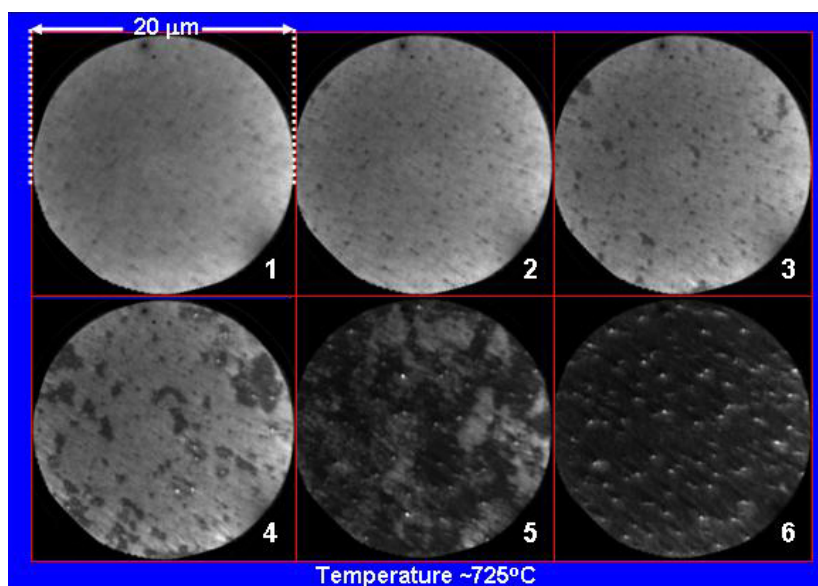


Figure 3.8. A series of PEEM images captured during the 2D layer to 3D island-like transition of an Fe film deposited on a TiN coated Si substrate.

Upon increased annealing times and temperatures, coalescence and ripening were observed. In the coalescence processes, the combination of two neighboring Fe islands resulted in the formation of a single larger island (See Fig. 3.9).

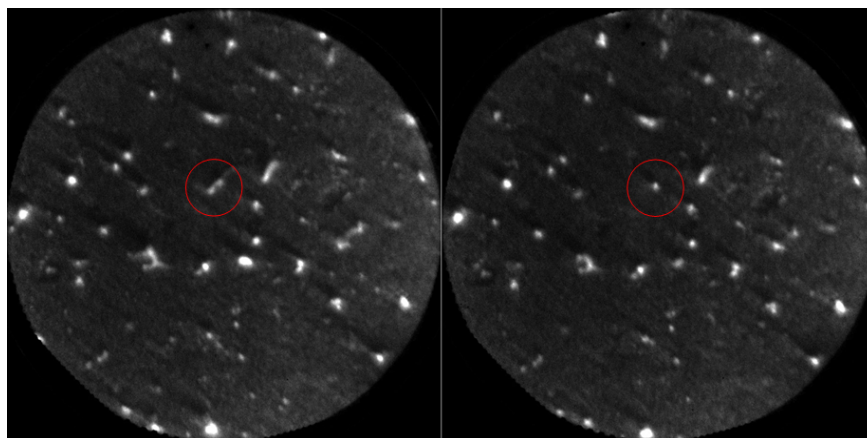


Figure 3.9. PEEM images of the annealed Fe films on a TiN coated Si substrate revealing island coalescence.

In addition to coalescence, ripening was also found to occur resulting in the growth of larger islands at the expense of smaller islands. The combination of ripening and coalescence explained the large island structures observed in the AFM images shown in Fig. 3.6.

3.4.3 AFM of Annealed Fe on TiN and Annealed Fe on Si

Fe films deposited on TiN and bare Si substrates were annealed in vacuum to 900 °C in order to obtain a direct comparison of the morphological changes exhibited by the catalyst during annealing on different surfaces. As a control, TiN was patterned over a Si substrate followed by the evaporation of a blanket Fe film 20 nm thick. The AFM images in Fig. 3.10 clearly show the Fe transition upon annealing the 20 nm thick films on TiN/Si (a) and bare Si (b) surfaces.

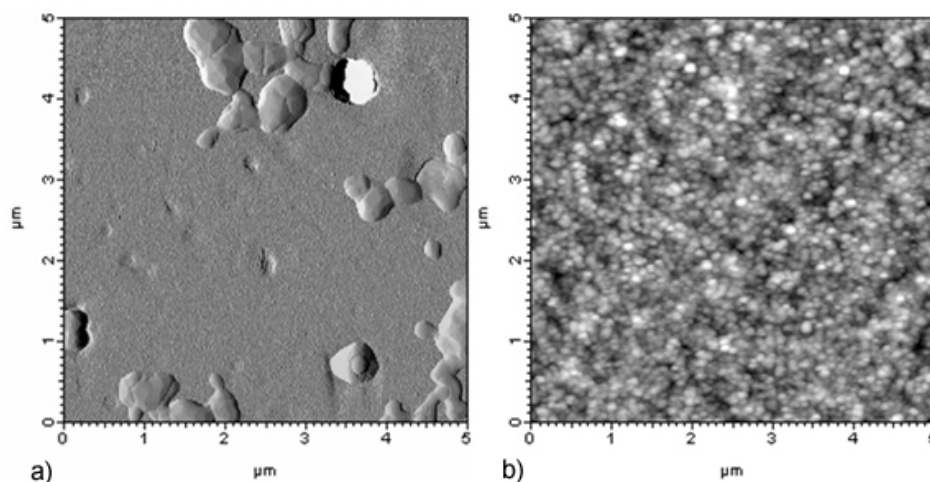


Figure 3.10. AFM error signal images revealing the transitions of 20 nm Fe films annealed to 900 °C on (a) TiN buffers and (b) Si substrates. (Images acquired in contact mode using SiN tips).

It should be noted that prior to TiN and Fe deposition, the native oxide from the Si surface was removed using an HF etch. Large island-like formations, as observed for Fe films annealed on TiN, were not observed to occur from Fe films annealed directly on Si. This indicated the formation of a silicide which has been reported to occur below 500 °C.¹²

Similar work by de los Arcos reported on the changes in chemical state of Fe films deposited on Si and various buffer layers after annealing to 840 °C.¹³ In this report he noted that a chemical change was detected in XPS spectra of Fe films annealed on TiO₂ and Al₂O₃ buffer layers, but Fe films annealed to 840 °C on TiN buffer layers remained un-reacted. This indicated that no reaction was taking place between the Fe and underlying TiN films and that TiN was acting as a sufficient barrier preventing the rapid formation of a silicide at the elevated temperatures. It was noted in a second report by de los Arcos that a small decrease in Fe signal was observed in the XPS spectra of the Fe films annealed on TiN buffer layers.⁹ He attributed this to diffusion of Fe through voids in the TiN film. He further noted that XPS of Fe films annealed directly on Si substrates revealed the formation of a silicide

which is known to hinder the catalytic activity for carbon nanotube growth. The effects of silicide formation on CNT growth will be presented in the following chapter.

3.5 Summary of TiN Deposition and Its Effectiveness as a Catalyst Support for CNT Growth and Field Emission Applications

XPS analysis of the PARE deposited TiN films revealed that they were of high quality and exhibited a N/Ti ratio of ~ 0.9 . The resistivity of the films was found to be $\sim 140 \mu\Omega\text{-cm}$ which was in good agreement with literature values of 100-200 $\mu\Omega\text{-cm}$ for thin films. AFM and XPS analysis of annealed TiN films on Si substrates revealed that up to temperatures of 500 °C, the films remained in a similar state to that of the as-deposited films. TiN films annealed to 900 °C in vacuum resulted in an agglomerated structure while 900 °C anneals of TiN films in a $\text{C}_2\text{H}_2/\text{NH}_3$ plasma environment resulted in a morphology similar to that of the as-deposited and 500 °C vacuum annealed films. This indicated that TiN films may possess a higher thermal stability when annealed in a $\text{C}_2\text{H}_2/\text{NH}_3$ plasma environment. In addition it was observed using XPS that the high temperature vacuum anneals resulted in a decrease of nitrogen content in the films.

AFM and PEEM analysis of Fe films annealed on TiN coated Si substrates revealed that the TiN layer acted as a sufficient buffer to prevent significant interaction of Fe with the underlying Si substrate. Coalescence and ripening were observed in the PEEM investigations which explained the large island formation observed in AFM images. Direct comparisons of Fe films annealed to 900 °C on uncoated and TiN coated Si substrates showed that the island like formation required for CNT growth did not occur on the uncoated Si substrates. This indicated the formation of a silicide which has been known to occur at temperatures of ~ 500 °C.

REFERENCES

- ¹ Jamd Valero, Y. Le Petitcorps, J. P. Manaud et al., *Journal of Vacuum Science & Technology A* **23** (3), 394 (2005).
- ² A. Sherman, *Journal of the Electrochemical Society* **137** (6), 1892 (1990).
- ³ G. I. Grigorov, K. G. Grigorov, M. Stoyanova et al., *Applied Physics a-Materials Science & Processing* **57** (2), 195 (1993).
- ⁴ H. C. Chen, B. H. Tseng, M. P. Hounq et al., *Thin Solid Films* **445** (1), 112 (2003).
- ⁵ V. D. Kalner and A. K. Verner, *Metal Science and Heat Treatment* **36** (3-4), 196 (1994).
- ⁶ John Moulder, William Stickle, Peter Sobol et al., *Handbook of X-ray Photoelectron Spectroscopy*. (Perkin-Elmer Corp., Eden Prairie, Minn, 1992).
- ⁷ I. Suni, M. Maenpaa, M. A. Nicolet et al., *Journal of the Electrochemical Society* **130** (5), 1215 (1983).
- ⁸ L. Gao, J. Gstottner, R. Emling et al., *Microelectronic Engineering* **76** (1-4), 76 (2004).
- ⁹ T. de los Arcos, F. Vonau, M. G. Garnier et al., *Applied Physics Letters* **80** (13), 2383 (2002).
- ¹⁰ M. Cantoro, S. Hofmann, S. Pisana et al., *Diamond and Related Materials* **15** (4-8), 1029 (2006).
- ¹¹ P. LeClair, G. P. Berera, and J. S. Moodera, *Thin Solid Films* **376** (1-2), 9 (2000).
- ¹² M. Kasaya, S. Yamauchi, M. Hirai et al., *Applied Surface Science* **75**, 110 (1994).
- ¹³ T. de los Arcos, M. G. Garnier, J. W. Seo et al., *Journal of Physical Chemistry B* **108** (23), 7728 (2004).

4. Synthesis and Characterization of Carbon Nanotubes Grown Using PECVD

Plasma enhanced chemical vapor deposition (PECVD) offers the advantage of nanotube growth capabilities over a larger temperature range and has been proven to be more effective in producing aligned CNT films than standard thermal CVD processes.¹ As in the case of supported catalytic growth of CNTs by thermal CVD methods, PECVD can enable the growth of CNTs of various diameters including single-walled carbon nanotube (SWCNT) growth. This chapter reports on the PECVD growth of vertically aligned CNTs and characterization of the films using scanning electron microscopy (SEM), transmission electron microscopy (TEM) and Raman spectroscopy.

4.1 Microwave PECVD System

In this study, vertically aligned carbon nanotube (VACNT) films were prepared using a microwave PECVD system. The PECVD system was assembled using a modified Applied Science and Technology, Inc. (ASTeX) system, model HPMS. The HPMS system consists of a vacuum chamber, an induction heater assembly with an Advanced Energy IPX-3750 power supply, an ASTeX S-1500 microwave power source, and a thermocouple/temperature controller to measure and regulate the temperature during processing. Vacuum is achieved using a rotary mechanical pump and the effective pumping speed is regulated using a throttle valve and automatic pressure controller coupled to a Baratron capacitance manometer. The system pressure can be set and maintained by balancing the gas inlet flow with the throttle valve position. Gas delivery is achieved using a MKS type 260 series modular control system consisting of four mass flow controllers and pneumatic valves supplying the reaction gasses into a mixing rail and ultimately to the system.

Microwave radiation is produced in the magnetron head that is coupled to a tunable waveguide output. The S-1500 supply is capable of delivering 1.5 kW of 2.45 GHz microwave power to the system through a quartz window attached to the vacuum chamber. Within the chamber, microwave energy couples to electrons ionizing the reaction gas species. Temperature control of the heater/sample stage is achieved through induction heating of a graphite susceptor using an induction heater supply. The induction heater allows for heating of the substrate up to ~ 900 °C. Substrate temperatures in excess of 1000 °C can be achieved through the use of the induction heating stage in combination with the heat generated from the microwave plasma. Cooling of the various system components including the vacuum chamber, heater induction coil and dummy load is required and is achieved using re-circulating purified cooling water connected to water flow indicators used as safety interlocks. A schematic of the HPMS system is shown in Fig. 4.1.

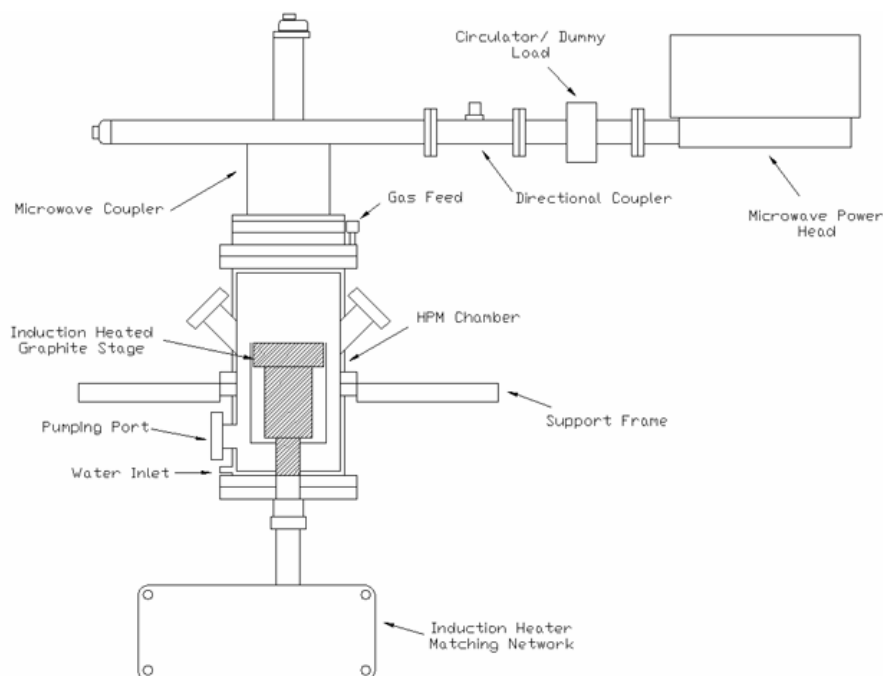


Figure 4.1 Schematic of the microwave plasma enhanced chemical vapor deposition system showing the main chamber with heater/sample stage and magnetron head with tunable waveguide.

4.2 PECVD GROWTH PROCESS

Sample preparation for the growth of CNTs is broken down into four stages: 1) substrate treatment; 2) buffer layer deposition; 3) catalyst deposition; and 4) sample pretreatment. The sample preparation involved the use of a UHV process and characterization tool composed of 13 growth and analysis systems interconnected by a 55 foot transfer line. Two of these UHV systems were employed for substrate and catalyst preparation, one system for surface characterization, and two systems for emission characterization. In addition to the UHV systems, PECVD and electron emission imaging systems were employed for CNT growth and emission characterization respectively. A schematic of the UHV process and characterization tool is shown in Fig. 4.2.

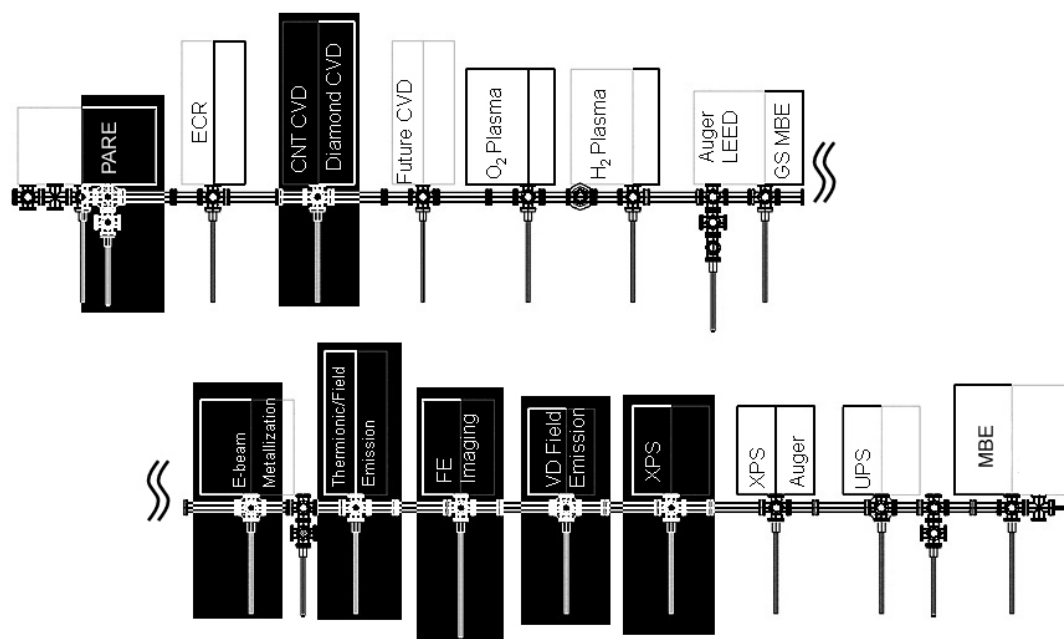


Figure 4.2. Schematic of UHV process and characterization tool (T-line) showing the systems used in this study (outlined in black).

4.2.1 Substrate Treatment

Carbon nanotube films were prepared on 25 mm diameter Si (110) n-type 0.49-0.67 Ω -cm substrates. Prior to loading the substrates into UHV, the native oxide was removed from the Si wafers using a 10:1 HF etch. After etching and removal of the native oxide, the substrates were transferred into UHV for buffer layer deposition.

4.2.2 TiN Buffer Layer Deposition

TiN buffer layers were deposited using plasma assisted reactive evaporation. Prior to deposition of the TiN buffer layers, the system was evacuated to a base pressure of approximately 5×10^{-9} torr and the substrate temperature was set to ~ 300 °C. Nitrogen was then fed through a SVT RF plasma source into the system using a leak valve. While introducing nitrogen into the system, 300 Watts of RF was delivered to the plasma source and a nitrogen plasma was initiated. The system pressure was set to 1×10^{-5} torr by adjusting the leak valve position.

After obtaining a stable nitrogen plasma, a solid Ti source was evaporated using an electron beam. The Ti evaporation rate was set to 0.5 Å/s as indicated by an oscillating quartz crystal monitor. The system pressure was maintained at 1×10^{-5} torr by adjusting the leak valve position. Once a stable evaporation rate was achieved, the sample shutter was opened and the selected thickness of TiN was deposited on the substrate surface.

4.2.3 Fe Catalyst Deposition

After deposition of the TiN buffer layers, the substrates were immediately transferred in UHV to a secondary electron beam evaporation system that was used to deposit the catalyst used for CNT growth. Fe films were deposited from a solid source (99.999% pure) at a rate of 1 Å/sec and at pressures typically $< 5 \times 10^{-10}$ torr with the substrate held at \sim RT.

4.2.4 Sample Pretreatment for CNT Growth

Prior to CNT deposition, the Fe containing substrates were loaded into the PECVD system and the growth chamber was evacuated to ~20 mTorr using a rotary mechanical pump. Following pump down, the substrates were heated to ~625 °C and pretreated in an C₂H₂:NH₃ atmosphere for ~2 min. The sample pretreatment was found to assist in the nucleation and formation of CNTs in the growth stage.

4.2.5 Parameters Used for CNT Growth

After pretreatment, hydrogen was flowed into the growth chamber for plasma initiation. Immediately after plasma ignition, the hydrogen gas source was shut off and simultaneously the C₂H₂ and NH₃ gasses were flowed into the chamber at typical rates of 25 and 55 sccm, respectively. C₂H₂ served as the carbon source while NH₃ was employed to suppress the formation of amorphous carbon deposits. Growth was carried out at a pressure of 28 torr, microwave power of 900 watts, and a substrate temperature of ~950 °C which was maintained through the combination of induction heating and heating due to the plasma. Growth times varied according to catalyst thickness and ranged from 1-30 minutes.

4.3 Characterization of PECVD Grown CNT Films

The resulting CNT films grown on TiN coated Si substrates were characterized by various methods for their structural composition as well as to obtain insight on their growth rate and growth mechanisms. Of specific interest were their alignment, structural composition, and whether or not they proceeded by base or tip growth mechanism.

4.3.1 SEM Analysis

SEM images of CNTs grown on the TiN buffer layers revealed that the CNTs were vertically aligned and the approximate growth rate was determined to be $\sim 5 \mu\text{m}/\text{min}$ for films grown from a 20 nm Fe catalyst film.

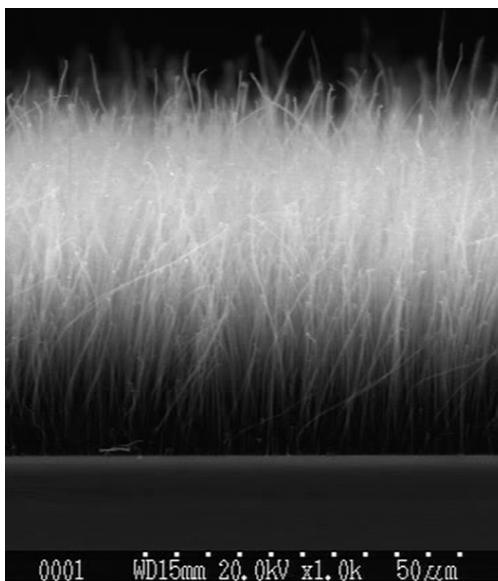


Figure 4.3. SEM image of an aligned CNT film grown for 10 minutes on a TiN coated Si substrate. A 20 nm Fe catalyst film thickness was used in the growth.

The effectiveness of TiN as a buffer layer, in preventing the interaction of Fe with Si, was directly observed for Fe films deposited on Si substrates containing patterned TiN layers. CNT growth was only observed to occur where the TiN buffer layer was present and the image in Fig. 4.4 shows the direct results when using the growth process described above.

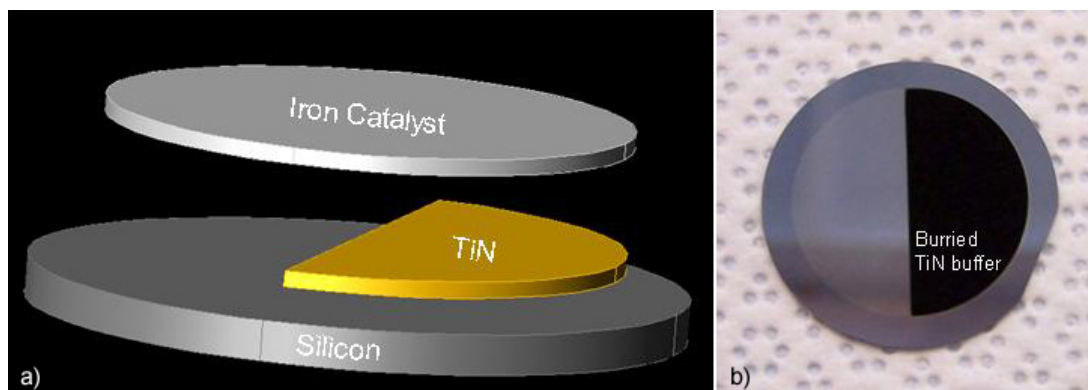


Figure 4.4. a) Schematic of the patterned TiN buffer and blanket Fe catalyst layers used to determine the influence of TiN on the growth of CNTs. The resulting CNT film is shown in (b).

The buried TiN layer effectively preserved the activity of the Fe catalyst film allowing CNT growth to occur on only half of the substrate. The lack of CNT growth on the unpatterned TiN region is attributed to the formation of an iron silicide which in turn transformed the Fe catalyst film into an inactive state.

4.3.2 TEM Analysis

TEM was employed to investigate the effects of catalyst film thickness on CNT growth as well as gain insight into the growth mechanism, tip or base, from which the various CNT films were produced. Fe films 5 nm and 20 nm thick were deposited on Si substrates containing 25 nm TiN buffer layers. The TiN films on both samples were deposited under the same conditions using plasma assisted reactive evaporation as described in chapter 3, and the 5 nm and 20 nm Fe films were deposited using electron beam evaporation. The substrates were then individually loaded into the PECVD reactor for CNT growth. Listed in table 4.1 and 4.2 are the pretreatment and growth parameters used for the preparation of the PECVD deposited CNT films.

Table 4.1. Pretreatment parameters used for CNT deposition on TiN coated Si substrates.

Pretreatment Parameters	Gas Flow (sccm)	Temperature (°C)	Time (min)
EB171 (20 nm Fe)	25:55 C ₂ H ₂ :NH ₃	600	2 min
EB172 (5 nm Fe)	25:55 C ₂ H ₂ :NH ₃	600	2 min

Table 4.2. Growth parameters used for CNT deposition on TiN coated Si substrates.

Growth Parameters	Gas Flow (sccm)	Microwave Power (Watts)	Temperature (°C)	Pressure (Torr)	Time (min)
EB171 (20 nm Fe)	25:55 C ₂ H ₂ :NH ₃	900	930	28	8
EB172 (5 nm Fe)	25:55 C ₂ H ₂ :NH ₃	900	940	28	3

After PECVD growth of the CNT films, small quantities of CNTs were scraped from the substrate surfaces and placed in glass vials containing acetone. The CNTs were then transferred from the vials to 300 mesh lacy carbon grids using a pipette. Prior to transferring the CNTs to the grid, the acetone/CNT solution was ultrasonically treated for ~5 min to separate and disperse the CNTs throughout the solution. The samples were then loaded into a JEOL 2010F high resolution TEM, and images of CNTs were captured for the two CNT specimens (See Fig. 4.5).

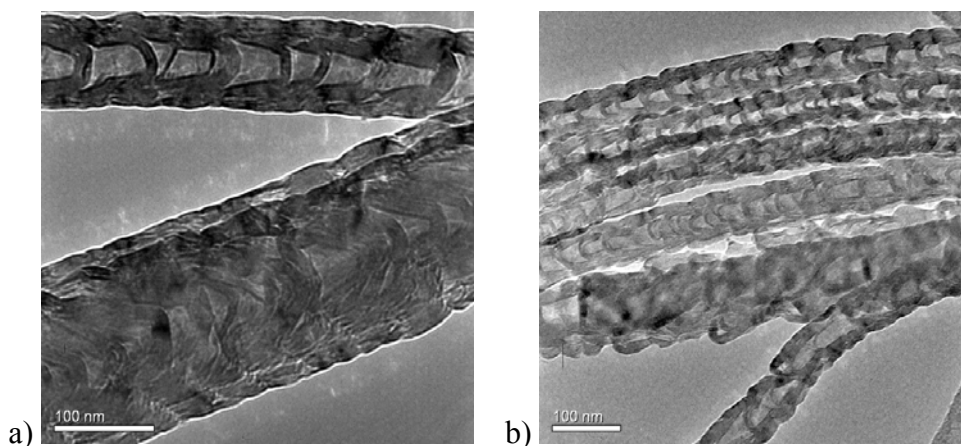


Figure 4.5. TEM image of a) large diameter CNTs grown from 20 nm thick catalysts and b) thinner diameter CNTs grown from a 5 nm thick catalyst. Growth from the 20 nm thick catalyst film resulted in a large distribution of CNT diameters while a tighter diameter distribution was obtained from the growth of the 5 nm thick catalyst film.

The sample grown from the 20 nm thick Fe catalyst layer contained a large distribution of CNT diameters as indicated in Fig. 4.5 (a) and by the numerous CNTs observed on the lacy carbon grid. The distribution was found to range from approximately 50 nm to 200 nm. The sample grown from the 5 nm thick Fe catalyst layer was found to have a smaller distribution of CNT diameters in the range of approximately 45 nm to 75 nm.

In the TEM characterization, a number of CNT endpoints were observed to terminate into a closed structure (See Fig. 4.6). This indicated that the endpoints or tips were not a result of CNT breakage.

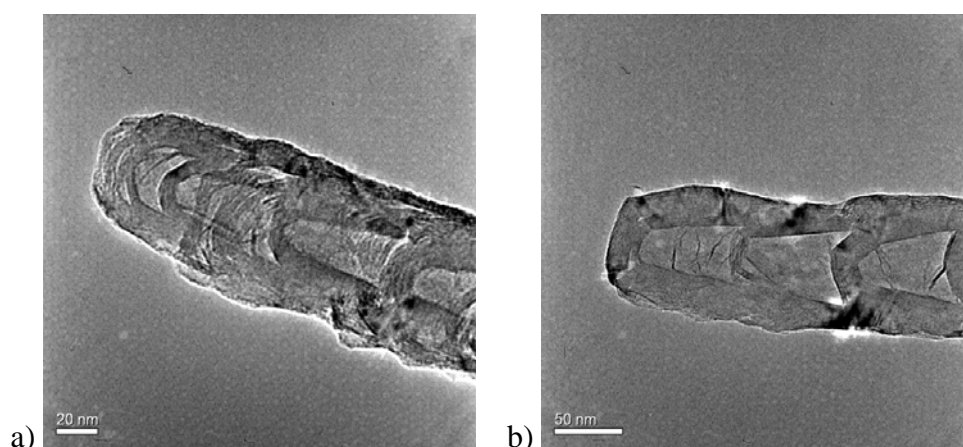


Figure 4.6. TEM images of CNT grown from (a) 5 nm Fe catalyst layer and (b) 20 nm Fe catalyst layer. Images of the tips revealed that no catalyst particles were observed to be encapsulated in the tips.

The images in Fig. 4.6 were captured slightly out of Scherzer focus in order to improve contrast in the internal structure of the CNTs. This assisted in determining whether or not a catalyst particle remained enclosed or on the tip of the CNT. No catalyst particles were observed to be on or enclosed in the tips indicating that the growth of the CNTs occurred predominantly through the base growth mechanism (Refer to Fig. 2.1). Numerous CNTs were observed to terminate into the closed structure while the other ends of the tubes resulted

in a structure that appeared to be due to breakage. This indicated that the catalyst particles most likely remained attached to the substrate during the CNT removal process, which gives further evidence that the growth occurred according to the base growth mechanism.

4.3.3 Raman Spectroscopy Analysis

Raman spectroscopy has extensively been used in the analysis of carbon based materials such as diamond and graphite. This fast non-destructive method has shown to be very useful in the characterization of CNTs. The characteristic bands in the Raman spectra of CNTs, located at $\sim 1350\text{ cm}^{-1}$ and $\sim 1580\text{ cm}^{-1}$, correspond to the D and G lines respectively. The G-band is characteristic of highly ordered graphite and corresponds to the in-plane vibration of two neighboring carbon atoms. The D band, commonly observed for pyrolytic graphite, is a symmetrical stretch which is forbidden in perfect graphite.² The appearance of the D band becomes more evident as disorder in the CNT increases. For CNTs, the D band has been attributed to disorder-induced features arising from defects in the curved structure of the nanotubes or nanotube ends. Additionally, the presence of carbon nanoparticles or diamond-like carbon layers have been found to give rise to the D peak observed in spectra obtained from CNT samples.³

The Raman spectra in Fig. 4.7 were obtained for CNTs grown from 20 nm and 5 nm thick Fe catalyst films. The spectra were obtained at room temperature using 514.4 nm excitation.

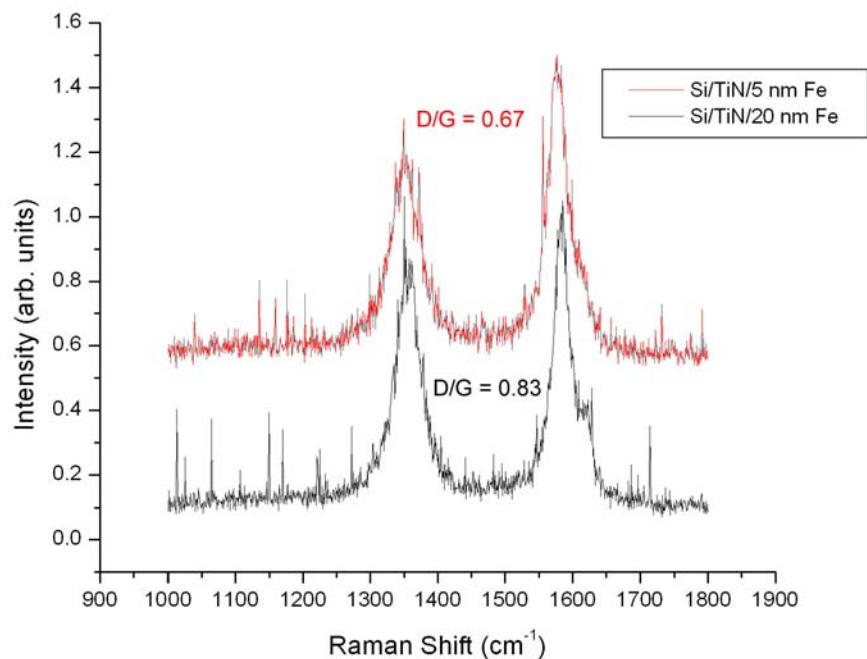


Figure 4.7. Raman spectra of PECVD CNT films grown from 5 nm and 20 nm catalyst layers.

The relative D/G peak ratio of the CNT films was found to be 0.67 and 0.83 for the 5 nm and 20 nm Fe catalyst samples respectively which is typical of PECVD grown multi-walled CNTs.^{4,5} The higher disorder of the CNT film grown using a 20 nm Fe catalyst may be attributed to the larger diameter CNTs possessing >50 walls as observed in TEM images.

4.4 Summary of PECVD Growth of CNTs and Characterization

It was directly observed that TiN buffer layers assisted in PECVD CNT growth on Si substrates when compared to uncoated Si substrates. SEM images of the CNT films revealed that they were vertically-aligned and a growth rate of $\sim 5 \mu\text{m}/\text{min}$ was achieved using 20 nm thick Fe catalyst films. TEM images revealed that CNT films grown from thick 20 nm Fe catalyst layers contained a large distribution of CNT diameters ranging from approximately 50 nm to 200 nm. 5 nm Fe catalyst layers produced CNT films with a diameter distribution of approximately 45 nm to 75 nm. This indicated that smaller diameter CNTs with a smaller

distribution could be achieved by utilizing thinner Fe catalyst layers. This effect was similarly observed in the reported work mentioned in chapter 2 of CNT growth on SiO₂ by Wang et al. Raman spectroscopy revealed that the CNT films displayed a component attributed to disorder in the CNT or to the presence of diamond-like carbon particles or layers. When compared to the CNT film grown from the 5 nm thick catalyst layer, the disordered component was observed to be higher for the larger diameter CNT film grown from the 20 nm thick catalyst layer.

REFERENCES

- ¹ C. Bower, W. Zhu, S. H. Jin et al., *Applied Physics Letters* **77** (6), 830 (2000).
- ² J. D. Harris, R. P. Raffaele, T. Gennett et al., *Materials Science and Engineering B-Solid State Materials for Advanced Technology* **116** (3), 369 (2005).
- ³ H. Hiura, T. W. Ebbesen, K. Tanigaki et al., *Chemical Physics Letters* **202** (6), 509 (1993).
- ⁴ M. Chhowalla, K. B. K. Teo, C. Ducati et al., *Journal of Applied Physics* **90** (10), 5308 (2001).
- ⁵ C. H. Lin, S. H. Lee, C. M. Hsu et al., *Diamond and Related Materials* **13** (11-12), 2147 (2004).

5. Field Emission Theory and Characterization

The first and second sections of this chapter outline the development and basic principles of field emission theory. The unique properties of CNTs that enable their field emission capabilities are addressed, and the later sections of the chapter focus on the field emission characterization from CNT films grown on TiN buffer layers.

5.1 Field Emission Theory

Field emission is a quantum mechanical phenomenon defined as the emission of electrons from the surface of a condensed phase into another phase under the application of high electric fields.¹ Although field emission can take place at numerous interfaces, for simplicity we will restrict this discussion to the field emission of electrons from a metal into vacuum. When considering electron emission process such as thermionic emission and photoemission, electrons gain sufficient energy to overcome the potential barrier at a metal-vacuum interface allowing electrons to escape from the metal surface into vacuum. Field emission, on the other hand, involves the emission of electrons from the metal surface into vacuum by tunneling through a potential barrier rather than overcoming it. The likelihood that electron tunneling will occur depends on the shape of the potential barrier which is determined by the applied electric field, the work function of the metal, the image force on an electron, and any factors that influence the surface from which the electrons will be emitted.

Significant contributions to the development of field emission theory began with the observed phenomenon by R. W. Wood in 1897.² Further experimental and theoretical contributions by Schottkey,³ Millikan,⁴ Richardson,⁵ and Debye,⁶ to name a few, led to a quantum-mechanical based model of field emission developed by Fowler and Nordheim in 1928.⁷ The free-electron theory of field emission predicts that at low temperatures, the

relevant free electrons are contained within a small energy interval around the Fermi level of the metal. These electrons, under low temperature conditions and the application of an electric field, are capable of tunneling through a retarded surface potential barrier as shown in Fig. 5.1.

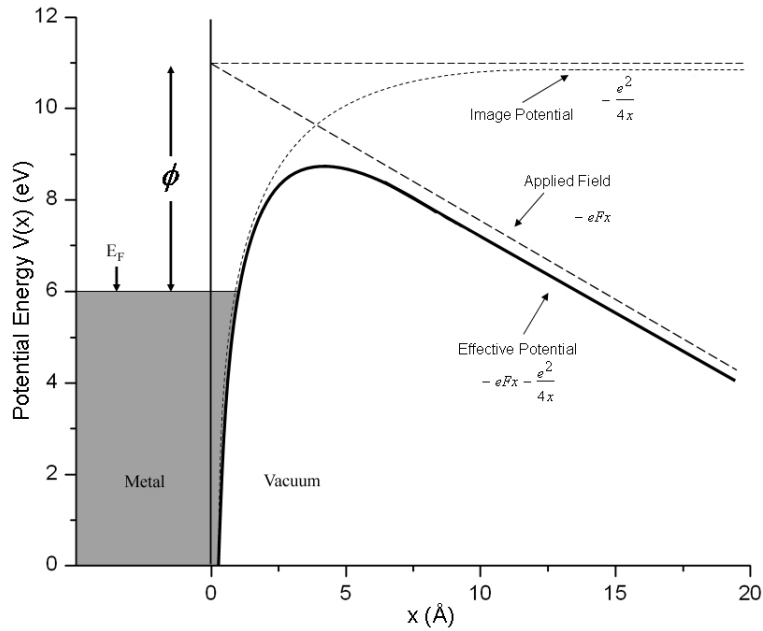


Figure 5.1. The surface potential barrier seen by an electron. The metal has a work function of 4.5 eV.

The Fowler-Nordheim (F-N) theory is based on the assumption that the metal surface is planar and that the metal obeys the free electron model with Fermi-Dirac statistics. In addition, it is assumed that the potential within the metal is constant and that the system is at a temperature of $T=0$ K. At a temperature of 0 K the emission current density is given by the equation

$$j = e \int_0^{\infty} n(E_x) D(E_x, F) dE_x, \quad (5.1)$$

where e is the electron charge, $n(E_x)$, referred to as the supply function or the number of electrons per second having energies between E_x and $E_x + dE_x$ incident on 1 cm^2 of the barrier surface from within the metal,

$$E_x = \frac{Px^2}{2m} \quad (5.2)$$

is the normal kinetic energy in the tunneling direction, $D(E_x, F)$ is the transmission coefficient, m is the free electron rest mass, and F is the applied electric field.

The Wentzel-Kramers-Brillouin (WKB) approximation has been used to calculate the barrier transparency for the one dimensional case.¹ Here $D(E, F)$ is the probability that an electron traveling to the right will not be turned back at the barrier but proceed through it.

The potential at a planar metal surface has the form

$$V(x) = -eFx - \frac{e^2}{4x} \quad (5.3)$$

where the magnitude of the image force is equal to $e^2/4x$ and points in the direction towards the metal surface.

Within the free electron model and the WKB approximation, the planar potential model of a tip results in the well-known Fowler-Nordheim equation⁸

$$J(F) = A' F^2 \exp\left[\frac{-B' \phi^{1.5}}{F}\right] \quad (5.4)$$

where

$$A' \equiv e^3 / \left[8\pi\phi^2 \left(\frac{(e^3 F)^{1/2}}{\phi} \right) \right] \quad (5.5)$$

$$B^1 \equiv \frac{8\pi}{6e} (2m)^{1/2} v \left(\frac{(e^3 F)^{1/2}}{\phi} \right) \quad (5.6)$$

The functions $t(y)$ and $v(y)$, where $y=y(F)$ are elliptic integrals whose values have been tabulated.¹ Here $v(y)$ effectively describes the image force lowering of the potential barrier. Evaluating $J(F)$ and inserting the appropriate approximations, the F-N equation reduces to

$$J = 1.54 \times 10^{-6} \frac{F^2}{\phi} \exp\left(\frac{10.4}{\sqrt{\phi}}\right) \exp\left(-6.87 \times 10^7 \frac{\phi^{1.5}}{F}\right) \quad (5.7)$$

where the current density J is in A/cm^2 , F is the applied electric field in V/cm , and ϕ is the work function of the material in eV .⁹

5.2 Effects of Morphology on Field Emission Properties

The derivation of the F-N equation is based on the assumption that the emitting surface is planar. Assuming a flat surface, fields on the order of $3\text{-}7 \times 10^3 \text{ V}/\mu\text{m}$ are necessary for appreciable field emission.¹⁰ Realistically, these values are much higher than desirable and experimentally difficult to achieve. Experimentally, it was observed that values of this order can be readily achieved with the use of field enhancement phenomena which originate from sharp tip structures (See Fig. 5.2).

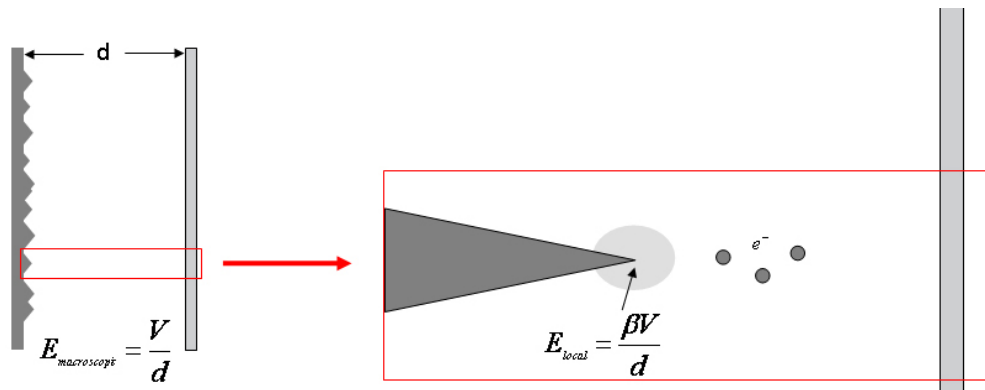


Figure 5.2. Schematic diagram of an emitter tip which results in the local field enhancement effect enabling the tunneling of electrons through the potential barrier.¹⁰

A rough surface will have features that lead to the distortion of the applied field. Sharp structures, historically etched Mo tips, have been found to magnify the macroscopic field up to 30+ times.¹¹ To account for the magnification of the field, a proportionality constant β was introduced. In many instances the value of β is approximated using the parameters of tip height and tip radius. The common expression derived from sphere-on-cone and sphere-on-cylinder models is

$$\beta = 2 + \frac{h}{r} \quad (5.8)$$

where h is the height of the protrusion in reference to a conducting base plane, and r is the radius of curvature of the tip.¹² This general expression typically holds where the h/r ratio is greater than or equal to 5.

Protrusions exhibiting needle-like geometry are commonly modeled as a sphere on a cylindrical or conical shank. The approximation of β in this case, where no conduction plane is nearby, only depends on the sharpness or effectively the radius of curvature at the tip.

Under this condition the field enhancement is approximated by

$$\beta = \frac{F_{\text{microscopic}}}{F_{\text{macroscopic}}} = \frac{1}{kr} \quad (5.9)$$

where r is the radius of curvature and k typically ranges from 3 to 5.¹³

When considering the electric field between two flat parallel plates the magnitude of the field, F is determined by the applied voltage divided by the separation distance.

$$F = \frac{V}{d} \quad (5.10)$$

In the cases where field enhancement is applicable, the effective field can be approximated using

$$F = \frac{\beta V}{d} \quad (5.11)$$

where β is local magnification of the electric field due to field enhancement.

Substituting the field enhancement correction for the applied field into the F-N equation yields

$$I = A \cdot 1.54 \times 10^{-6} \frac{\beta^2 F^2}{\phi} \exp\left(\frac{10.4}{\sqrt{\phi}}\right) \exp\left(-6.87 \times 10^7 \frac{\phi^{1.5}}{\beta F}\right) \quad (5.12)$$

The current I can be taken as the emission current density J divided by the area A .

It should be noted that in a plot of the $\ln(J/F^2)$ vs $1/F$, also known as the F-N plot, the corresponding curve yields a straight line which has been experimentally observed in specific regions of applied fields. The F-N plot is a useful tool which is often used to characterize the field emission behavior of a material and in certain cases can allow an estimate of material properties such as work function and field enhancement factors as well as give an approximation of an emitter's potential performance.

5.3 Field Emission Characterization by the Approach Curve Method

An important technique to characterize field emission from a material is to measure the electron emission current density (J) versus an applied field (F). Normally this is done by assembling the cathode and anode in a parallel plate configuration using an insulating spacer of a known distance. An alternate method of characterization is to use the approach curve method where a movable anode, commonly a truncated cone, is assembled normal to the cathode surface. This method is typically useful in circumstances when it is difficult to

accurately position the anode and cathode a known distance from each other. The approach curve method was employed in this case to enable UHV processing and field emission characterization of CNT films grown on the TiN buffer layers.

5.3.1 Variable Distance Field Emission System

The basic components of the variable distance field emission system (VDFES) used in this study are a vacuum chamber, sample stage, movable anode and a source measure unit (SMU). An additional feature of the VDFES is that it is interconnected to the UHV process and characterization tool (Refer to Fig. 4.2) which allows the study of in-situ treatments and their effect on the field emission properties of a sample. The vacuum in the VDFE chamber is maintained using a turbo molecular pump which provides typical operation pressures of $\sim 5 \times 10^{-9}$ torr. The sample (cathode) is mounted to a specimen holder which remains fixed in the VDFES when loaded. The anode is mounted to a movable stage allowing linear translation normal to the sample surface. Linear motion of the anode is achieved through a vacuum stepper motor and can be precisely controlled to move in step sizes of 55 nm toward or away from the cathode surface.

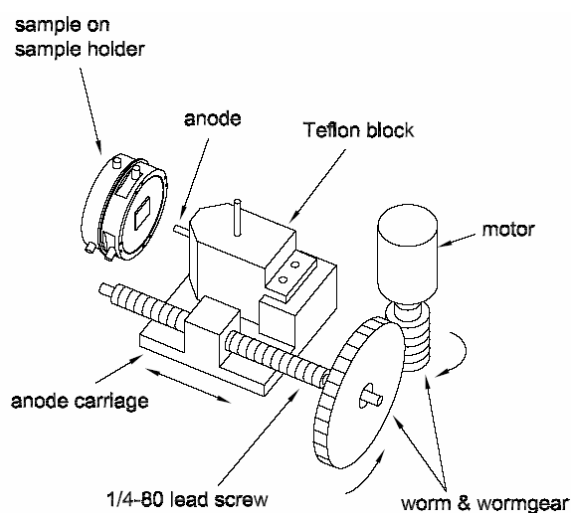


Figure 5.3. Schematic of the setup for the variable distance field emission system showing the mechanism of the anode stepper.

The anode used in these studies was a 2 mm diameter Mo rod that was polished to a high radius of curvature, typically >5 mm. Current-voltage measurements were obtained using a Keithley 237 SMU interfaced to a computer for data acquisition.

Although an accurate anode-cathode spacing is difficult to measure in the VDFES, accurate relative distances could easily be obtained using the anode stepper. Since only a relative anode-cathode spacing is known, precautions were taken to prevent anode and cathode contact which could damage the emitter or render the anode surface leading to uncharacteristic I-V measurements. In order to protect the sample/anode from possible arcing or contact, a compliance value, typically 1 nA, was set to limit the extracted emission current. The voltage required to reach the compliance current was a good indication of how close the emitter was to the anode probe.

Initial setup for I-V measurements consisted of loading the emitter into the VDFES ensuring that proper electrical contact was formed between the sample, sample holder, and sample stage. This was accomplished with the aid of stainless steel springs that compressed the sample holder to the stage preventing any shifting or rotation of the sample during I-V measurements. Starting at a small gap location, usually set by visual inspection, an I-V sweep was initiated to determine if the emission current was within the detection limits of the source measure unit (~ 1 pA). If the compliance current was reached within the voltage range of the SMU (0-1100V), the cathode-anode distance was increased and if the compliance value was not reached the cathode-anode distance was decreased. This process was repeated until the compliance current was obtained at values near 1100 V, the maximum voltage of the SMU. This became the starting and reference point for the remaining measurements. At the reference point an I-V sweep was initiated ensuring that the compliance value of 1 nA was

reached within the voltage range of the SMU. Once the I-V sweep was completed the anode was moved closer to the cathode, typically in 55 μm increments, using the stepper. After translation of the anode, the stepper value was recorded and a second I-V sweep was initiated. This process was repeated until the compliance current was reached at low voltage values, typically ~ 300 V. At this point, the potential for arcing and damage is high due to the small cathode-anode spacing so the measurements were terminated.

5.3.2 Threshold Field Determination

Figure 5.4 shows a series of IV curves obtained at 55 μm spacing intervals.

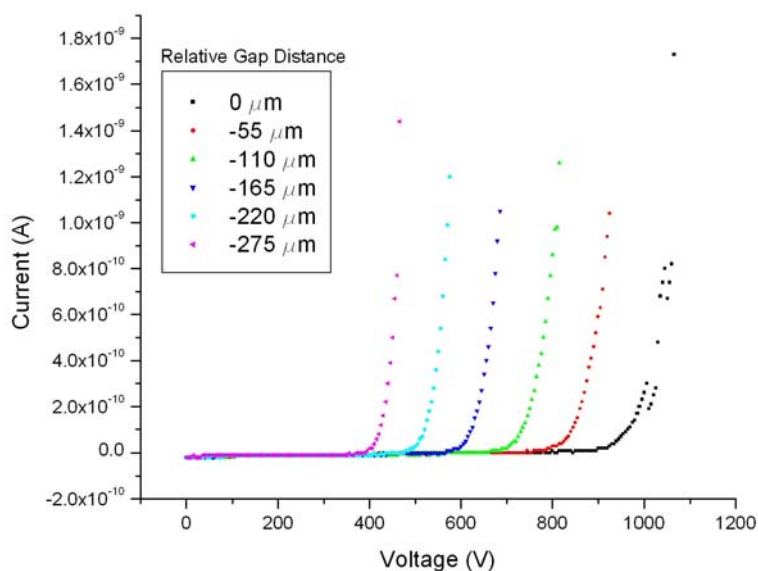


Figure 5.4. Current vs. voltage sweeps at various 55 μm step sizes for an as loaded CNT film grown on a TiN coated Si substrate. Emission was found to be unstable leading to large jumps in current and variations in the I-V upsweep and downsweep.

Under as-loaded conditions, the I-V data obtained for the CNT films showed that the emission was quite unstable during single forward and return sweeps as well as from one anode spacing to another. The instability in the emission was attributed to adsorbates which are common to CNT films and have been shown to influence the field emission behavior of

the films. In order to remove the adsorbates from the surface of the film, the sample was transferred in UHV from the VDFES to an alternate system where it was annealed to ~ 900 °C under UHV conditions. After the annealing stage, the sample was immediately transferred back to the VDFES for a second series of I-V sweeps. The resulting data revealed that the emission from the sample was much more stable over the entire sweep series.

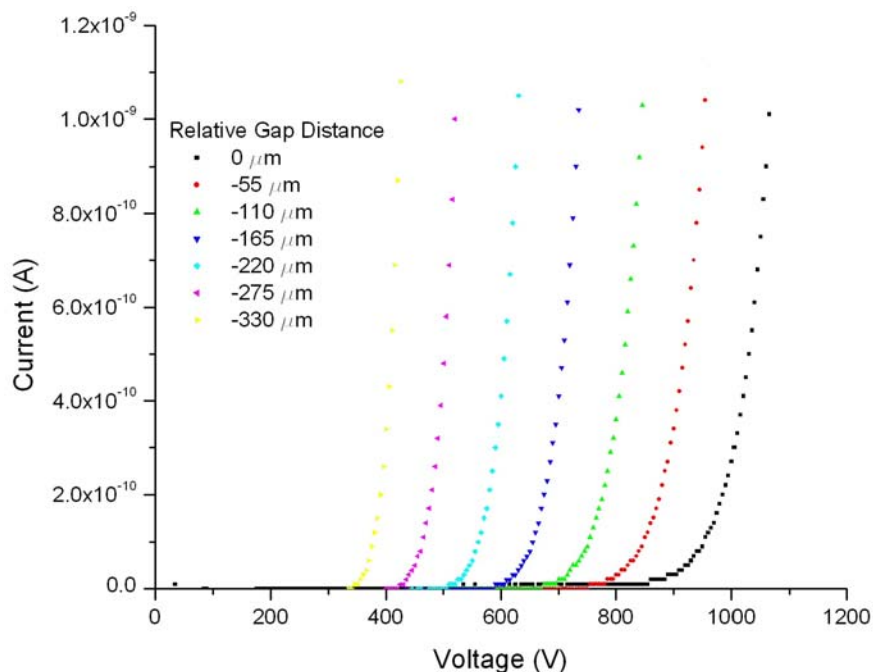


Figure 5.5. Current vs. voltage sweeps at various 55 μm step sizes for a UHV annealed CNT film. Emission was found to be much more stable when compared to the as loaded sample.

When using the approach curve method, an absolute separation distance is unknown so it is useful to generate a voltage vs. relative distance curve from which an average threshold field value can be obtained. In Fig. 5.6, the voltage required to reach the compliance current of 1 nA was plotted versus the relative step distance of 55 μm in the plot of Fig. 5.5.

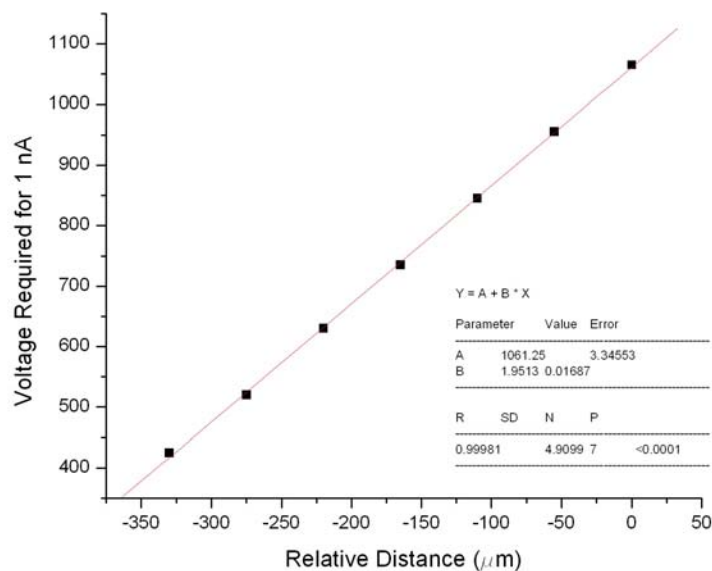


Figure 5.6. Plot of the voltage required for extraction of 1 nA of current vs. the relative distance for a CNT film grown on a TiN coated Si substrate.

The corresponding plot is a straight line in which the slope of the line represents the average threshold field required to obtain a current of 1 nA from the film. In this case a value of 1.95 V/ μm was determined as the threshold field required for the extraction of 1 nA from the film.

5.3.3 Field Enhancement Factor Determination

Further data analysis of the CNT film consisted of plotting the $\ln(I/V^2)$ vs $1/V$ to obtain F-N plots of the I-V data. The slope of the F-N plots can be obtained by a linear fit of the data for the number of sweeps taken at each step value.

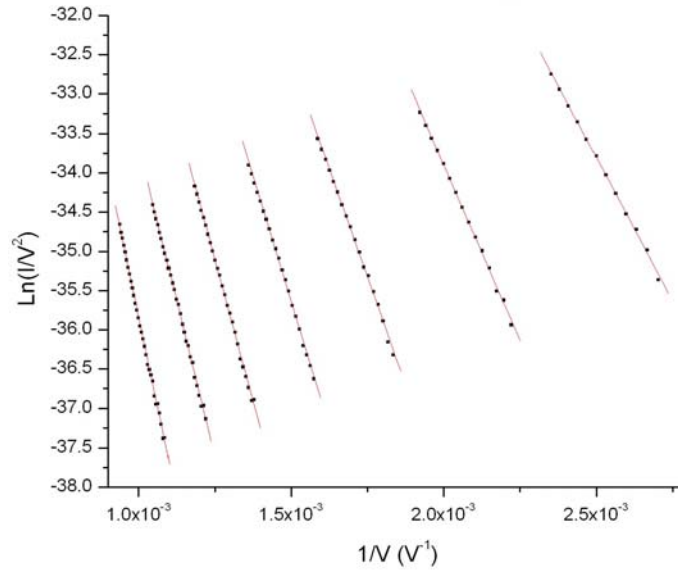


Figure 5.7. F-N plots and corresponding linear fits of the I-V data presented in Fig 5.5.

A plot of the F-N slope vs. relative distance results in a straight line whose slope can be used to estimate specific parameters related to the CNT emitter.

The general form of the F-N equation can be written as

$$I = aV^2 \exp(-b/V) \quad (5.13)$$

where

$$a = 1.54 \times 10^{-6} \frac{\beta^2}{d^2 \phi} \exp\left(\frac{10.4}{\sqrt{\phi}}\right) \quad (5.14)$$

$$b = -6.87 \times 10^7 \frac{d\phi^{1.5}}{\beta} \quad (5.15)$$

Here b will be the slope of the line in the F-N plot of the data and can be used to extract information about the average field enhancement factor or materials effective work function.

A plot of the slope values, obtained for the fits in Fig. 5.7, vs. relative distance will give a slope, b, equal to

$$b = -6870 \frac{\Delta d \phi^{3/2}}{\beta} \quad (5.16)$$

when the proper conversion factors are inserted.

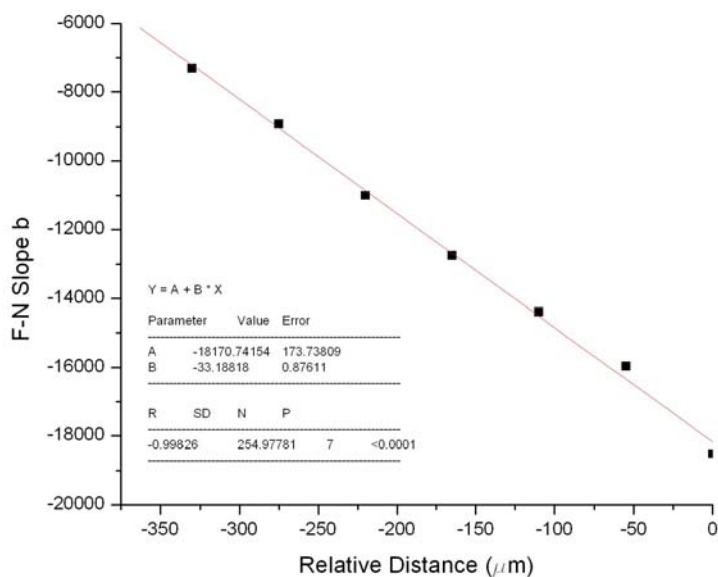


Figure 5.8. A plot of the F-N slopes vs. relative distance which can be used to approximate the field enhancement factor of a CNT film (obtained from the data of Fig. 5.7).

With the known slope, an approximation of the films average field enhancement factor can be determined with knowledge of the materials work function and vice the versa. From the data presented in Fig. 5.8, a field enhancement factor of ~ 2300 was estimated when a work function of 5 eV, common for nanotubes, was used.

When considering electron emission measurements using a small anode probe the potential for error is quite high when attempting to obtain quantitative data. Effects such as adsorbates, anode irregularities, or strong localized emission sites can easily result in misleading characterization. This may explain the wide variation in reported data on calculated β values as well as the maximum emission current densities achieved from CNT

films.¹⁴ The discussion of adsorbates and emission site density will be addressed in the following sections.

5.4 Emission Current Measurements In the Parallel Plate Field Emission System

High current measurements were performed over large (3.24 cm^2) emission areas in the parallel plate field emission system (PPFES) to gain insight on the emission characteristics of the CNT films as a whole. In this section the PPFES will be described and the emission properties of the CNT films deposited on TiN buffers will be discussed.

5.4.1 Parallel Plate Field Emission System

To further investigate the emissive properties of the CNT films, I-V data was gathered in a secondary electrical characterization system utilizing a parallel plate configuration. The system pressure was maintained using a turbo molecular pump which was capable of achieving a base pressure on the order of 2×10^{-7} torr. An upgrade to the pump eventually resulted in an achievable base pressure of 2×10^{-8} torr. A schematic of the parallel plate anode-spacer-cathode stage is shown in Fig. 5.9.

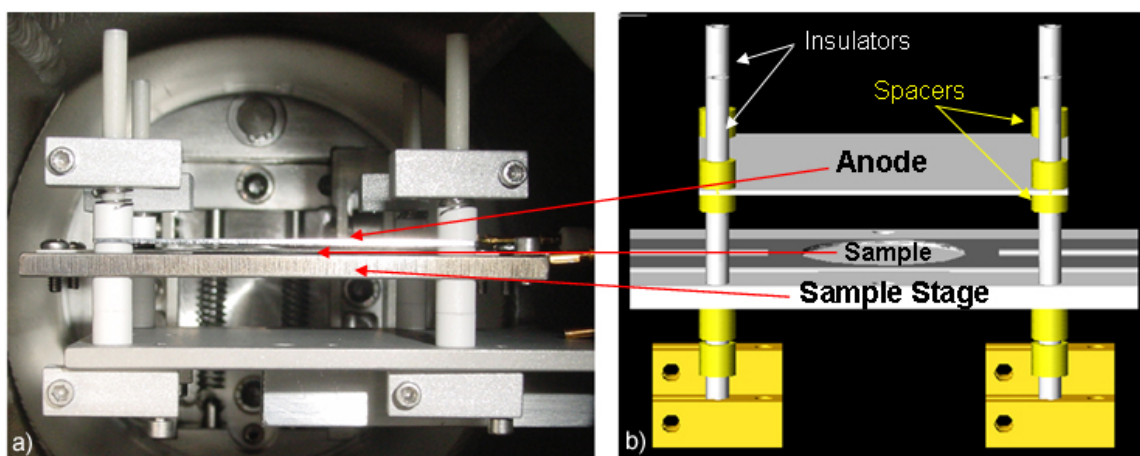


Figure 5.9. a) Image and b) schematic of the parallel plate field emission stage.

The stainless steel anode and Mo sample stage were electrically isolated and held in place using alumina rods. The sample-anode spacing was determined using a single or

combination of alumina spacers 0.025", 0.05" or 0.1" thick. This allowed for accurate calculation of the macroscopic applied field values (voltage/spacing). The flexible stage design allowed the loading of various sample sizes and shapes enabling topside and backside contact as well as the capability to easily change the anode plate to an emission imaging screen.

This field emission system is capable of measuring the overall emissive behavior of films up to 1" in diameter as apposed to the VDFES which only sampled an area corresponding to the 2mm diameter anode. In addition, this system is capable of applying voltages up to 5 kV and measuring current levels up to 5 mA. The high voltage source measure unit used was a Stanford Research PS350 capable of delivering up to 25 watts. The power supply was connected to a personal computer through a general purpose interface bus (GPIB) to allow automated voltage application and data acquisition. A schematic of the system is shown in Fig. 5.10.

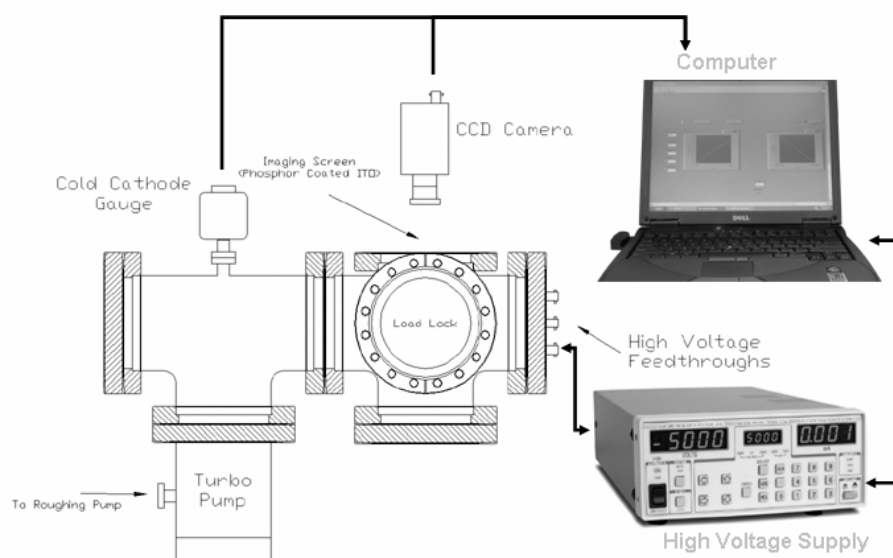


Figure 5.10. Schematic of the PPFES showing the power supply and computer interface used to collect field emission data.

A program was written using Labview to control the voltage sweep and simultaneously record the measured current values. This was achieved by simulating a triangular wave of a certain frequency and amplitude that would correspond to the applied voltage.

5.4.2 PPFES Measurements and Comments on Adsorbate Effects

Data acquisition typically consisted of a number of voltage sweeps within the full limits of the supply (0-5 kV) or until a safe current limit of ~ 4.5 mA was achieved. The data shown in Fig. 5.11 is a typical current vs. voltage curve obtained for the CNT films grown on TiN coated Si substrates.

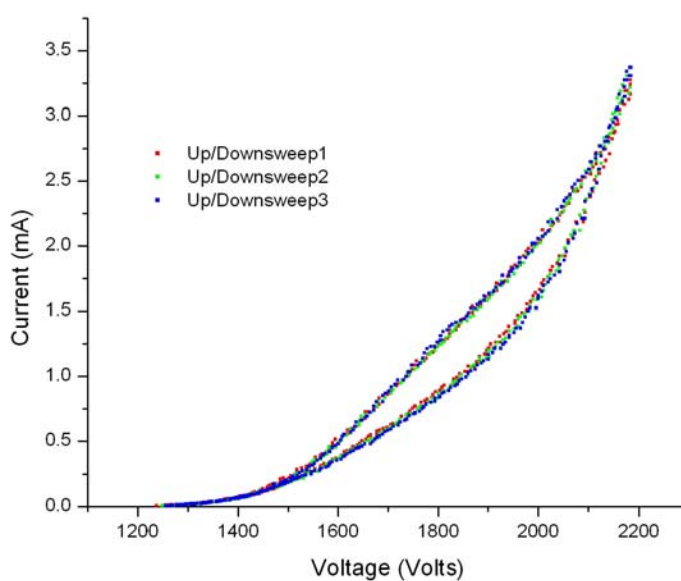


Figure 5.11. Current vs. voltage plots, for three up/down sweeps, obtained for a CNT film measured in the PPFES.

With the knowledge of the anode-cathode spacing and sample area, a plot of the current density vs. applied field can be made. In most cases the actual emission area is much less than the sample surface area because the emission originates from individual CNTs. This will lead to much higher current densities when considering only a fraction of the sample is emitting, but in general and for application purposes it is useful to know the

emission behavior of the film as a whole. Details of the emission site density will be further discussed in section 5.1.

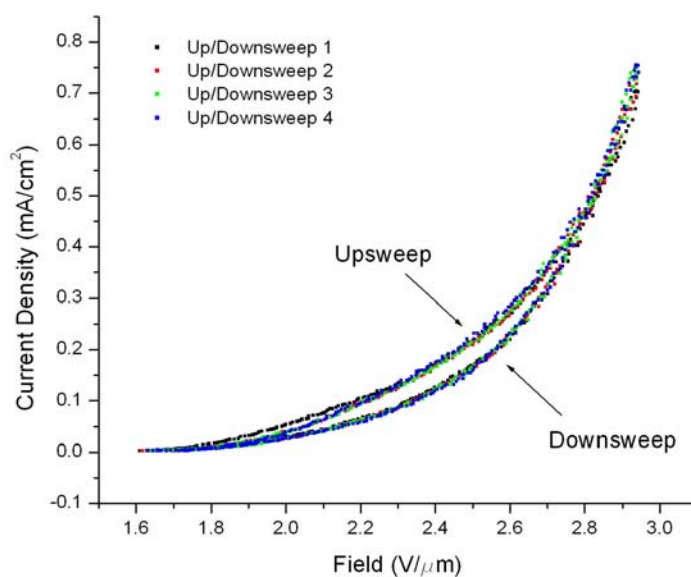


Figure 5.12. Current density vs. applied field plots for a CNT film measured in the PPFES.

Upon inspection of the I vs. V and J vs. F plots, hysteresis was observed in the forward/return or upsweep/downsweep data and remained consistent for multiple sweeps. This behavior was characteristic of nearly every film measured in the system. Upon changing the frequency of the supplied voltage sweep and corresponding data acquisition little to no observed change occurred in the hysteresis behavior. This ruled out the possibility of time lag occurring between the supply and GPIB interface with the computer. A more plausible explanation for the hysteresis behavior is the absorption and removal of adsorbates from the CNT films. On the upsweep, the adsorbates are effectively removed in the high current regime as a result of Joule heating of the emitter. The removal of adsorbates, known to enhance or hinder emission depending on type, results in less overall emission from the film. On the downsweep, the adsorbates return to the surface in the low current regime restoring the initial behavior again on the upsweep. To test this theory, a series of isolated

sweeps were run maintaining the emitted current in the low, middle and high emission regimes.

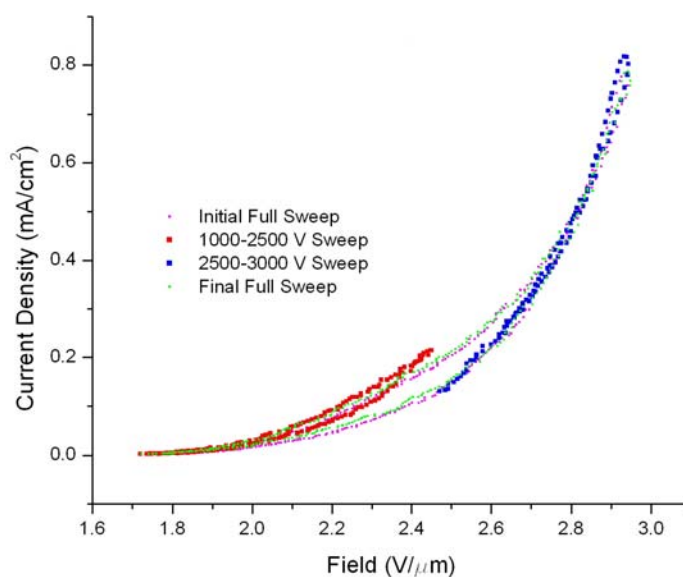


Figure 5.13. Current density vs. field plots of a CNT film showing adsorbate effects on the emission behavior.

As is evidenced in Fig. 5.13, hysteresis behavior was observed for the sweeps allowed to return to low emission levels. The lower current sweep (red) resulted in higher emission behavior when compared to the full sweep (green & magenta) due to the inadequate removal of adsorbates. Preventing the emission to return back to low current levels by isolating the sweeps in the high emission regime eventually resulted in the removal of the hysteresis behavior. The resulting curves in the high current regime closely resembled the downsweep data obtained for the typical full sweeps. This was convincing evidence indicating that adsorbates were the most likely cause of the hysteresis behavior observed in the field emission data.

A Fowler-Nordheim plot of the data represented in Fig. 5.14 contains three distinct emission regimes, each fairly linear in nature.

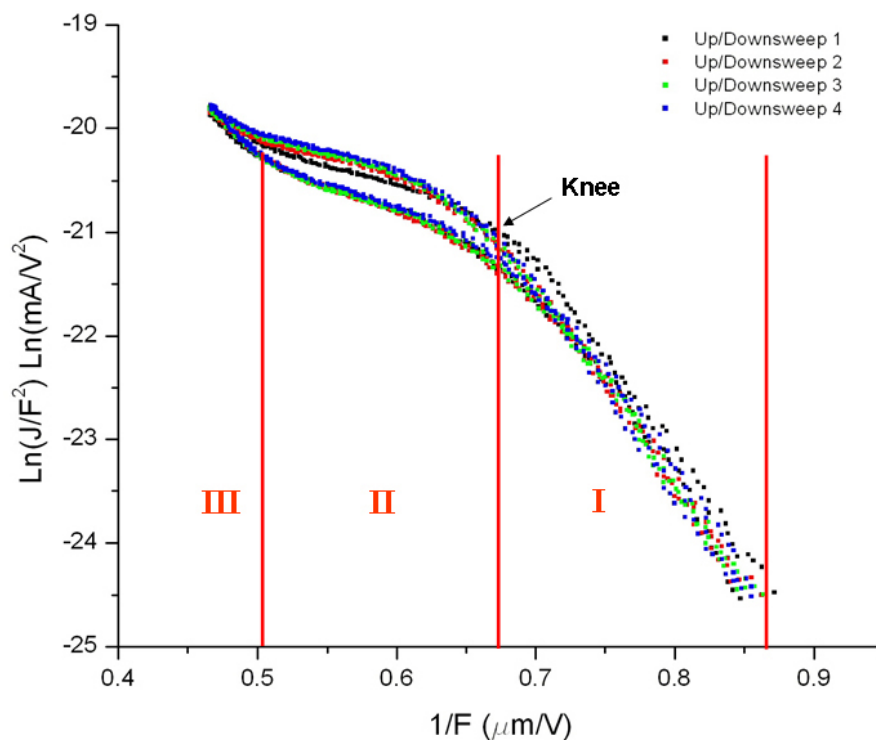


Figure 5.14. *F-N plot of a CNT indicating three distinct regions of field emission behavior.*

These regimes have been observed and discussed by various authors and there has been debate on which emission region is characteristic of the actual emission behavior of the CNT films.^{15,16,17} The Fowler-Nordheim equation indicates that a plot of $\ln(J/F^2)$ vs. $1/F$ should result in a straight line. Regions I and II are commonly observed in literature and both have been used to characterize the emission behavior of CNTs.^{16,18} The transition from emission region I to II, sometimes referred to as a “knee” has been attributed to a variety of factors including current saturation due to removal of adsorbates known to enhance emission,¹⁹ suppression of emission due to interaction between neighboring CNTs,²⁰ current saturation due to space charge,¹⁶ and a transition due to interface barrier effects originating from the contact between the CNTs,¹⁷ catalyst, and the substrate.

Although region III is less commonly reported, it has been suggested that this is the true emission region and that regions I and II are attributed to adsorbate interactions alone.

This is evidenced in Fig. 5.15. A F-N plot of the data shown in Fig. 5.13 reveals that maintaining high current levels effectively prevented the return of adsorbates to the CNTs resulting in what will be referred to as the clean state.

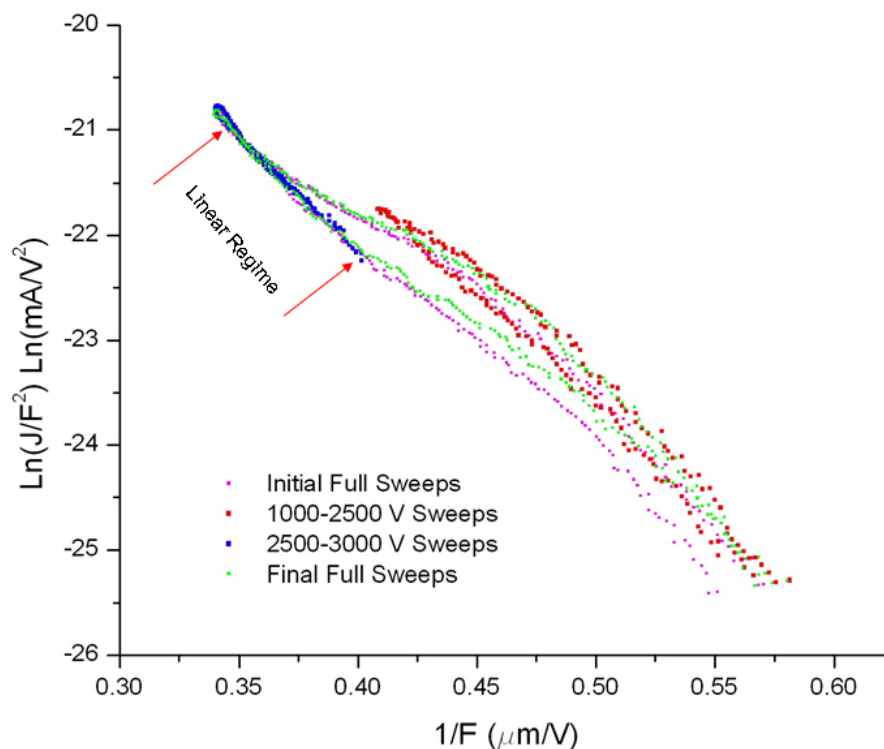


Figure 5.15. F-N plots of a CNT film operating in the high (blue), medium (green-magenta), and low (red) current regimes.

When comparing the F-N plot of the clean state, the slope was found to follow closely to that of region III. This further supported our proposal that region II was indeed an adsorbate induced state. Unfortunately, in this system, the clean state of the CNTs could not be maintained at lower current levels to verify the F-N behavior over the whole emission regime.

5.4.3 Field Emission Stability of CNT Emitters

Investigation of the emission stability of the CNT films was characterized by recording the emission current vs. time at various emission current levels. These

measurements were performed in the PPFES at moderate current levels. The results are presented in Fig. 5.16, and it is evident that at a current level of ~ 0.76 mA, the emission is quite stable for the data acquisition time of 3 hours.

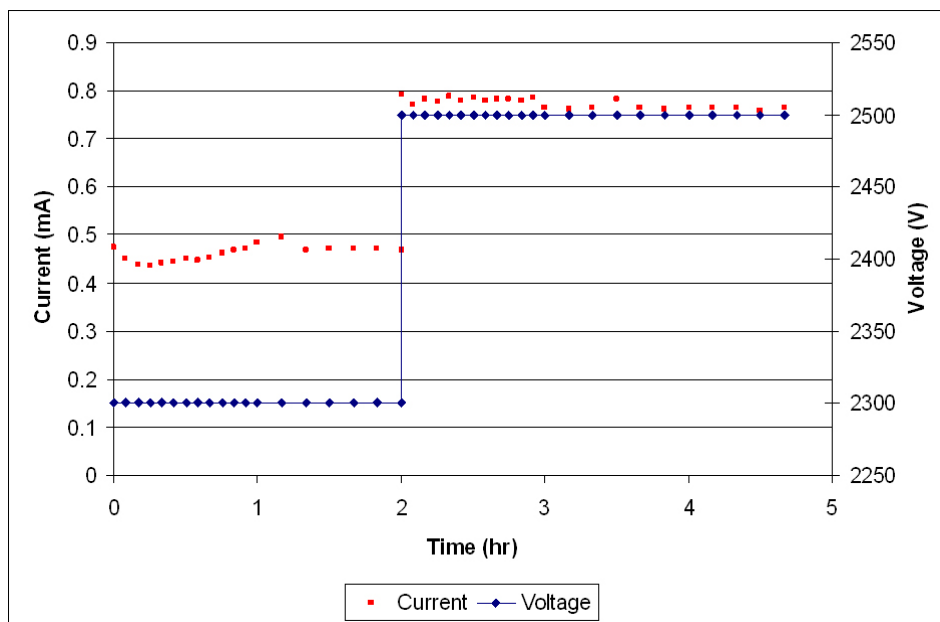


Figure 5.16. Emission stability of a CNT film deposited on a TiN coated Si substrate. The stability was measured at two different current levels.

High current stability measurements were prohibited due to significant heating of the thermally isolated floating anode plate.

5.5 Field Emission Characterization in the UHV Thermionic/Field Emission System

Verification of the F-N emission behavior of the CNT films spanning the low and high emission regimes was enabled using the thermionic/field emission system (TFES). The TFES is interconnected to the UHV process and characterization system and is composed of a 1 cm^2 moveable anode and a heatable sample stage. This allowed high current measurements of CNT films in UHV with heating capabilities which could be used to effectively remove adsorbates from the CNTs surfaces.

The CNT films were loaded into the TFES and an initial high current I-V sweep was performed at 475 °C. The film was then annealed to higher temperatures performing I-V sweeps at ~ 100 °C intervals. After the film was annealed to ~ 700 °C the film was cooled to a temperature of 390 °C and a final I-V sweep was carried out. The maximum pressure recorded for the as-loaded and post annealed measurements was 3×10^{-8} torr and 5×10^{-9} torr, respectively. Upon analysis of the data it was observed that the first I-V sweep, after loading the sample, contained the characteristic knee in the F-N plot.

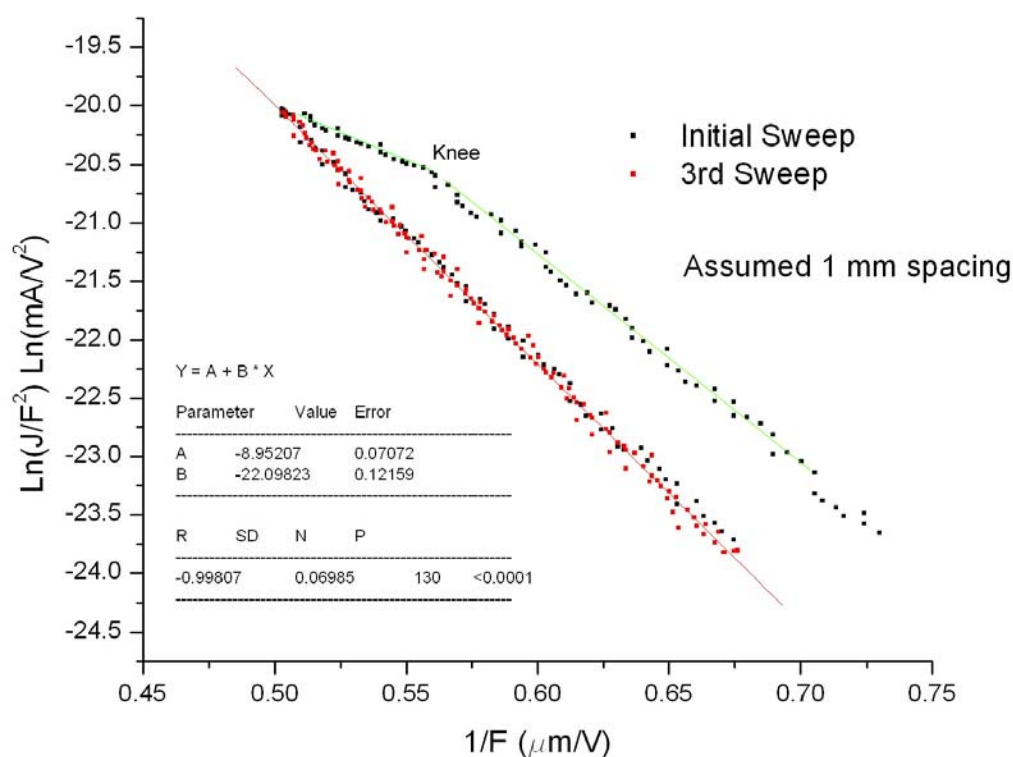


Figure 5.17. F-N plot of an as loaded CNT film showing the transition on the initial upsweep from an adsorbate induced state to the clean state on the downsweep.

F-N plots of the subsequent sweeps revealed that the knee characterized by region I and II were eliminated. This indicated that adsorbates were effectively removed from the surface and that they did not return at the low current regime. The F-N plots were linear over the whole emission regime, low and high, and were within good correlation to a linear fit.

Similar measurements obtained after exposure of the CNT film to atmosphere revealed that the adsorption/desorption process was reversible. The initial and resulting J vs. F and $F-N$ plots of the TFES measurements are shown in Fig. 5.18 and Fig. 5.19, respectively. These plots were generated using estimated gap spacings of 0.5 mm and 1 mm.

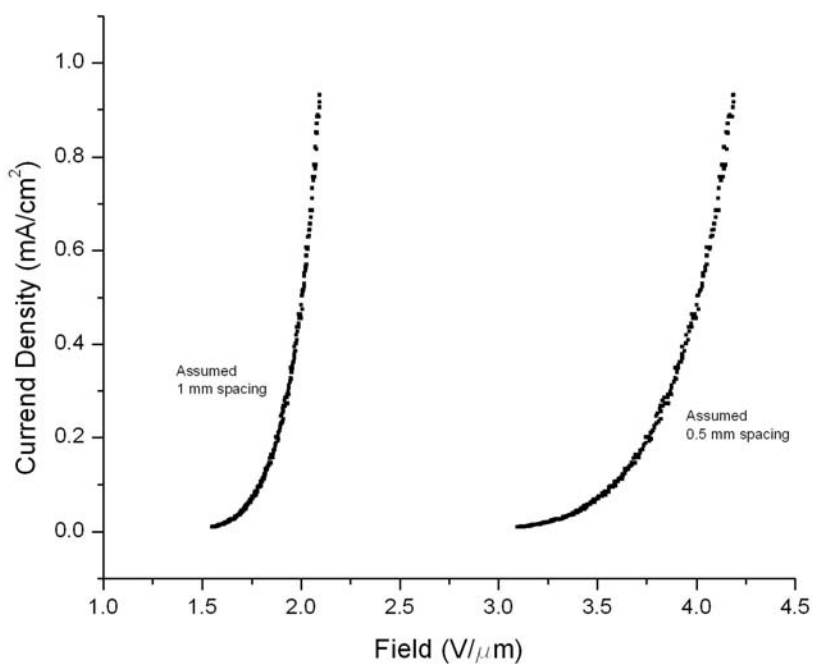


Figure 5.18. Current density vs. applied field for an outgassed (clean) CNT film obtained assuming 1mm (left) and 0.5 mm (right) spacing.

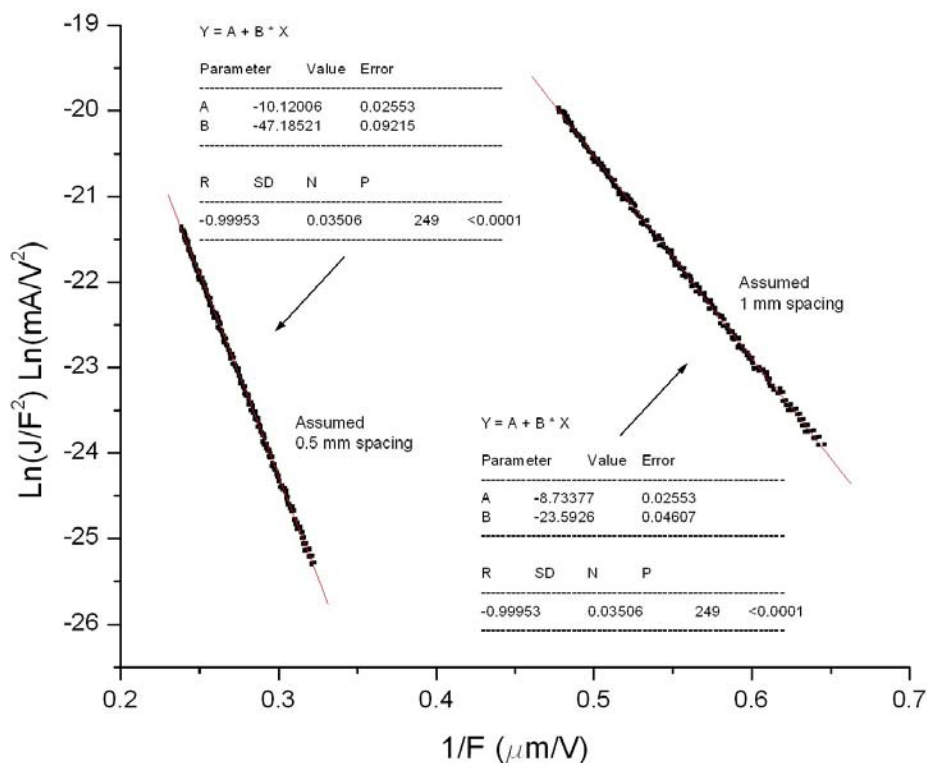


Figure 5.19. *F-N plots for an outgassed (clean) CNT film obtained assuming 1mm (left) and 0.5 mm (right) spacing.*

Although a true separation distance of the anode and cathode is unknown, by visual inspection it is estimated that the spacing was $\sim 1\text{mm}$. The low limit on spacing was 0.5 mm and was determined by a spacer used in the mounting of the sample. The $\sim 1\text{ mm}$ gap was estimated by a visual observation of a small gap between the anode and spacer. The field emission data presented in Figs. 5.18 and 5.19, using a 1 mm gap spacing, was in good agreement with data obtained in the PPFES where the actual gap distance was known. This was additional verification that the actual spacing in the TFES measurements was close to 1 mm. The slope of the lines in Fig. 5.19 can be used to predict the emission performance of the films at higher applied fields. If an anode-cathode separation distance of 1 mm is assumed, the linear fit to the data predicts a current density of 3.6 A/cm^2 at an applied field of $5\text{ V}/\mu\text{m}$.

5.6 Characterization of CNT Emitters by Field Emission Imaging

Electron sensitive photoluminescent materials have been used for decades in display and imaging applications such as cathode ray tube based television sets and transmission electron microscopy screens. Light emissive materials, for example, $\text{Gd}_2\text{O}_2\text{S:Tb}$, ZnS:Ag , or ZnO:Zn , have been found to be an effective means of detecting the distribution of high energy electrons directed at a surface. The emission site density of deposited field emitters is of particular importance to applications such as field emission displays which require more than 10^7 emitters distributed evenly over a surface area of typically 10^2 - 10^3 cm^2 .²¹

In this study, ZnS:Ag (blue emission) and ZnO:Zn (green emission) coated indium tin oxide imaging screens were employed as a method to detect and image the distribution of field emitted electrons from CNT films prepared using PECVD. Specifically, emission site density, uniformity and the field required for the onset of emission were of interest. Two modes of operation, high and low magnification, were used to study the emissive properties of the PECVD grown CNT films. A small gap parallel plate diode configuration was used to determine the general emission distribution over substrates up to 1" in diameter. Large gap triode configurations were employed to obtain magnified projections of the electron emission to investigate the emissive properties of individual CNTs.

The emission site density of the films can play a critical role in determining the actual validity of I-V measurements and threshold field calculations determined using the approach curve and parallel plate methods. This is due to the fact that a few strong emissive sites can exhibit Fowler-Nordheim-like emissive behavior and result in misleading characterization of the emitters.

Figure 5.20 shows a series of emission images recorded for a carbon nanotube film under various applied fields.

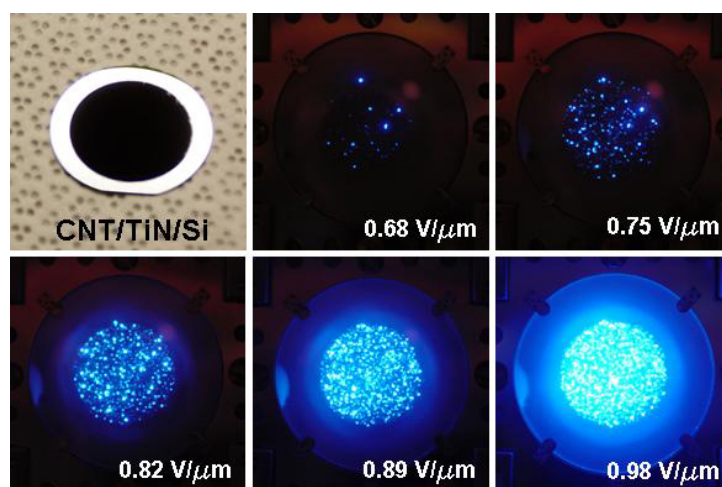


Figure 5.20. Image of a PECVD grown CNT film on a TiN coated Si substrate, and emission images recorded from the film at various applied fields.

The emission images were captured in the emission imaging system, using a ZnS:Ag coated indium tin oxide screen, operating in the parallel plate geometry shown in Fig. 5.21.

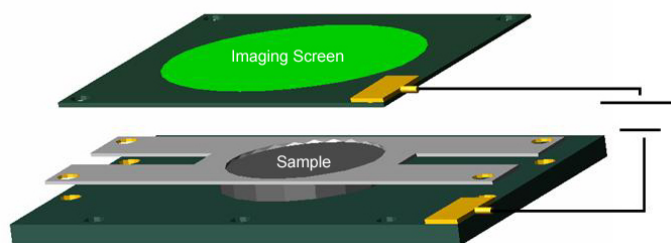


Figure 5.21. Schematic of parallel plate field emission imaging setup.

It can be seen in the emission site images of Fig. 5.20 that a considerable increase in emission site density occurs for small increase ($\sim 0.3 \text{ V}/\mu\text{m}$) in the applied field. The emission site distribution is found to be fairly uniform over the 3.24 cm^2 sample area at an applied field of $0.98 \text{ V}/\mu\text{m}$. Emission imaging at higher fields was terminated at this point due to saturation of the CCD camera and potential to cause damage to the imaging screen.

An important characteristic of the emission distribution images is that emission does not preferentially occur along the edges of the CNT deposited area. Sample preparation played a key role in preventing edge effects which are a result of additional field enhancement contributions and phenomena originating from the edges of the substrate. These effects are commonly observed in emission distribution images and can significantly influence the outcome of I-V measurements. A shadow mask was used during the deposition of the Fe catalyst to selectively determine where CNT growth would occur on the substrate surface. In order to prevent CNT growth along the edges of the 1" Si substrate, a circular 0.8" diameter growth area was patterned in the center of the substrate. This effectively prevented edge effects occurring from the substrate and allowed space for topside contact to the substrate for I-V measurements and emission site imaging.

It is observed in the J vs. F curve, shown in Fig. 5.22, that saturation of the CCD camera occurs in the low current regime of emission from the film shown in Fig. 5.20.

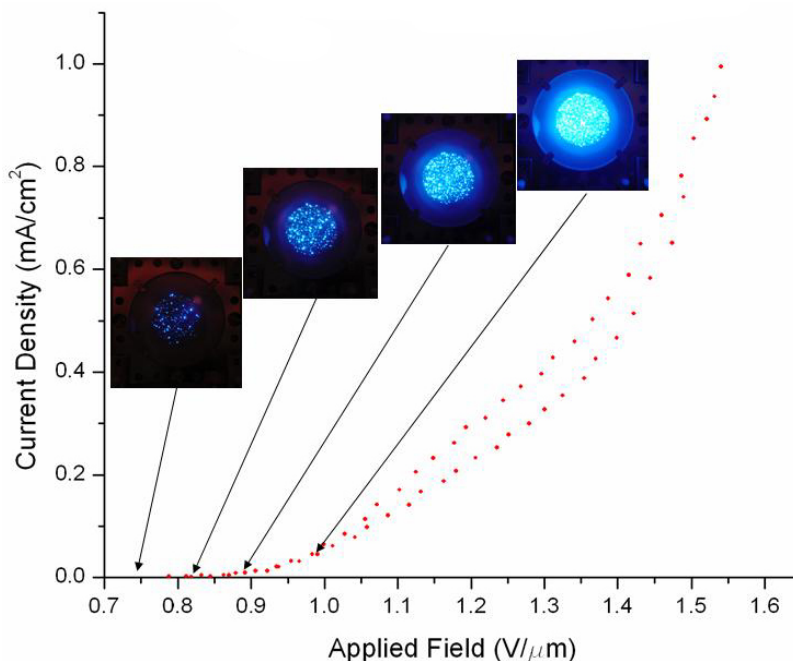


Figure 5.22. A plot of current density vs. applied field for a CNT film with inserted emission images corresponding to the field at which they were captured.

In Fig. 5.22 the arrows from the emission images point to the corresponding fields at which they were captured. Groning et al. evaluated the emission site density vs. applied field for a PECVD grown CNT film and found a significant increase in emission site density from 5 sites/cm² at 1.8V/μm to >10⁴ sites/cm² at 3.5 V/μm.²¹ It is expected that for the sample shown in Fig. 5.20, the emission site density will significantly increase upon application of higher fields. In order to obtain quantitative information on the actual emission site density, a less emissive imaging screen will be needed since CCD saturation was observed to occur at a low value on the current density vs. field curve. Additionally spot-like emission is not observed for all emission sites. It has been shown that adsorbates can lead to lobe-like emission patterns, which presents difficulties in determining the actual emission site densities.²²

5.7 Growth and Characterization of Carbon Nanoparticles on Metallic Substrates

Extending beyond the limits of Si based field emitter devices, the selective PECVD growth of CNTs on metallic Ti and Mo substrates was investigated. As in the case of direct growth of CNTs on Si substrates, catalyst/metal substrate interactions occurring at the high growth temperatures can ultimately leave the catalyst in an inactive state.

5.7.1 PECVD Growth of CNPs on Fe/TiN/Ti and Fe/TiN/Mo Substrates

TiN buffer layers were employed into catalyst/buffer/metal stacks in order to preserve the activity of the Fe catalyst films during the PECVD growth process. 1" diameter Mo and Ti substrates, 1 mm thick, were machined from bulk plates of each type of metal. Prior to TiN deposition, the substrates were cleaned and etched using a chemical polish consisting of nitric, hydrofluoric, acetic and phosphoric acid. After chemical etching, the substrates were rinsed in DI water and dried using compressed nitrogen.

TiN films, 25 nm thick, were deposited on the Ti and Mo substrates using plasma assisted reactive evaporation. Deposition conditions were identical to those used for the work outlined in chapter 3. After deposition of the TiN films, 20 nm Fe films were electron beam evaporated on the on the TiN/Ti and TiN/Mo substrates. The successful deposition of a TiN film as well as the Fe catalyst was confirmed by XPS after each deposition process.

The catalyst containing substrates were removed from UHV and loaded into the PECVD system for CNT growth. Prior to deposition, the substrates were pretreated for 2 min at ~640 °C under a C₂H₂/NH₃ atmosphere. After pretreatment, a hydrogen plasma was initiated and the hydrogen gas source was removed and simultaneously replaced with C₂H₂ (25 sccm) and NH₃ (55 sccm) gas sources to provide the proper reactants for CNT growth. Growth was carried out at a pressure of 28 torr, microwave power of 900 watts, and a

temperature of ~ 975 °C which was achieved through the combination of induction heating and heating due to the plasma.

Upon removal of the substrates from the PECVD chamber a significant difference was observed in the physical appearance of the Fe/TiN/Ti and Fe/TiN/Mo substrates. For clarity, the substrates will be referred to as Fe/TiN/Mo and Fe/TiN/Ti where Fe denotes a 20 nm thick deposited catalyst layer, TiN denotes a 25 nm thick TiN buffer layer, and Mo or Ti denotes the 1 mm thick starting metal substrates. After PECVD growth, the surface of the Fe/TiN/Ti substrates appeared gold/yellow in color, similar to the as-deposited TiN films, while the Fe/TiN/Mo substrates appeared black.

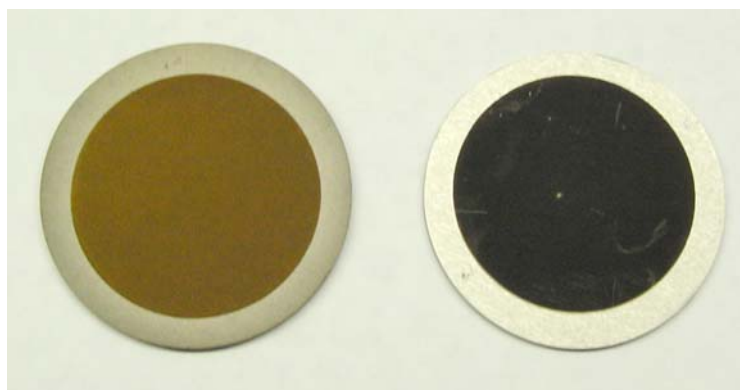


Figure 5.23. Images of Fe/TiN/Ti (left) and Fe/TiN/Mo (right) substrates after PECVD growth.

After deposition, XPS and Raman investigation of the Fe/TiN/Ti substrates revealed that indeed a form of carbon growth occurred under the PECVD growth conditions.

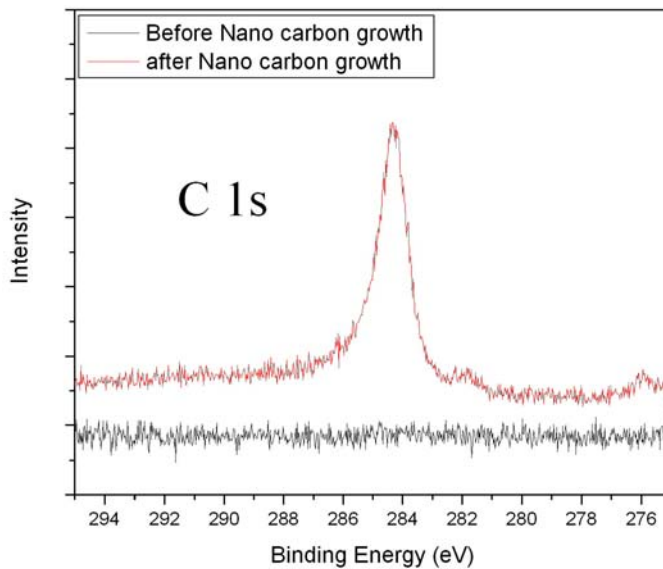


Figure 5.24. XPS ($Mg K\alpha$) analysis of PECVD carbon growth on a Fe/TiN/Ti substrate.

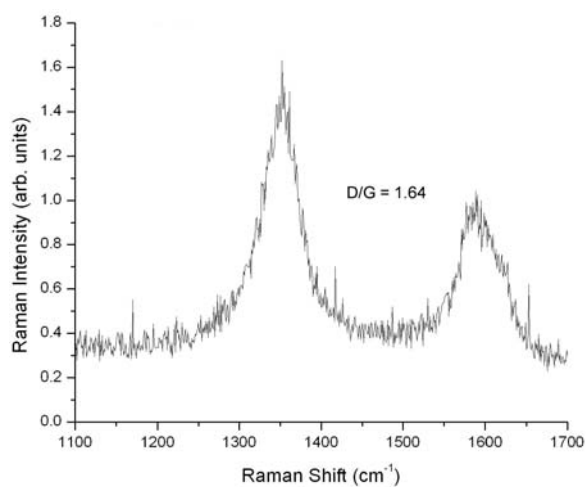


Figure 5.25. Raman spectra of PECVD carbon growth on a Fe/TiN/Ti substrate.

The unusual aspect of the XPS spectra of the Fe/TiN/Ti substrate, taken after the deposition, is the absence of a significant Fe signal.

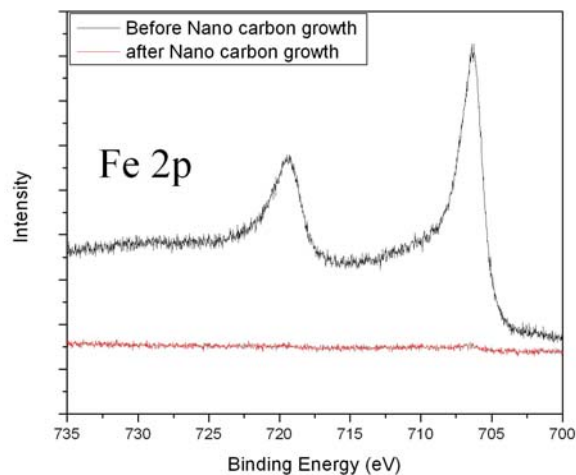


Figure 5.26. XPS ($Mg\ K\alpha$) spectra of Fe pre and post carbon growth on a Fe/TiN/Ti substrate.

SEM images on the Fe/TiN/Ti substrates after PECVD growth revealed small nanoparticles on the surface of the TiN buffer layer. It was also observed that the 1 mm thick Ti wafer and TiN buffer layer coating contained an abundant amount of cracks that propagating along and through the substrate.

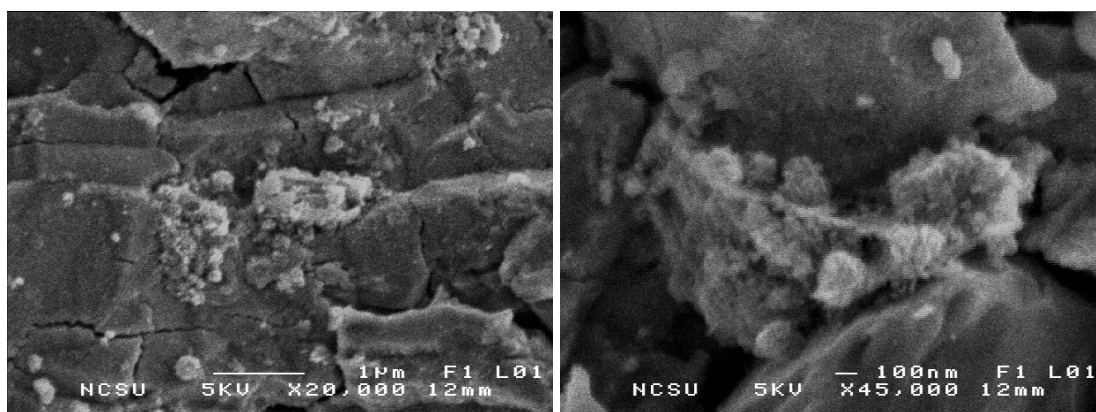


Figure 5.27. SEM images of nanoparticles grown on a Fe/TiN/Ti substrate.

The graphitic peak in the Raman spectra indicated that some form of catalytic hydrocarbon decomposition and growth occurred on the surface of the film. When considering the escape depth of electrons in XPS it is likely that the absence of the Fe signal

may be due to the Fe catalyst being encapsulated by a carbon film thicker than the escape depth of the emitted electrons.

As in the case of the Fe/TiN/Ti substrates, Raman spectroscopy of the PECVD treated Fe/TiN/Mo substrates indicated the catalytic growth of a carbon species on the surface.

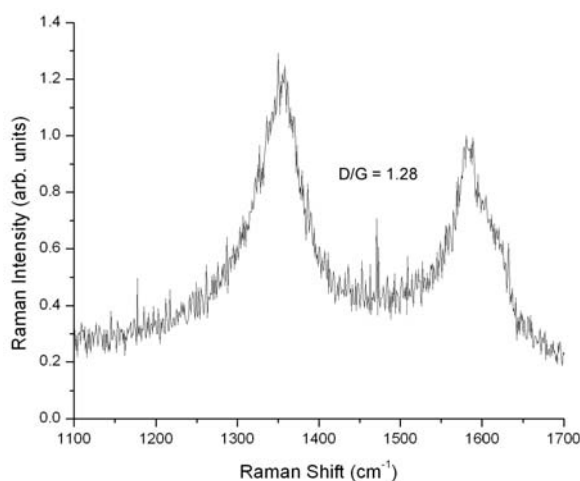


Figure 5.28. Raman spectra of PECVD carbon growth on a Fe/TiN/Mo substrate.

In comparison to the carbon films grown on the Fe/TiN/Ti substrates, a higher content of disordered carbon was detected on the Fe/TiN/Mo substrates. The D/G ratio of the carbon film on the Fe/TiN/Ti substrate was 1.28 while the D/G ratio of the carbon film on the Fe/TiN/Mo substrate was found to be 1.64.

SEM images of the carbon film grown on the Fe/TiN/Mo substrate revealed a different morphology than that observed for the films grown on the Fe/TiN/Ti substrates. The SEM image in Fig. 5.29 (a) shows the transition between the regions of the Fe/TiN deposited area (left) and the bare Mo substrate (right).

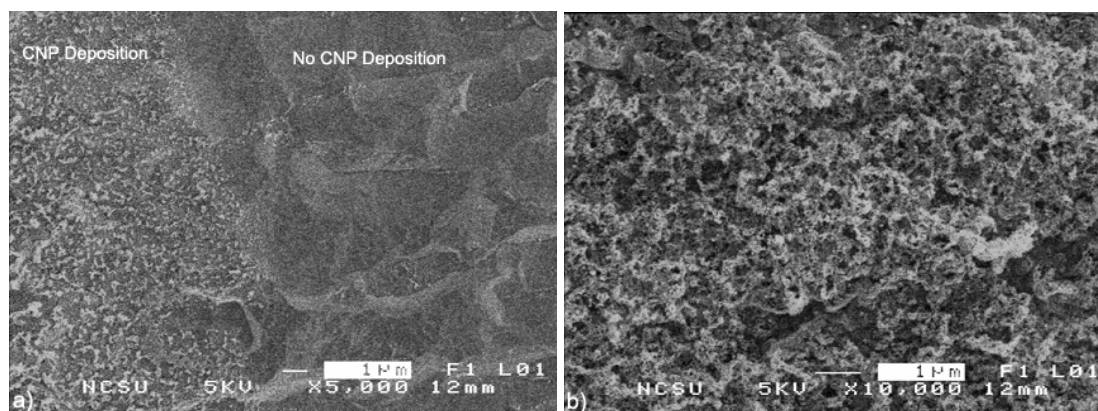


Figure 5.29. SEM images of carbon nanoparticles grown on a Mo/TiN/Fe coated substrate showing a) transition from deposited area to bare Mo substrate, and b) 10 kX magnified image of carbon nanoparticle structure.

A coral like structure was observed for the deposited film which closely resembled what has been referred to as carbon nanoparticles (CNPs) by Yu et al.²³ Although similar growth conditions to those described in chapter 4 were used, the formation of CNTs were not observed in the SEM images of the films grown on the Fe/TiN/Ti and Fe/TiN/Mo substrates. During the PECVD growth of the CNP films it was observed that plasma focusing, apparently due to interactions with the thick metallic substrates, occurred. It is likely that this produced a growth environment significantly different to that obtained for CNT growth on the Fe/TiN/Si substrates.

It should be noted that TiN/Ti layers have been used as high temperature diffusion barriers for Si devices²⁴ and the successful high temperature deposition of Ti on Mo substrates have been reported.²⁵ This suggests that the integrity of the TiN/Ti and TiN/Mo interfaces are maintained at high temperatures (~ 800 °C), but at growth temperatures of ~ 975 °C it is possible that the TiN support layers can be compromised. It is suggested that CNT growth will be enabled on the Fe/TiN/Ti and Fe/TiN/Mo substrates with the optimization of growth conditions.

5.7.2 Field Emission Properties of CNPs Grown on Fe/TiN/Ti and Fe/TiN/Mo Substrates

Substrates

Field Emission characterization of the CNPs grown on the Fe/TiN/Ti and Fe/TiN/Mo substrates revealed that the films exhibited significant emission at low applied fields. The plot in Fig. 5.30 was obtained for a CNP film grown on a Fe/TiN/Mo substrate and the plot in Fig. 5.31 was obtained for a CNP film grown on a Fe/TiN/Ti substrate.

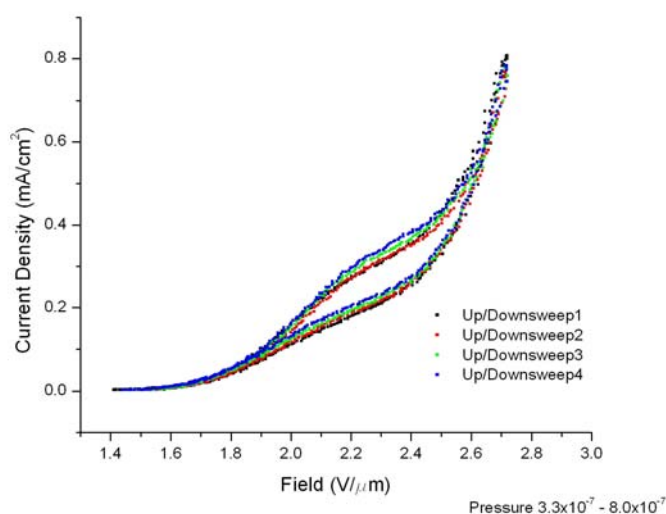


Figure 5.30. Current density vs. applied field for a CNP film deposited on a Fe/TiN/Mo substrate. The measurements were obtained using the PPFES.

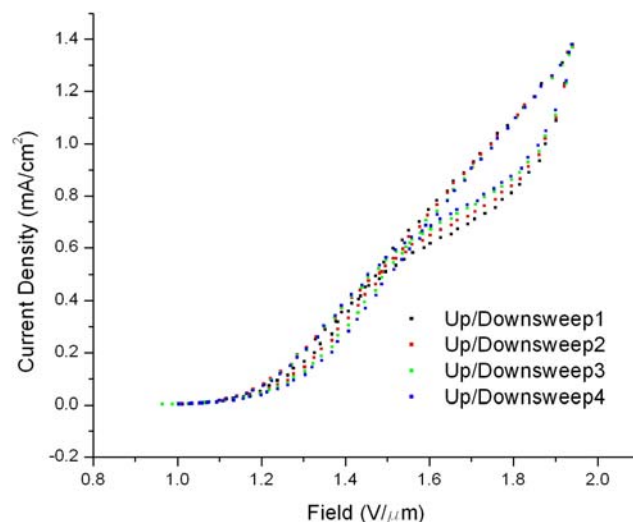


Figure 5.31. Current density vs. applied field for a CNP film deposited on a Fe/TiN/Ti substrate. The measurements were obtained using the PPFES.

Comparisons of current density vs. field measurements of numerous films revealed that the CNT films prepared on Fe/TiN/Si substrates and CNP films deposited on Fe/TiN/Ti substrates appeared to be the best emitters achieving current densities of 1 mA/cm^2 at applied fields of $\sim 2.1 \text{ V}/\mu\text{m}$ or less. Although slightly less emissive, current densities of 1 mA/cm^2 were achieved for applied fields of $\sim 2.9 \text{ V}/\mu\text{m}$ for the CNP films deposited on the Fe/TiN/Mo substrates.

In addition to the emission images of CNT samples grown on Fe/TiN/Si substrates, emission images of CNPs grown on Fe/TiN/Ti and Fe/TiN/Mo substrates were captured. As in the case of the CNT films, the CNP films exhibited relatively uniform emission over the sample surface area. Figures 5.32(a) and 5.32(b) show emission images captured for a Mo/TiN/Carbon (ZNO) and Ti/TiN/Carbon (ZNS) film respectively.

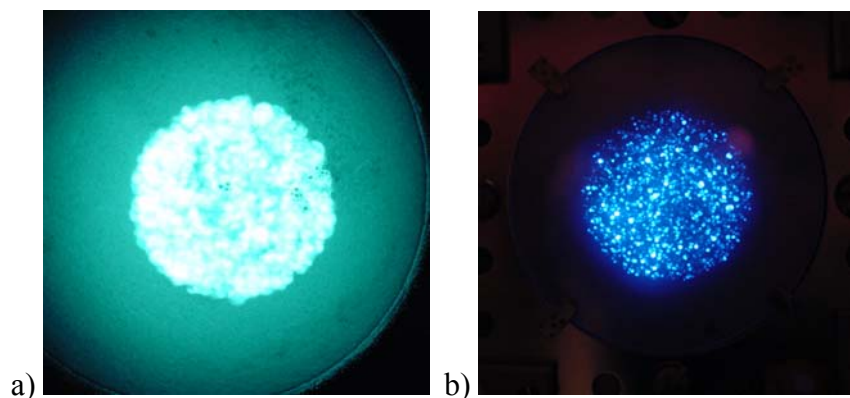


Figure 5.32. Emission images captured for a) CNPs grown on a Fe/TiN/Mo coated substrate using a (ZNO) imaging screen and for b) CNPs grown on a Fe/TiN/Mo coated substrate using a (ZNS) imaging screen. Saturation of the CCD camera is evident in (a).

5.8 Observation of Ring Formations in Field Emission Images

Under the parallel plate mode of acquisition in the emission imaging system, unique singular emission patterns were observed to originate from the CNT films grown on the TiN coated Si substrates and CNPs grown on the TiN coated Mo substrates. These unique emission patterns appeared as highly symmetric rings, all of similar diameter, and the number of sightings varied significantly from sample to sample.

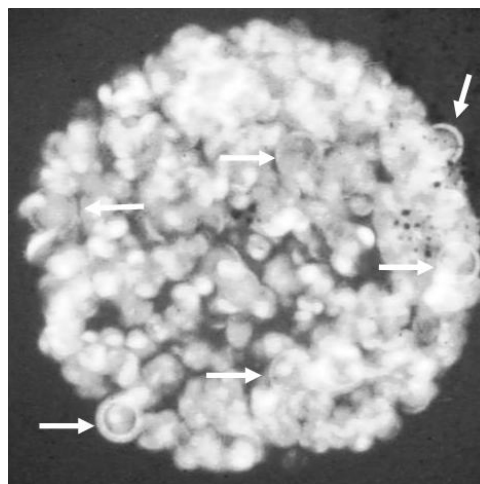


Figure 5.33. Emission images of a CNP film grown on a Fe/TiN/Mo coated substrate which reveals the appearance of emission rings indicated by arrows.

To further investigate the unusual patterns observed in the emission images, high magnification imaging was employed by modifying the parallel plate emission geometry to a triode setup. This involved the insertion of an extraction grid close to the sample surface and increasing the image screen distance to achieve magnification. The individual rings shown in Fig. 5.34 were observed to appear at higher emission currents and were found to be stable only over a small range of applied fields. As the applied field was increased the rings were found to abruptly disappear.

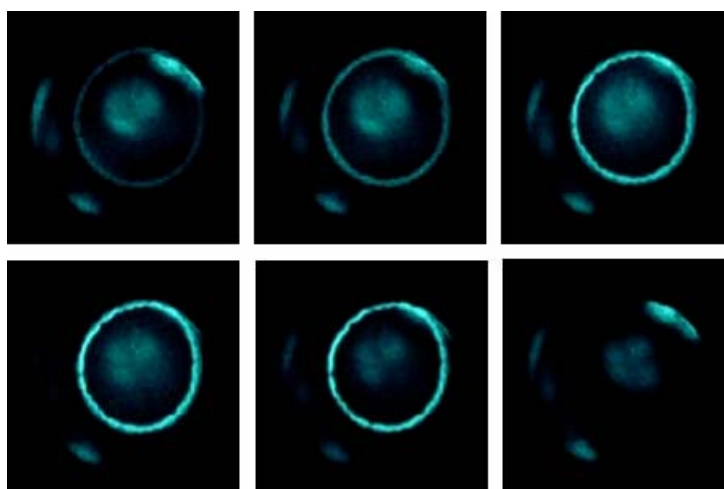


Figure 5.34. A series of images showing emission rings obtained using the parallel plate high magnification system.

The images captured in Fig. 5.33 were obtained by utilizing an extraction grid made by mounting a 3 mm diameter (600 mesh) copper TEM grid to a copper plate. The extraction grid was placed in a configuration similar to the one shown in Fig. 5.35.

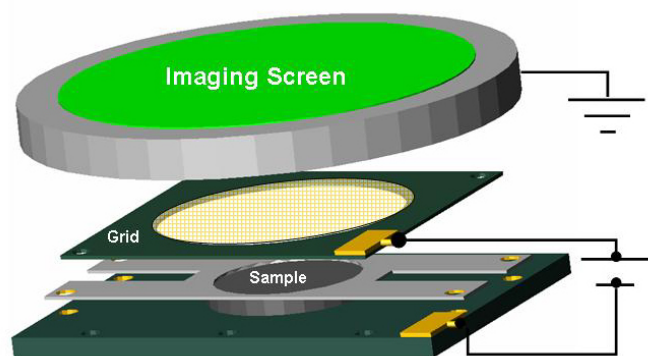


Figure 5.35. Schematic of the high magnification parallel plate emission imaging setup.

The asymmetry in the ring patterns observed in Fig. 5.34 is attributed to variations in the local field originating from imperfections in the grid mounting process.

5.8.1 Jožef Stefan Institute Collaboration

In addition to the emission imaging system used to capture the images shown in Figs. 5.32 and 5.33, a secondary system was used to obtain high resolution images of the emission rings observed for the CNT and CNP samples. Emission images were obtained through a collaboration with the researchers at the Jožef Stefan Institute located in Ljubljana, Slovenia. An image and corresponding schematic of the secondary imaging system is shown in Fig. 5.36.

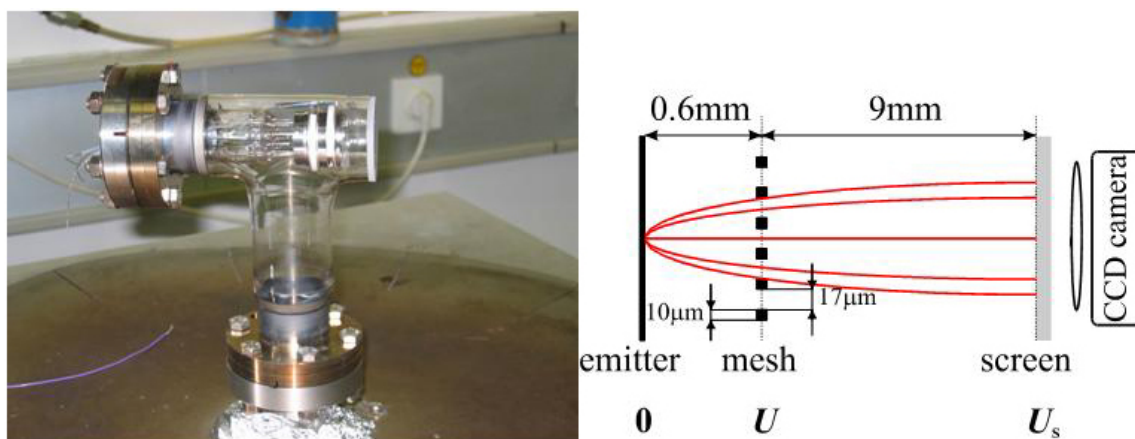


Figure 5.36. Image and schematic of the field emission imaging triode located at the Jožef Stefan Institute.

Emission images captured from the various films clearly showed the highly symmetric rings as observed for the images captured using the parallel plate system. In addition, a number of films grown under varying growth conditions exhibited arc-like emission behavior.

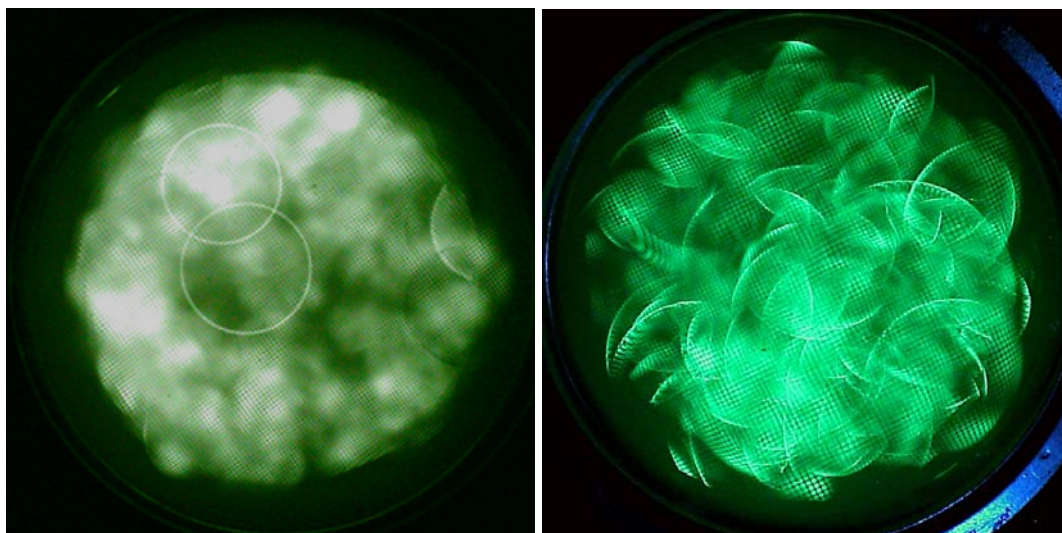


Figure 5.37. Field emission images captured for CNT films using the triode imaging system located at the Jožef Stefan Institute. Ring emission patterns as well as arc emission patterns were observed.

5.8.2 Theory Behind Ring Structure Formation

Various experimental results have been reported on the field emission images of individual nanotubes which revealed structured emission patterns.^{22,26,27,28} These patterns, typically symmetric, were attributed to adsorbates and/or the atomic structure of the nanotube tip where conventional theory predicts emission originates. Models have been developed to simulate emission patterns from single CNTs in efforts to link them to experimental observations.^{29,30} Several reports have noted the ring shaped emission patterns which are typically observed when the field emitting nanotubes are operated in the high current regime.^{26,31,32,33} These ring patterns, in many cases exhibiting a hollow center, could be attributed to an open-ended nanotube which would satisfy conventional theory. When

considering the electron trajectories required to form the particular rings observed in this study, an alternative emission model must be considered. In addition, structured images were also observed within these ring patterns suggesting that the emission originated from a closed CNT tip.

The onset of the ring pattern at high current emission and the abrupt disappearance indicate that the observation of the rings occur at the pre-breakdown regime of the emitter. Furse et al. were able to observe similar field emission patterns from metallic tips of W and Ta at currents approaching critical pre-breakdown states where significant emitter tip heating occurred.² In addition it has been noted by Dean et al. that the formation of rings appeared to have a temperature dependence.³⁴ Although the general explanation given for the rings is that emission originates from an open ended tube, there is significant contradictory evidence suggesting that the emission behavior occurs through another mechanism.

Walker et al. proposed a model to attribute the spreading of emitted electrons due to local field curvature near the emission site³⁵, while Filip et. al. proposed that for high emission currents, part of the electrons behave as quasi-free resulting in spatial confinement quantization of their states.³⁶ It was noted that although the extraction field is higher at the nanotube tip, there is a probability of finding an electron close to the body of the nanotube.

The rings formed within the triode imaging setup were found to have a radius ranging from approx. 3.1 to 6.4 mm giving a semi-angle ranging from 18 to 34 degrees (See Fig. 5.38).

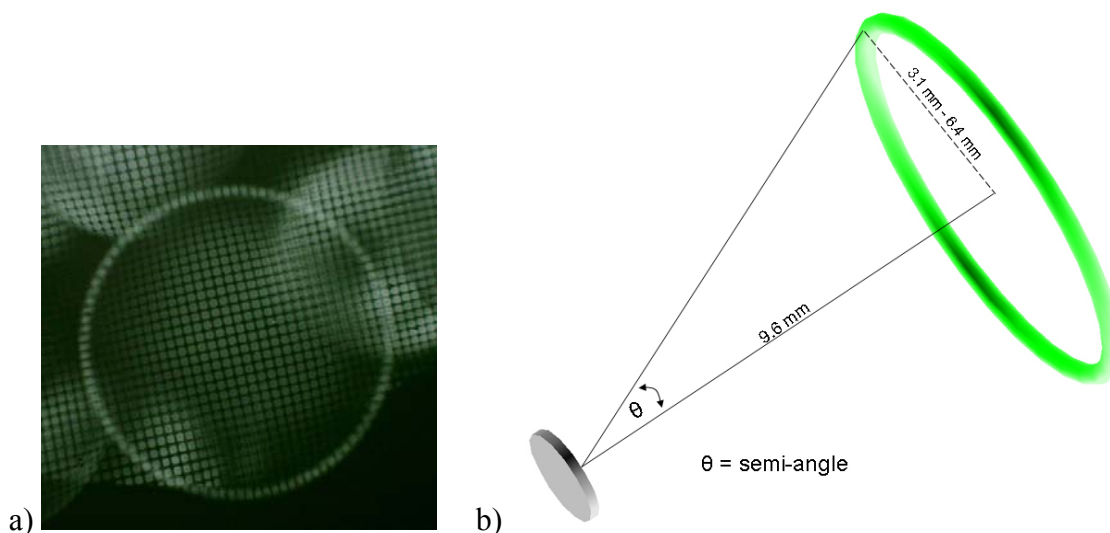


Figure 5.38. a) Image of an emission ring from a CNT film, identifying the high level of symmetry associated with the ring structure (a shadow of the extraction grid can be seen in the background) and b) schematic identifying the semi-angle of emission (the point-source emitter is represented as a disk for visual aid).

The models of Filip and Walker predict the formation of rings if suitable conditions and specifications are met, but this model has difficulty accounting for the large lateral electron momentum required to produce rings through the large-semi angles calculated in our results. An explanation of the rings will require further investigation and innovative analysis techniques. Work is currently being performed at the Jožef Stefan Institute to locate a single emission ring with a scanning field emission microscope. This microscope utilizes a scanning anode that possesses a micromachined hole along its axis. The channel along the anode enables electron projection on a phosphor screen whose intensity can be monitored. A larger image can be generated by monitoring the emission intensity as the anode scans, similar in operation to a SEM. The difficulty in these measurements comes in locating an individual ring.

5.9 Summary of Field Emission Characterization of CNT Films

Fowler-Nordheim theory was used to evaluate the field emissive behavior of the CNT films grown on TiN coated Si substrates by PECVD techniques. The approach curve method was employed to investigate the emission characteristics of the films and from the data an average field enhancement value of ~ 2300 was determined. In the VDFES, it was observed that annealing CNT films in UHV improved the stability of emission.

High current measurements collected from emission areas of 3.24 cm^2 were obtained using the PPFES. Significant hysteresis was observed in the I-V sweeps of the CNT films measured in this system. It was proposed that adsorbates leaving and returning to the CNT films, at various emission levels, were responsible for the hysteresis. F-N plots of the emission data indicated that the commonly observed non-linear regimes of F-N plots from CNT films could be attributed to the proposed adsorbate effects. Emission current densities of 1 mA/cm^2 at an applied voltage of $\sim 2.1 \text{ V}/\mu\text{m}$ were obtained for the CNT films. Additionally, it was observed that the emission from the films was stable over a 3 hour acquisition time while operating at moderate current levels of $\sim 0.75 \text{ mA}$.

High current UHV measurements performed in the thermionic/field emission system revealed that the CNT films grown on TiN coated Si substrates behaved according to F-N theory. Data analysis of the initial I-V sweeps in the thermionic/field emission system resulted in the commonly observed “knee” in the F-N plots. Upon removal of the adsorbates by tip and sample heating, the resulting F-N plots were linear over the low, medium, and high emission regimes. It was also noted that the absorption/desorption process was reversible by exposing the sample to atmosphere. Convincing evidence was obtained in

these measurements suggesting that the commonly observed non-linear regimes of the F-N plots are a direct result of adsorbate effects.

It was noted in field emission images of the CNT films, that a relatively uniform distribution of emission sites occurred over the 3.24 cm² deposited area. This indicated that the I-V measurements made in the parallel plate and thermionic/field emission systems were characteristic of the films as a whole and that strong singular sites did not significantly contribute to the high current densities obtained from the films.

PECVD grown CNPs, obtained on Fe/TiN/Ti and Fe/TiN/Mo substrates, exhibited similar field emission behavior to that of the CNT films produced on Fe/TiN/Si substrates. Optical and SEM images of the CNP films revealed structures significantly different than the CNTs prepared on Fe/TiN/Si substrates. A higher disordered carbon state, as compared to CNTs, was observed in the Raman spectra of the CNP films. It was proposed that the deposition of the CNPs was due to variations in the growth environment and that the growth of CNTs would be possible on the Fe/TiN/Ti and Fe/TiN/Mo substrates with optimization of growth conditions.

The final section of this chapter summarized the initial stages of the investigation into the unique ring structures observed in field emission images of the CNT and CNP films. The work, carried out in collaboration with researchers from the Jožef Stefan Institute revealed that the emission rings were well defined and required a unique mechanism of formation. While models have been developed to explain the formation of emission rings, there is difficulty in these models to account for the large diameter and well defined symmetry of the rings.

REFERENCES

- ¹ Robert Gomer, *Field Emission and Field Ionization*. (American Institute of Physics, New York, 1993).
- ² George Fursey, *Field Emission in Vacuum Microelectronics*. (Springer, 2005).
- ³ W. Schottky, *Zeitschrift Fur Physik* **14**, 63 (1923).
- ⁴ R. A. Millikan and C. F. Eyring, *Physical Review* **27** (1), 51 (1926).
- ⁵ O. W. Richardson, *Proceedings of the Royal Society of London Series a-Containing Papers of a Mathematical and Physical Character* **117** (778), 719 (1928).
- ⁶ P. Debye, *Annalen Der Physik* **33** (13), 441 (1910).
- ⁷ R. H. Fowler and L. Nordheim, *Proceedings of the Royal Society of London Series a-Containing Papers of a Mathematical and Physical Character* **119** (781), 173 (1928).
- ⁸ A. Modinos, *Field, Thermionic, and Secondary Electron Emission Spectroscopy*. (Plenum Press, New York, 1984).
- ⁹ P. H. Cutler, J. He, N. M. Miskovsky et al., *Journal of Vacuum Science & Technology B* **11** (2), 387 (1993).
- ¹⁰ M. Meyyappan, *Carbon Nanotubes: Science and Applications*. (CRC Press, Boca Raton, 2005).
- ¹¹ C. A. Spindt, I. Brodie, L. Humphrey et al., *Journal of Applied Physics* **47** (12), 5248 (1976).
- ¹² Rodney Latham, *High Voltage Vacuum Insulation: Basic Concepts and Technological Practice*. (Academic Press Inc., San Diego, 1995).
- ¹³ Y. Saito and S. Uemura, *Carbon* **38** (2), 169 (2000).
- ¹⁴ M. Sveningsson, R. E. Morjan, O. A. Nerushev et al., *Applied Physics a-Materials Science & Processing* **73** (4), 409 (2001).
- ¹⁵ R. Collazo, R. Schlessler, and Z. Sitar, *Diamond and Related Materials* **11** (3-6), 769 (2002).
- ¹⁶ Y. Chen, S. Z. Deng, N. S. Xu et al., *Materials Science and Engineering a-Structural Materials Properties Microstructure and Processing* **327** (1), 16 (2002).

- 17 H. H. Zhang, C. R. Yang, W. W. Yang et al., *Solid State Communications* **138** (1), 13 (2006).
- 18 J. H. Han, S. H. Choi, T. Y. Lee et al., *Journal of Vacuum Science & Technology B* **21** (3), 1120 (2003).
- 19 S. C. Lim, H. J. Jeong, Y. S. Park et al., *Journal of Vacuum Science & Technology A* **19** (4), 1786 (2001).
- 20 P. G. Collins and A. Zettl, *Physical Review B* **55** (15), 9391 (1997).
- 21 O. Groning, O. M. Kuttel, C. Emmenegger et al., *Journal of Vacuum Science & Technology B* **18** (2), 665 (2000).
- 22 K. Hata, A. Takakura, and Y. Saito, *Ultramicroscopy* **95** (1-4), 107 (2003).
- 23 J. Yu, Q. Zhang, J. Ahn et al., *Journal of Materials Science Letters* **21** (7), 543 (2002).
- 24 J. S. Chen and K. Y. Lu, *Thin Solid Films* **396** (1-2), 204 (2001).
- 25 J. C. Nable, S. Nosheen, S. L. Suib et al., *Surface & Coatings Technology* **200** (8), 2821 (2006).
- 26 K. A. Dean and B. R. Chalamala, *Journal of Vacuum Science & Technology B* **21** (2), 868 (2003).
- 27 W. M. Liu, S. M. Hou, Z. X. Zhang et al., *Ultramicroscopy* **94** (3-4), 175 (2003).
- 28 T. Kuzumaki, Y. Horiike, T. Kizuka et al., *Diamond and Related Materials* **13** (10), 1907 (2004).
- 29 C. Oshima, K. Mastuda, T. Kona et al., *Physical Review Letters* **88** (3), 4 (2002).
- 30 A. Buldum and J. P. Lu, *Molecular Simulation* **30** (4), 199 (2004).
- 31 J. H. Lee, S. H. Lee, W. S. Kim et al., *Journal of Vacuum Science & Technology B* **23** (2), 718 (2005).
- 32 M. Kumar, K. Kakamu, T. Okazaki et al., *Chemical Physics Letters* **385** (3-4), 161 (2004).
- 33 J. M. Bonard, C. Klinke, K. A. Dean et al., *Physical Review B* **67** (11), 10 (2003).
- 34 K. A. Dean and B. R. Chalamala, *Applied Physics Letters* **76** (3), 375 (2000).

- ³⁵ D. G. Walker, W. Zhang, and T. S. Fisher, *Journal of Vacuum Science & Technology B* **22** (3), 1101 (2004).
- ³⁶ L. D. Filip, D. Nicolaescu, M. Tanemura et al., *Journal of Vacuum Science & Technology B* **23** (2), 649 (2005).

6. Concluding Remarks

The goal of this chapter is to serve two functions. It's main purpose is to summarize the work reported in this thesis, but it also offers suggestions for future work.

6.1 Summary and Results

This work focused on the influence of TiN on the growth and field emission properties of CNTs selectively grown on Si substrates. In chapter 3 the application of TiN as a buffer layer to prevent the interaction of catalyst metals, used in CNT growth, with the underlying substrates was discussed. Atomic force microscopy, photo electron emission microscopy, and X-ray photoelectron spectroscopy revealed that TiN films, deposited by plasma assisted reactive evaporation, were of high quality and effectively prevented the rapid formation of iron silicide which is known to inhibit the growth of CNTs at high temperatures. Additionally, it was indicated that high temperature plasma anneals of the TiN films resulted in a higher thermal stability of the films. The improved thermal stability was attributed to the nitrogen rich annealing atmosphere produced by the $C_2H_2:NH_3$ plasma.

Chapter 4 outlined the benefits of plasma enhanced chemical vapor deposition and showed that CNTs could be produced on TiN coated Si substrates using Fe catalysts. SEM, TEM, and Raman spectroscopy revealed that graphitic vertically aligned CNTs were produced by the base growth mechanism and that the diameter of the PECVD grown CNTs could be controlled by variations in the catalyst film thickness. The growth rate of the CNTs was determined to be approximately $5 \mu\text{m}/\text{min}$ for films grown using a 20 nm Fe catalyst layer.

Field emission theory, and the field enhancement effects which give CNTs their unique capabilities were introduced in the first sections of chapter 5. Field emission

measurements from the CNT films, produced using the methods outlined in chapter 4, revealed that the CNT films grown on TiN coated Si substrates acted as excellent field emitters generating current densities of 1 mA/cm^2 under applied fields of $\sim 2.1 \text{ V}/\mu\text{m}$. CNT films operating in the intermediate current regimes showed quite stable emission over the three hour data acquisition period. The emission distribution from the films, observed using a phosphor imaging screen, was found to be uniform over the selected deposited area of 3.24 cm^2 . The commonly observed non-linearity in the F-N plots of emission from CNTs was attributed to adsorbate interactions. With the effective removal of adsorbates, linearity in the F-N plots was observed throughout the high and low emission current regimes.

In addition to the CNT films, attempts to grow CNTs on metallic substrates using TiN buffers resulted in the growth of CNPs. These films exhibited excellent field emission properties similar to that of the CNT films. The formation of CNPs on TiN coated metallic substrates as opposed to CNTs is not directly understood, but it is speculated that variations in plasma behavior due to substrate interactions may be responsible. It is expected that with optimization of growth conditions, CNT growth from Fe catalysts will be enabled on the Ti and Mo substrates coated with the TiN buffer layers.

The collaborative work, performed with researchers at the Jožef Stefan Institute, identifying the unusual ring-shaped emission patterns from the CNT and CNP films is currently at its developmental stages. Although numerous images of highly symmetric rings were captured, significant conclusions about their mechanism of formation can not be made at this time.

6.2 Suggestions and Future Work

The TiN films in this study were deposited using plasma assisted reactive evaporation. It has been found that densification of the films and improved barrier effectiveness can be obtained using biased deposition.¹ It would be useful to apply the biased deposition techniques since the initiation of thermal instabilities was found to occur in the PECVD deposited TiN films at temperatures close to those used for CNT growth.

Knowledge of the emission site density of the CNT films would be particularly useful in the characterization of the films. In order to carry out these measurements a secondary imaging setup or a less emissive imaging screen would be needed. In addition, it was shown that adsorbates significantly influence the emissive behavior of the CNT films. UHV annealing and high current sweeps to drive off adsorbed species will significantly improve the emission site distribution analysis. For these measurements, close attention must be paid to the choice of phosphor used in the emission imaging screen since the addition of binders, used to make the phosphor coating more robust, can lead to significant outgassing issues. An interesting alternative to the phosphor screens was implemented by Lee et al..² In their study, an electron-beam resist was used for the detection of electron emission from CNTs. This method, similar to the use of photographic film, may result in higher resolution images of the emission site distribution.

In addition to adsorbates, a significantly discussed topic is the screening effect known to occur for metallic CNTs during field emission. A reduction in the overall emissive behavior of CNTs through the screening effect has been theoretically calculated and experimentally observed.^{3,4} Dense CNT films have been shown to be less emissive than films of medium density. It has been predicted that in order to achieve the maximum

emission from the films, the tubes should be spaced approximately one tube length from the other.⁴ Patterning of Fe catalysts using lithography or porous alumina templates could be employed to produce mid-density arrays of CNTs on the TiN buffer layers. It is suggested that these arrays will improve the field emission results reported in this thesis. Additionally, the implementation of TiN buffer layers may assist in the difficulties of producing aligned CNT arrays from patterned catalysts.

Extending beyond the capabilities of the voltage supplies used in this work, it would be most interesting to verify the emission behavior of the CNT films at field emission levels above 5 mA or 1.54 mA/cm² for a 3.24 cm² deposited area. One could simply reduce the emission area, but as noted earlier, this could result in misleading analysis when attempting to obtain quantitative data such as the achievable emission current densities from the films. It would be of specific interest to determine the maximum emission capabilities of the film as well as their stability at various emission current levels. It can be predicted from the F-N plot in Fig. 5.18 of chapter 5, that a current density of >3 A/cm² can be obtained at an applied field of 5 V/μm. Although a field of 5 V/μm is very realistic and in some cases considered low, it is difficult to predict the emission behavior at such high current levels since only a fraction of the CNTs within the 3.24 cm² deposited area are emitting. In this case, the linearity observed in the F-N plots, after adsorbate removal, would be a tool to determine when the emission deviates from F-N behavior and additional factors such as thermionic emission come into play.

REFERENCES

- ¹ T. de los Arcos, F. Vonau, M. G. Garnier et al., *Applied Physics Letters* **80** (13), 2383 (2002).
- ² J. H. Lee, S. H. Lee, W. S. Kim et al., *Journal of Vacuum Science & Technology B* **23** (2), 718 (2005).
- ³ J. S. Suh, K. S. Jeong, J. S. Lee et al., *Applied Physics Letters* **80** (13), 2392 (2002).
- ⁴ L. Nilsson, O. Groening, C. Emmenegger et al., *Applied Physics Letters* **76** (15), 2071 (2000).